## **Evolution of Fiber Microstructure During Polymer Processing**

By

Tzu-Chuan Chang

A dissertation submitted in partial fulfillment of the requirements for the degree of

Doctor of Philosophy

(Mechanical Engineering)

At the

UNIVERSITY OF WISCONSIN - MADISON

2023

Date of final oral examination: September 22<sup>nd</sup>, 2023

This dissertation is approved by the following members of the final oral committee:

Tim A. Osswald, Professor, Mechanical Engineering
Lih-Sheng (Tom) Turng, Professor, Mechanical Engineering
Pavana Prabhakar, Professor, Civil and Environmental Engineering
Lianyi Chen, Professor, Mechanical Engineering
Alejandro Roldan, Professor, Mechanical Engineering

## **Abstract**

Discontinuous fiber-reinforced polymers play a significant role in the automotive industry due to their lightweight properties and excellent mechanical performance with lower manufacturing costs. Since there are many unknowns regarding how fibers interact with the polymer matrix during polymer processing, it is crucial to understand how fiber orientation, fiber length, and fiber concentration affect the final part's properties.

As few modeling techniques can accurately predict both fiber damage and fiber orientation during polymer processing, such as injection molding, a particle-level simulation is used in this study to predict the fiber motion in the polymer flow. In the particle level simulation, each fiber is represented as a chain of rods that experience hydrodynamic, interaction, and elastic effects. The simulation results were compared to simple shear flow experiments conducted in a Couette Rheometer to validate the model's approach.

In addition to the particle-level simulation, a modified breakage model developed in the Polymer Engineering Center, UW-Madison, was implemented as a post-processing tool for injection molding simulation using Moldex3D to find the optimum value for predicting fiber damage in the polymer process. The model was validated with different fiber content materials as well as different part geometries and processing conditions. A new form of stress-induced fiber breakage model was proposed to allow more accurate predictions on fiber attrition in polymer processing.

## Acknowledgments

It has been a wonderful journey here at the Polymer Engineering Center at the University of Wisconsin-Madison. First and foremost, I would like to express my sincere thanks to my parents for their continuously and unconditionally encouragement and support throughout this journey. I wouldn't have been able to make it this far without their support for the past 6 years. I would like to extend my sincere gratitude to my advisor, Prof. Tim Osswald, for providing me a chance to come and study in Madison. His invaluable guidance and mentorship throughout my graduate school greatly contributed to the success of this work. I would like to express special thanks to Allen J. Román and Jamelah Cholewa for their warm welcome and support during my difficult times. Secondly, I would like to thank the entire current and former PEC family that made my time in Madison an unforgettable experience as we shared the laughs and frustrations together. I would like to thank the Fibers Group who I worked closely with and who helped with critical feedback and collaboration; in particular, I want to thank Ian Walter, Sara Simon, Abrahan Bechara, and Kelsey Hacker. I would also like to thank Trevor Winterhack and Sebastian Tompson for being wonderful undergraduate research assistants and helping me with the Couette flow experiments. Additionally, I would like to thank Angel Yanev, Ruud Winter, and Simon Staal from SABIC, who made this research possible and provided me with a chance to broaden my experience and explore the work life in the Netherlands. Last but not least, thanks to those friends I met along the journey here in Madison.

## **Table of Contents**

Abs	stract		i
Acl	knowled	dgments	ii
Tab	le of C	ontents	iii
Lis	t of Fig	ures	v
Lis	t of Tab	oles	X
Noi	nencla	ture	xi
1.	Intro	duction and Motivation	1
	1.1.	Introduction	1
	1.2.	Objectives	2
2.	Liter	ature Review	3
	2.1.	Processed Induced Fiber Orientation	3
	2.2.	Processed Induced Fiber Length Degradation	5
	2.3.	Prediction on Fiber Breakage	6
	2.4.	Fiber-Flow Coupling	8
3.	Direc	ct Fiber Simulation	10
	3.1.	Theoretical background	10
	3.2.	Sample Preparation	13
		3.2.1. Improve the procedure of the cluster preparation.	13
		3.2.2. Implementing Fiber Length Distribution	20
	3.3.	Fiber Attrition Simulation	22
		3.3.1. Update in the Program	23
		3.3.2. The effect of shear stress	28
		3.3.3. Influence of Probability Theory on Fiber Damage	30
		3.3.4. Parallelization of the code	40
4.	Modified fiber breakage model		47
	4.1.	Introduction	47
	4.2.	Modeling Approaches	49
	4.3.	Effect on Fiber-Flow Coupling (Plaque)	51
	4.4.	Effect on fiber length distribution	60
	4.5.	Effect on part geometry (Plaque vs Tailgate)	63

5.	Shear S	Stress Induced Fiber Attrition Model	74
6.	Summary		81
	6.1.	Recommendations for future work	82
	6.2.	Publications	83
7.	Reference 84		84
Appe	ndix A.		<b>\</b> -1

# **List of Figures**

Figure 2.1 Unit vector p for orientation of a single rigid fiber in the Cartesian coordinate system	3
Figure 2.2 Schematic representation of different orientation tensors: (a) unidirectional, aligned with	h
axis 1, (b) random orientation.	4
Figure 2.3 Schematic diagram of short fiber (Left) and long fiber pellets (Right).	5
Figure 3.1 Particle level simulation: modeling single fiber and macroscale interactions	10
Figure 3.2 An example of the spherical coordinate used in generating the fiber positions	14
Figure 3.3 An example of the differential area when generating the fiber positions.	15
Figure 3.4 Fiber distribution and projection plane	16
Figure 3.5 The flow chart of generating a fiber cluster with randomlu placed position of fibers	
integrated into the algorithm.	17
Figure 3.6 The flow chart of generating a fiber cluster with a predetermined orientation integrated	
into the algorithm.	19
Figure 3.7 A 5 wt% cluster with 1331 fibers which orientation tensor $a11, a22, a33 =$	
0. 6, 0. 3, 0. 1	20
Figure 3.8 An example of fiber length distribution as an input for generating initial fiber cluster	21
Figure 3.9 The flow chart of the Direct Fiber Simulation.	22
Figure 3.10 The orientation result in $a11$ direction using different number of segments to represent	ıt
a single fiber: (a) 10 segments in a single fiber, (b) 25 segments in a single fiber	23
Figure 3.11 The orientation result in <b>a11</b> direction with fixed dt set for the simulation: (a) $dt =$	
10 - 5, (b) $dt = 10 - 6$	24
Figure 3.12 The orientation result in <b>a11</b> direction with auto dt adjusted depends on the segment	
displacement for the simulation: (a) set input dt: $dt = 10 - 5$ , (b) set input $dt = 10 - 6$	26
Figure 3.13 The comparison between the simulation result from the updated algorithm of	
mechanistic model and the Jeffery rotation model with fiber aspect ratio below 100	27
Figure 3.14 The comparison between the simulation result from the updated algorithm of	
mechanistic model and the Jeffery rotation model with fiber aspect ratio from 0 to 800	27
Figure 3.15 The test location on an injection molded plaque with PPGF05 and the corresponding	
shear stress profile during the simulation using Moldex3D.	28
Figure 3.16 The fiber attrition with various shear stress in the mechanistic model and the	
corresponding breakage distribution in the simulation.	29

Figure 3.17 The Predicted <i>LW</i> and <i>LN</i> of simple shear flow simulation at varying shear stress with
PPGF05: (a) Shear stress = 5000 Pa, (b) Shear stress = 10000 Pa
Figure 3.18 Fiber deformation and approximation with bending theory: (a) Beam deformation with
pure bending; (b) Approximation with rods and the expression of critical curvature during
fiber breakage
Figure 3.19 Breakage Distribution of the loop test using glass fibers
Figure 3.20 Shear cell with periodic boundary conditions
Figure 3.21 Length evolution result by mechanistic model using an empirical excluded volume force
constant compared to Couette flow experimental
Figure 3.22 Predicted <i>LN</i> of simple shear flow simulation at varying fiber critical breaking
curvature with three excluded volume force constants A from: (a) 250, (b) 500, (c) 750 34
Figure 3.23 Predicted <i>LN</i> of simple shear flow simulation at varying excluded volume force
constant $\boldsymbol{A}$ with three critical curvature from: (a) 200 $\mu$ m, (b) 250 $\mu$ m, (c) 300 $\mu$ m34
Figure 3.24 Stepwise increase profile in shear rate for fiber relaxation
Figure 3.25 Predicted <i>LN</i> of simple shear flow simulation at varying fiber critical breaking
curvature with fiber relaxation applied to the first second in the simulation
Figure 3.26 Fiber length evolution compared to the Couette flow experiment with fiber relaxation
applied to the first second in simulation
Figure 3.27 Different breakage models implemented in the mechanistic model: (a) Original breakage
model; (b) probability breakage model when $m = 15$
Figure 3.28 Fiber length evolution compared to the Couette flow experiment with fiber relaxation
and probability breakage applied to the first second in simulation
Figure 3.29 Varying values of $m$ for the probability breakage applied in the model
Figure 3.30 Breakage Distribution over time of simulation results with fiber relaxation and
probability breakage model applied
Figure 3.31 The distribution of which the segment's curvature is within 50 $\mu m$ of the critical
breaking point: 200~250 $\mu m$ for No PB (Left); 400~450 $\mu m$ for PB (Right) in simulation 39
Figure 3.32 Fiber Length Distribution at the end of 150 second simulation
Figure 3.33 Computational structure of OpenMP program
Figure 3.34 Computational structure of MPI Program
Figure 3.35 The working comparison between multi-threading and message passing in the algorithm
[59]42
Figure 3.36 The flow chart of communicating process in algorithm with two cores utilized in

computation
Figure 3.37 The flow chart of communicating process in algorithm with multiple cores utilized in
computation44
Figure 4.1 The procedure of extracting fiber length distribution data from simulation over the part
thickness
Figure 4.2 The procedure of calculating the average error percentage from a simulation result 51
Figure 4.3 An overview of fiber length measurement process developed at the PEC
Figure 4.4 The injection molded plaque for fiber length measurements, (a) the geometry of molded
plaques, (b) the sample location extracted from the plaques
Figure 4.5 Result of the local fiber length measurement for all trials, showing the number-average
fiber length, $\boldsymbol{LN}$ , and the weight-average fiber length, $\boldsymbol{LW}$ at four locations: in the purged
material, close to the gate (Loc.1), at the center of the plate (Loc.2), and at the end of the flow
(Loc.3)54
Figure 4.6 The average percent error of $\xi$ value for simulation result without fiber-flow coupling
calculation of fiber length degradation for PPGF20 and PPGF30 with two thickness of plaques
in Moldex3D55
Figure 4.7 The average percent error of $\xi$ value for simulation result with fiber-flow coupling
calculation of fiber length degradation for PPGF20 and PPGF30 with two thickness of plaques
in Moldex3D56
Figure 4.8 The optimum $\xi$ from the simulation with disable fiber-flow coupling calculation as
function of the initial fiber aspect ratio
Figure 4.9 The optimum $\xi$ from the simulation with enable fiber-flow coupling calculation as
function of the initial fiber aspect ratio
Figure 4.10 The comparison of weight-average fiber length (LW) degradation between the modified
breakage model and Phelps model for PPGF20 and PPGF30 with for 1.5 and 2mm-thick
injection molded plaque59
Figure 4.11 The comparison of number average fiber length $(LN)$ degradation between the modified
breakage model and Phelps model for PPGF20 and PPGF30 for 1.5 and 2 mm-thick injection
molded plaque60
Figure 4.12 The comparison of fiber length distribution between the measured results and the
Figure 4.12 The comparison of fiber length distribution between the measured results and the simulated fiber length distribution at four locations for PPGF20, 1.5 mm-thick injection

the simulated length with fiber length distribution integrated for PPGF20 and PPGF30 for 1.5
and 2 mm-thick injection molded plaque.
Figure 4.14 The geometry of an injection molded tailgate.
Figure 4.15 The flow front profile of an injection molded tailgate at dfferent filling percentage with
all gates open at once during injection stage65
Figure 4.16 The flow front of an injection molded tailgate at dfferent filling percentage with a
predefined gates opening and clouses sequence during the process
Figure 4.17 The sprue pressure of two different valve gate open system: open all at once and
sequence open for the injection molded tailgate.
Figure 4.18 Fiber length measurement at three locations of an injection molded tailgate where P1 is
in the beginning of the filling, P2 is at 50% of the filling, and P3 is at the end of filling 68
Figure 4.19 The comparison of average fiber length degradation between the modified breakage
model and the measured result for PPGF30 and PPGF40 for the injection molded tailgate 69
Figure 4.20 The $\xi$ distribution of the same material (PPGF30) with two different geometries and part
thickness
Figure 4.21 The average shear rate profile across the part thickness in the simulation: (a) Location
one in injection molded plaque, (b) P1 in injection molded tailgate71
Figure 4.22 The comparison between the $\xi$ difference of plaque versus tailgate and the difference in
shear rate profile: (a) no fiber-flow coupling enabled in computation, (b) fiber-flow coupling
enabled in computation. 72
Figure 4.23 The average shear stress profile across the part thickness in the simulation: (a) Location
one in injection molded plaque, (b) P1 in injection molded tailgate
Figure 4.24 The comparison between the $\xi$ difference of plaque versus tailgate and the difference in
shear stress profile: (a) no fiber-flow coupling enabled in computation, (b) fiber-flow coupling
enabled in computation
Figure 5.1 The $\xi$ distribution with different $\lambda$ values used in the simulation
Figure 5.2 The reduction in fiber length as a function of residence time for PPGF30 at two rotational
speeds with a melt temperature of 250°C [23]
Figure 5.3 Average interaction coefficient $\lambda$ as function of fiber concentration [27]76
Figure 5.4 The fitting curves of fiber length reduction over residence time with calculated $kf$ 78
Figure 5.5 The dimensionless $y$ over residence time compared to Couette flow experiments78
Figure A.1 The comparison of fiber length distribution between the measured results and the
simulated fiber length distribution at four locationsn for PPGF20, 2.0 mm-thick injection

molded plaque.	A-1
Figure A.2 The comparison of fiber length distribution between the measured results and the	
simulated fiber length distribution at four locationsn for PPGF30, 1.5 mm-thick injection	
molded plaque.	A-2
Figure A.3 The comparison of fiber length distribution between the measured results and the	
simulated fiber length distribution at four locationsn for PPGF30, 2.0 mm-thick injection	
molded plaque.	A-3

## **List of Tables**

Table 1 The test input for evaluating the performance of adjusted dt with the mechanistic model 25
Table 2 The time cost of different dt used in the simulation
Table 3 Constant values of shear cell properties in simulation
Table 4 Values varied in simulation
Table 5 The break-down of the time cost for each function in the algorithm
Table 6 Test environment for evaluating the performance of the parallelization for the algorithm 45
Table 7 The computational time required for calculating fiber motion in the algorithm
Table 8 The computational time required for calculating excluded volume force in the algorithm46
Table 9 Total computational time required for 15,000-time steps for different version of the
algorithm46
Table 10 An overview of fiber length measurement parameters
Table 11 The validation test result with a different initial fiber length as input for the simulation 58
Table 12 The test input of integrating the fiber length distribution into simulation
Table 13 Processing condition of manufacturing injection molded tailgate part
Table 14 The sequence of the valve gate used in the hot runner for the injection molded tailgate 66
Table 15 The comparison of the cases that has been validated using the modified fiber breakage
model
Table 16 The cases condition studied to analyze the relationship between two different geometries.
72

## Nomenclature

$L_N$	Number-Average Fiber Length
$L_W$	Weight-Average Fiber Length
$L_{\infty}$	Equilibrium fiber length
$L_0$	Initial fiber length
r	Fiber Radius
D	Fiber Diameter
$\eta_m$	Matrix Viscosity
ζ	Hydrodynamic Drag Coefficient
S	Distribution Shape Factor
$E_f$	Young's Modulus
Ϋ	Shear Rate
ξ	Fiber Breakup rate constant
λ	Dimensionless parameter for interactions
$k_f$	Rate of Deformation
t	Time
S	Seconds
T	Torque
$a_{11}$	Fiber Orientation Tensor in Flow Direction
$a_{22}$	Fiber Orientation Tensor in Crossflow Direction
$a_{33}$	Fiber Orientation Tensor in Thickness Direction
$\eta_S(\dot{\gamma})$	Shear Viscosity of the Cross Viscous Fluid
$R_T(\dot{\gamma})$	Trouton Ratio
τ	Extra Stress Tensor
D	Rate-of-deformation Tensor
$\varphi$	Fiber Volume Fraction
$N_P$	Dimensionless Parameter
$C_I$	Fiber-Fiber Interaction Parameter
$C_M$	Fiber-Matrix Interaction Parameter

$\alpha$	Slowdown Parameter
$\dot{\lambda}_i$	Eigenvalues
R	Eigenvector
$\underline{F}_{i}^{H}$	Drag Forces from the Surrounding Fluid
$\underline{F}_{ij}^{\mathcal{C}}$	Inter-Fiber Interaction Force with Rod
$\underline{X}_i$	intra-fiber forces exerted by adjacent Rod i
$\underline{X}_{i+1}$	intra-fiber forces exerted by adjacent Rod $i + 1$
$\underline{M}^b$	Rotational Equation of Motion
$\underline{T}^H$	Hydrodynamic Torque
$T_k^H$	Hydrodynamic Torque of Bead k
$F_k^H$	Hydrodynamic Force
k	Number of Beads
$u_k^\infty$	Surrounding Fluid Velocity
a	Radius of a Bead
$u_k$	Velocity Bead k
$arOmega_k^\infty$	Vorticity of the Surrounding Fluid
$\omega_k$	Angular Velocity of the Bead k
М	Bending Moment
E	Young's Modulus
ρ	Radius of Curvature of a Beam
I	Inertial Moment
$\underline{F}^{N}$	Normal Force
$\underline{F}^T$	Tangential Force
$d_{ij}$	Distance Between Rod $i$ and Rod $j$
$\mu_f$	Coulomb Coefficient Between Fibers
$\Delta u_{ij}$	Relative Velocity Between Segment i and Segment j
$n_{\Phi}$	Intervals in Φ Direction
$B_0$	Distance Factor
P	Fraction of a Program that can be Parallelized
N	Number of Processing Units Used for Parallel Execution
$\sigma_u$	Ultimate strength

## 1. Introduction and Motivation

### 1.1. Introduction

The use of composite materials in industrial applications began when fiber composites were first developed in the 1940s [1]. This development significantly changed the manufacturing industry as it allowed industries to build lightweight products with performance comparable to that of metals and alloys. Fiber-reinforced composites are a unique material class with two main components: the matrix material and the reinforcing fibers [2]. By combining two phases, the composite has enhanced properties over the individual constituents. Discontinuous fiber-reinforced polymers play a significant role in transportation due to their lightweight performance and lower manufacturing costs [3-5]. In industry, injection molding and compression molding of long fiber-reinforced thermoplastics (LFTs) are widely used to produce parts with outstanding mechanical properties [6]. As fiber length is crucial in improving the mechanical performance of a molded product, an increase in fiber length correlates with the increased strength of the product. Researchers also found that parts are stronger in the direction of fiber alignment if both fiber length and volume fraction are increased [7]. However, fibers in the polymer melt often break during polymer processing because they are subjected to intense viscous forces during flow and deformation. Therefore, it is beneficial to understand the mechanism of fiber breakage during flow, particularly shear flow, which is dominant within the extrusion process. Understanding the fundamentals of fiber breakage will allow the user to optimize the process, ultimately reducing the length degradation and, thus, gaining better mechanical properties. However, there are still some aspects of processing that are not well understood. In addition to fiber length degradation, the development of anisotropy is another major factor determining molded

In addition to fiber length degradation, the development of anisotropy is another major factor determining molded parts' global and local properties [3]. The anisotropic properties of the molded parts are due to how fibers show a preferential alignment based on the flow conditions during the mold-filling process [8, 9]. As fiber alignment is crucial in determining the mechanical properties of parts, acquiring accurate predictions on fiber orientation is still an active research topic for academia and industry.

## 1.2. Objectives

The research objectives of this dissertation are divided into two parts. First, a simulation is conducted via a mechanistic model to understand the effect of fiber breaking curvature and the magnitude of penalty forces that prevent fibers from overlapping during simulation to the fiber damage in the polymer process. In addition, the probability of breakage is introduced to the system to increase the model's reliability and better describe the uncertainty of breakage in numerical terms. Moreover, to relieve the entanglement between fibers when generating an initial fiber cluster used for the simulation, a relaxation step is applied to reduce the initial breakage caused by an unsteady system. Then, the mechanistic model is used to predict the fiber breakage in a Couette flow rheometer [10]. By comparing the model's predictions to the experimental curve, the influence of adjusting parameters in the model to different conditions is assessed. In addition, the lack of maintenance of the algorithm leads to bugs during the simulation. To apply the mechanistic model more broadly, the algorithm also needs to integrate parallelization to fully utilize the cores in the computer and reduce the execution time for large data sets.

The second objective is to validate a new phenomenological approach to modeling fiber attrition developed at the Polymer Engineering Center (PEC). This validation is conducted by implementing the modified breakage model into Moldex3D and comparing it with experimental data. The model will be tested with different part geometry and processing conditions to analyze how different settings may affect the performance of the modified breakage model. In summary, the model can predict the number-average and weight-average of fibers and provide a better understanding of the length distribution during processing.

## 2. Literature Review

## 2.1. Processed Induced Fiber Orientation

During the manufacturing process, fiber orientation depends on two factors: fiber properties such as aspect ratio and length, and processing conditions, including injection speed and material viscosity [11, 12]. Fiber orientation strongly affects the mechanical properties of molded parts, leading to the development of several numerical models for predicting flow-induced fiber orientation. For a single rigid fiber in 3D space, its orientation can be defined by the orientation vector  $\mathbf{p}(\theta, \phi)$ , as shown in Figure 2.1 and equation (2.1).

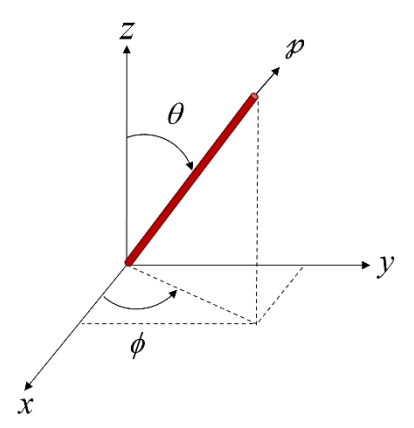


Figure 2.1 Unit vector p for orientation of a single rigid fiber in the Cartesian coordinate system.

$$\mathbf{p} = \begin{pmatrix} \mathbf{p_1} \\ \mathbf{p_2} \\ \mathbf{p_3} \end{pmatrix} = \begin{pmatrix} \cos\phi\sin\theta \\ \cos\theta\sin\phi \\ \cos\theta \end{pmatrix} \tag{2.1}$$

To characterize a composite material, using a single fiber to describe the overall fiber alignment is insufficient.

Instead, the orientation of the entire fiber population needs to be taken into consideration. The probability distribution function of orientation for a group of fibers is as follows:

$$\Psi = \Psi(\mathbf{p}) = \Psi(\theta, \phi) \tag{2.2}$$

The probability of a fiber existing between  $(\theta, \phi)$  and  $(\theta + d\theta, \phi + d\phi)$  can be given by  $\psi(\theta, \phi) \sin(\theta) d\theta d\phi$  [13]. A more concise way to describe fiber orientation is by using the second-order orientation tensor defined by Advani and Tucker [14] as below:

$$\mathbf{A} = \oint \Psi(\mathbf{p}) \mathbf{p_i} \mathbf{p_j} d\mathbf{p} = \begin{bmatrix} A_{11} & A_{12} & A_{13} \\ A_{21} & A_{22} & A_{23} \\ A_{31} & A_{32} & A_{33} \end{bmatrix}$$
(2.3)

where  $\mathbf{p_i}\mathbf{p_j}$  is a tensor product of the fiber orientation vector  $\mathbf{p}$ , and  $\oint \Psi(\mathbf{p}) d\mathbf{p}$  is an integral over all possible fiber orientations. In terms of the orientation distribution and the angle pair  $(\theta, \phi)$ , the tensor components can be calculated as follows [14]:

$$\mathbf{A} = \mathbf{p_i} \mathbf{p_j} = \begin{bmatrix} \sin^2 \phi \cos^2 \theta & \sin^2 \phi \cos \theta \sin \theta & \sin \phi \cos \phi \cos \theta \\ \sin^2 \phi \cos \theta \sin \theta & \sin^2 \phi \sin^2 \theta & \sin \phi \cos \phi \sin \theta \\ \sin \phi \cos \phi \cos \theta & \sin \phi \cos \phi \sin \theta & \cos^2 \phi \end{bmatrix}$$
(2.4)

By definition, the orientation is symmetric where  $A_{ij} = A_{ji}$  and its trace is equal to 1 where it leads to  $A_{11} + A_{22} + A_{33} = 1$ . A randomly placed fibers has the orientation of  $A_{11} = A_{22} = A_{33} = \frac{1}{3}$  while a unidirectional fiber orientation can described as  $A_{11} = 1$ ,  $A_{22} = A_{33} = 0$  as shown in Figure 2.2.

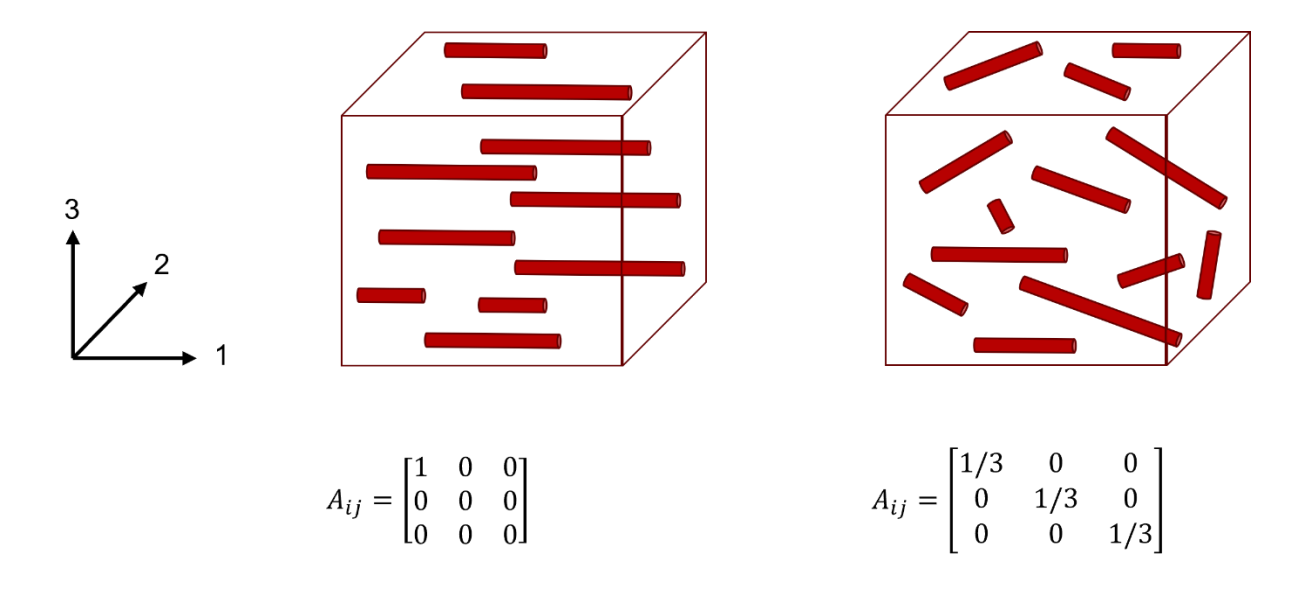


**Figure 2.2** Schematic representation of different orientation tensors: (a) unidirectional, aligned with axis 1, (b) random orientation.

## 2.2. Processed Induced Fiber Length Degradation

The outstanding mechanical performance of fiber-reinforced composites is carried out by transferring the applied load from the matrix to the reinforcing fibers. Keeping fiber lengths sufficiently long throughout the process remains a central objective in the industry [15, 16]. Fiber attrition can be described as the process of fibers breaking during processing, which inevitably leads to the length of the fibers being reduced from its initial value. Generally, the fiber length for long fiber-reinforced thermoplastic materials (LFRTs) is 15-30 mm before processing. In the finished part, fiber attrition may result in a distribution from 0.1 to a small fraction of fibers retaining their initial length (Figure 2.4).

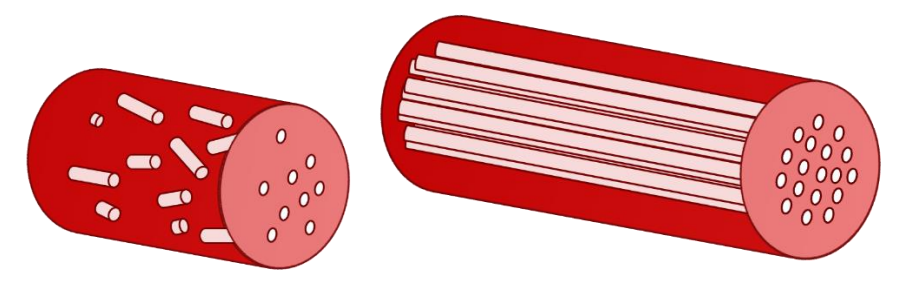


Figure 2.3 Schematic diagram of short fiber (Left) and long fiber pellets (Right).

Generally, the final fiber length is influenced by the specific process, the processing conditions, and materials [1, 15, 16]. Since mechanical properties depend on fiber length, it is desired to preserve the length of the fibers as much as possible by using processing conditions that treat the fibers more gently.

The fibers are subjected to different stresses throughout the process, including hydrodynamic effects, fiber-fiber interactions, and fiber-wall interactions. These may lead to fiber damage and reduce the average fiber length significantly in the finished part. For example, fiber length may be reduced to only 0.5 - 1.0 mm in the finished part for LFRT materials [16, 17].

As fibers are subjected to varying forces during manufacturing, there are different ways to characterize the fiber length. In addition to the statistic expression with the cumulative distribution, a single value description, including number-average length,  $L_N$ , and weight-average length,  $L_W$ , can also be used [18].

The number-average fiber length,  $L_N$ , is calculated as

$$L_N = \frac{\sum_{i=1}^{n} (N_i l_i)}{\sum_{i=1}^{n} (N_i)}$$
 (2.5)

The weight-average fiber length,  $L_W$ , takes into consideration the population of long fibers. This length is important for manufacturing parts with long fiber-reinforced materials as

$$L_w = \frac{\sum_{i=1}^n (N_i l_i^2)}{\sum_{i=1}^n (N_i l_i)}$$
 (2.6)

## 2.3. Prediction on Fiber Breakage

To estimate the final mechanical behavior of a product, it is necessary to predict the process-induced fiber breakage. Forgacs et al. [19] proposed that the critical shear stress that provokes fiber buckling is described by the Young's modulus of fibers and the fibers' geometrical properties. From this, it becomes clear that, with high aspect ratios, fibers tend to break under low loadings. Hinch [20] later demonstrated through applying the Slender Body theory that we could calculate and obtain the deformation of an ideally elastic particle in a shear flow. Using the Couette rheometer, Goris et al. [21] developed an experimental setup in combination with the fiber length measurement to obtain the repeatable length degradation of glass fibers at different fiber concentrations, initial fiber lengths, residence time, melt temperature, and processing speed. This setup provides good insight into measuring the fiber length. However, there's still no simulation tool that can accurately predict the final fiber length in a molded part, and the phenomenon of fiber breakage is not fully understood. Therefore, the numerical simulation is applied to investigate the phenomena of fiber breakage.

Some continuum models, which are very different from particle-level simulations, have been developed to obtain the macroscopic picture of breakage by solving the balance equation of fiber length distribution [4, 22]. Phelps et al. [4] presented a quantitative model to describe fiber attrition based on buckling as the driving mechanism for fiber breakage during processing. Phelp's model is based on three fitting parameters: the breakage coefficient (CB), the hydrodynamic drag coefficient ( $\zeta$ ), and the distribution shape factor (S). They defined the critical force needed to cause buckling ( $F_{crit}$ ) and the critical flow regimen ( $\dot{\gamma}_{crit}$ ) which would cause buckling as a function of fiber characteristics and flow parameters:

$$F_{\rm crit} = \frac{\pi^3 E_f D^4}{64 L_i^2} \tag{2.7}$$

$$\dot{\gamma}_{\rm crit} = \frac{\pi^3 E_f D^4}{4 \zeta \eta_m L_i^4} \tag{2.8}$$

where  $E_f$  is the Young's modulus, D is the fiber diameter,  $L_i$  is the fiber length,  $\eta_m$  is matrix viscosity, and  $\zeta$  is the drag coefficient. This model introduces a Normal or Weibull probability distribution that determines the location along the fiber's axis where failure is likely to occur. However, this approach does not consider the fiber breakage caused by fiber volume fraction, which ignores fiber-fiber interactions as a source of damage. A novel modified breakage model was then developed at the PEC by Bechara et al. [23].

$$L_{\infty} = \lambda \left(\frac{\sigma_u \, d_f^2}{\eta_m \dot{\gamma}}\right)^{0.5} \tag{2.9}$$

The coefficient  $\lambda$  is a material-dependent property and a measure of fiber-fiber interactions that cause fiber attrition during processing. The parameter is assumed to capture the effects of fiber concentration (fiber-fiber interactions) and fiber-wall interactions.  $\lambda$  as a function of fiber content as obtained from the measured  $L_{W\infty}$  values of the Couette rheometer experiment [23]. The linear correlation between  $\dot{\gamma}$  and  $k_f$  leads to a straightforward expression for the breakage rate coefficient:

$$k_f = \xi \dot{\gamma} \tag{2.10}$$

where  $\xi$  is a scale factor for the rate of deformation. Reducing the number of fitting parameters introduced when developing a model is beneficial since this makes the approach more robust and potentially reduces the number of experiments needed to determine such parameters [24].

To fully understand the micromechanical picture of fiber breakage, particle simulation is necessary to develop an understanding of the details of concentrated fiber suspension dynamics [25-29]. Until now, single particle models are not accurate enough and well developed to investigate the fiber-level degradation mechanisms due to expensive computation. Therefore, a particle-level model developed at the PEC at the University of Wisconsin-Madison will be extended to better understand fiber damage.

## 2.4. Fiber-Flow Coupling

Viscosity is one of the key factors that will affect the fiber motion inside the polymer flow. For example, the melt front of a circular disk in compression molding forms an elliptical shape instead of the circular shape observed by Ericsson et al. [30] and Dweib and O'Bradaigh [31]. Additionally, it has been found that the melt front of injection molding is not smooth. All of these phenomena are attributed to the anisotropic orientation of fibers during the process. The researchers have discovered that the orientation of the fibers affects the viscosity within the flow field, and changes in viscosity can also lead to varying fiber rotations. This phenomenon is referred to as fiberflow coupling. However, owing to the numerical challenges associated with computing highly anisotropic fluids, establishing a connection between fiber orientation and flow viscosity has remained challenging. Recently, Favaloro et al. [32, 34] developed a new fiber-suspension constitutive equation for the Informed-Isotropic (IISO) viscosity model for concentrated fiber suspensions in non-linear viscous fluids to couple flow field and fiber orientation:

$$\mathbf{\tau} = 2\eta_S(\dot{\gamma})\mathbf{D} + 2\eta_S(\dot{\gamma})R_T(\dot{\gamma})\frac{\mathbf{D}: \mathbf{A}_4: \mathbf{D}}{\mathbf{D}: \mathbf{D}}\mathbf{D}$$
(2.11)

where  $\eta_S(\dot{\gamma})$  is the shear viscosity of the Cross viscous fluid with fibers;  $R_T(\dot{\gamma})$  is the famous Trouton ratio

$$\mathbf{\tau} = 2\eta_m \mathbf{D} + 2\eta_m \varphi N_p \mathbf{D} : \mathbf{A}_4 \tag{2.12}$$

where  $\tau$  is the extra stress tensor; **D** is the rate-of-deformation tensor;  $\eta_m$  is the matrix viscosity;  $\varphi$  is the fiber volume fraction;  $N_P$  is a dimensionless parameter. The scalar viscosity is developed which depends on the orientation state and the deformation mode. Specifically, the viscosity function varies as the deformation mode is rotated with respect to the orientation state.

The A<sub>4</sub> used in the flow-fiber coupling model is calculated based on the Improved ARD Model and Retarding Principal Rate Model (iARD-RPR model) proposed by Tseng et al [35, 36, 37].

$$\dot{\mathbf{A}} = \dot{\mathbf{A}}^{\mathsf{HD}} + \dot{\mathbf{A}}^{\mathsf{iARD}}(C_{I_{I}}C_{M}) + \dot{\mathbf{A}}^{\mathsf{RPR}}(\alpha) \tag{2.13}$$

The iARD-RPR model uses only three physical parameters: a fiber-fiber interaction parameter  $C_I$ , a fiber-matrix interaction parameter  $C_M$ , and a slowdown parameter  $\alpha$ .

$$\dot{\mathbf{A}}^{\text{HD}} = (\mathbf{W} \cdot \mathbf{A} - \mathbf{A} \cdot \mathbf{W}) + \xi(\mathbf{D} \cdot \mathbf{A} + \mathbf{A} \cdot \mathbf{D} - 2\mathbf{A}_4: \mathbf{D})$$
(2.14)

$$\dot{\mathbf{A}}^{\mathrm{iARD}} = \dot{\gamma} [2\mathbf{D}_r - 2\mathrm{tr}(\mathbf{D}_r)\mathbf{A} - 5\mathbf{D}_r \cdot \mathbf{A} - 5\mathbf{A} \cdot \mathbf{D}_r + 10\mathbf{A}_4 : \mathbf{D}_r]$$
 (2.15)

$$\mathbf{D}_r = C_I \left( \mathbf{I} - C_M \frac{\mathbf{D}^2}{\|\mathbf{D}^2\|} \right) \tag{2.16}$$

$$\dot{\mathbf{A}}^{\text{RPR}} = -\mathbf{R} \cdot \dot{\Lambda}^{\text{IOK}} \cdot \mathbf{R}^{\text{T}} \tag{2.17}$$

The intrinsic orientation kinetics (IOK) assumption [38]

$$\dot{\Lambda}_{ii}^{\rm IOK} = \alpha \dot{\lambda}_i$$
, where  $i, j, k = 1, 2, 3$  (2.18)

 $\dot{\lambda}_i$  is eigenvalues of  $A, \lambda_1 \ge \lambda_2 \ge \lambda_3$ ;  $R = [e_1 \quad e_2 \quad e_3]$  is defined by eigenvector columns of A.

$$\|\mathbf{D}^2\| = \sqrt{\frac{1}{2}\mathbf{D}^2:\mathbf{D}^2}$$
 (2.19)

The iARD-RPR model has been implemented into a commercial injection molding simulation software, Moldex3D, to allow fiber orientation predictions.

## 3. Direct Fiber Simulation

## 3.1. Theoretical background

The mechanistic model, based on the work done by Schmid et al. [26], models fibers as chains of rigid cylindrical rods, as shown in Figure 3.1. At each segment node in a fiber, the position  $x_i$ , the velocity  $u_i$  and the angular velocity  $\omega_i$  are calculated. Additionally, the segments experience hydrodynamic effects, fiber-fiber interactions, excluded volume effects, and elastic deformation within the flow field.

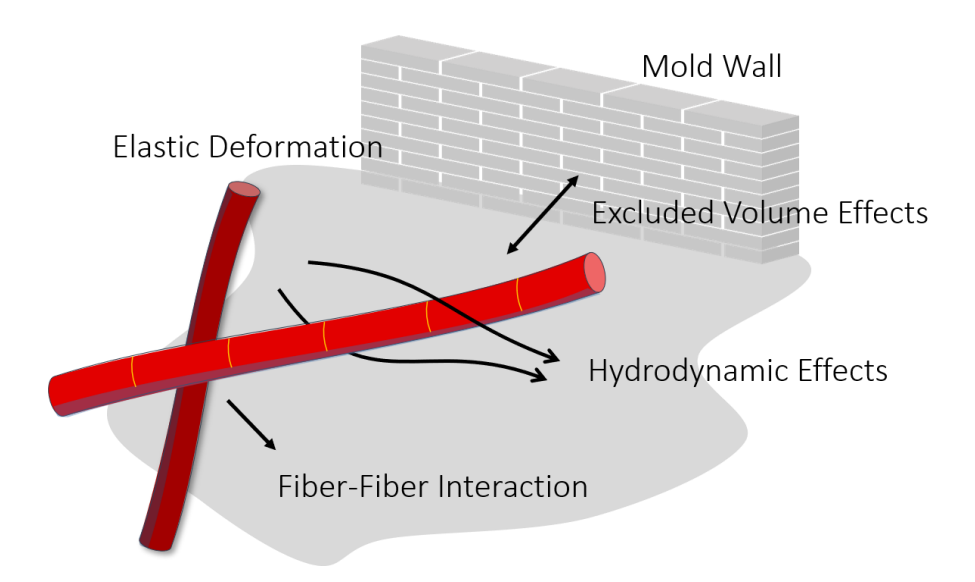


Figure 3.1 Particle level simulation: modeling single fiber and macroscale interactions.

The fibers are immersed in a homogeneous shear flow at a low Reynolds number; therefore, inertial effects can be neglected based on the experiments by Hoffman [39] and Barnes [40]. In addition, long-range hydrodynamic interactions are neglected due to the high viscosity of the polymer [41]. Furthermore, as fluid forces are not high enough to cause fibers to stretch or have torsional deformation, only bending deformation is included in the model. Buoyant effects are neglected as well [42, 43].

The excluded volume force, implemented as a discrete penalty method, stops fibers from overlapping and is used to model inter-fiber interaction. Discretizing the fibers into more than two nodes or one beam allows fiber bending

to occur, where the back coupling from fiber motion to fluid is not considered due to expensive computational costs [42]. The translational equations of motion are written as

$$\underline{0} = \underline{F}_{i}^{H} + \sum_{j} \underline{F}_{ij}^{C} + \underline{X}_{i} - \underline{X}_{i+1}$$
(3.1)

where  $\underline{F}_i^H$  are the drag forces from the surrounding fluid,  $\underline{F}_{ij}^C$  is the inter-fiber interaction force with rod, j, and  $\underline{X}_i$ ,  $\underline{X}_{i+1}$  are the intra-fiber forces exerted by adjacent rods.

Likewise, the rotational equation of motion is analogous but includes an elastic recovery term,  $\underline{M}^b$ , and a hydrodynamic torque,  $\underline{T}^H$ :

$$\underline{0} = \underline{T}_i^H - \underline{r}_i \times \underline{X}_{i+1} + \sum_j \underline{r}_{ii} \times \underline{F}_{ij}^C + \underline{M}_i^b - \underline{M}_{i+1}^b$$
(3.2)

Additionally, if a fiber has more than one segment; an extra constrain that enforces connectivity between the different segments is used:

$$0 = u_i + w_i \times r_i - u_{i+1} \tag{3.3}$$

Using a chain of beads to represent the rod-like geometry of a fiber for the hydrodynamic effects reduces the complex solution compared to an ellipsoid geometry [44]. The hydrodynamic force  $F_i^H$  is calculated as the summation of forces experienced by the beads  $F_k^H$  and is given as:

$$\underline{F}_{i}^{H} = \sum_{k=1}^{m} \underline{F}_{k}^{H} \tag{3.4}$$

where  $\underline{F}_{k}^{H}$  is the hydrodynamic force and k describes the number of beads given by the Stokes law as seen below:

$$\underline{F}_k^H = 6\pi\mu\alpha(\underline{u}_k^\infty - \underline{u}_k) \tag{3.5}$$

where  $u_k^{\infty}$  is the surrounding fluid velocity, a is the radius of the bead and  $u_k$  is the velocity bead k which can also be represented as  $(u_k = u_i + \omega_i \times r_k)$ . This allows the final  $F_i^H$  equation to be written as shown below

$$\underline{F}_{i}^{H} = 6\pi\mu a \left( \sum_{k=1}^{m} \underline{u}_{k}^{\infty} - m\underline{u}_{i} - \underline{w}_{i} \times \sum_{k=1}^{m} \underline{r}_{k} \right)$$
(3.6)

Similarly, the torque exerted on a rod is:

$$\underline{T}^H = \sum_{k=1}^m \underline{T}_k^H \tag{3.7}$$

where the hydrodynamic contribution  $T_k^H$  of bead k where  $\Omega_k^{\infty}$  is the vorticity of the surrounding fluid and  $\omega_k$  is the angular velocity of the bead k.

$$\underline{T}_k^H = 8\pi\mu a^3 \left(\underline{\Omega}_k^{\infty} - \underline{w}_k\right) + 6\pi\mu a\underline{r}_k \times \left(\underline{u}_k^{\infty} - \underline{u}_i - \underline{w}_i \times \underline{r}_k\right) \tag{3.8}$$

By substituting the expression of  $T_k^H$ , the expression of  $u_k$  into the fluid's vorticity can be written as:

$$\underline{T}^{H} = 8\pi\mu a^{3} \left( \sum_{k=1}^{m} \underline{\Omega}_{k}^{\infty} - m\underline{w}_{i} \right) + 6\pi\mu a\underline{r}_{k} \times \left( \sum_{k=1}^{m} \left( \underline{r}_{k} \times \underline{u}_{k}^{\infty} \right) + \underline{u}_{i} \times \sum_{k=1}^{m} \underline{r}_{k} - \sum_{k=1}^{m} \underline{r}_{k} \times \left( \underline{w}_{i} \times \underline{r}_{k} \right) \right)$$
(3.9)

Using elastic beam theory, the approach below resembles Schmid's [30]. The bending moment of a fiber where the radius of curvature of a beam subjected to pure bending is given by:

$$\frac{1}{\rho} = \frac{M}{EI} \tag{3.10}$$

where M is the bending moment, E the Young's modulus,  $\rho$  the radius of curvature of the beam, and I is the inertial moment of the beam's cross section.

Approximation by linear segments which connected with elastic joints, the bending moment will be then:

$$\underline{M}_{i}^{b} = \frac{\alpha IE}{\rho} \underline{e} \tag{3.11}$$

$$\underline{e} = \frac{\underline{r_i} \times \underline{r_{i-1}}}{|\underline{r_i} \times \underline{r_{i-1}}|} \tag{3.12}$$

The model also includes mechanical interaction between fibers. The fiber-fiber interaction force is the sum of a normal force and a tangential force as seen below where  $\underline{F}^N$  is the normal force, and  $\underline{F}^T$  is the tangential force representing the friction between rods.

$$\underline{F}_{ij}^{C} = \underline{F}_{ij}^{N} + \underline{F}_{ij}^{T} \tag{3.13}$$

The collision response between fibers is represented as a discrete penalty method [45, 46]. The penalty method implemented in the model starts with selecting a force dependent on the penetration distance. The equation below of the excluded volume force is often used in a particle-level simulation for fiber suspension [26, 47-48] where A and B are parameters [49, 50],  $d_{ij}$  is the shortest distance between rod i and rod j, r is the fiber radius, and  $\underline{n}_{ij}$  is

the vector along the closest distance between the rods.

$$\underline{F_{ij}^{N}} = A \exp\left[-B\left(\frac{2d_{ij}}{r} - 2\right)\right] \underline{n}_{ij} \tag{3.14}$$

The force increases exponentially as fibers get closer. In this research, *B* is chosen as 2 [42], and *A* is tuned for each system, represented as an excluded volume force constant later.

The friction force between segment i and j is calculated as a force in the direction of the relative velocity of the rods and is computed using the equation below, where  $\mu_f$  is the coulomb coefficient between fibers and  $\Delta u_{ij}$  is the relative velocity between segments i and j.

$$\underline{F}_{ij}^{T} = \mu_f |\underline{F}_{ij}^{N}| \frac{\Delta u_{ij}}{|\Delta u_{ij}|}$$
(3.15)

Due to non-linear behavior, the model calculates future steps using the previous time step. For this reason, the initial time step is zero to avoid missing data points.

## 3.2. Sample Preparation

The mechanistic model simulates the motion of a bundle of fibers in a cell. To start a direct fiber simulation, one needs to prepare a fiber cluster that represents the actual fiber placement of a realistic part, including the fiber length and the fiber orientation. The algorithm requires sufficient fiber information to construct a cluster that can represent the whole picture of a process.

### 3.2.1. Improve the procedure of the cluster preparation.

Due to program limitations in the past, users were restricted to generating clusters with a maximum volume fraction of 2.5% and were then compelled to compress the cluster afterward to attain the desired volume fraction of fiber bundles. However, this compression frequently resulted in alterations to fiber orientation, as it forced the fibers to realign within the fiber cluster, particularly in materials with higher fiber content. Improvements are necessary to achieve a more accurate representation of the fiber bundle in its original state.

The mechanistic model is utilized to simulate the motion of fibers under specific types of flows. To initiate this, generating a cluster that accurately reflects the real experimental environment is very important. In polymer processes, it's commonplace for fibers to be randomly distributed within space. Therefore, generating a cluster with an orientation tensor approximately equal to [0.33, 0.33, 0.33] is essential for a more precise simulation of the process. However, due to the limitations of the numerical methods used in the Cluster Generation code, the program can only generate a randomly placed cluster in the  $a_{11}$  and  $a_{22}$  directions. It proves to be quite challenging to generate a cluster that is random in every angle, including  $a_{11}$ ,  $a_{22}$ , and  $a_{33}$ . In other words, the program initially generates a cluster with planar orientation in  $a_{11}$  and  $a_{22}$ , while the value for  $a_{33}$  remains only 0.01. Moreover, for high-concentration fibers, the process becomes time-consuming. As an additional step, Pre-Compression, is required to compress the fibers and attain the desired volume fraction before executing the shear cell model. Furthermore, the Pre-Compression step doesn't guarantee the achievement of the desired orientation, as compressing the cell also affects its orientation.

To address the limitations of the current Cluster-Generating code, a new conceptual method, the Randomly Placed Method, is introduced to the preparation process, as demonstrated below.

#### Randomly-Placed Method

First, the model uses the spherical coordinate to describe each fiber's position as Figure 3.2.

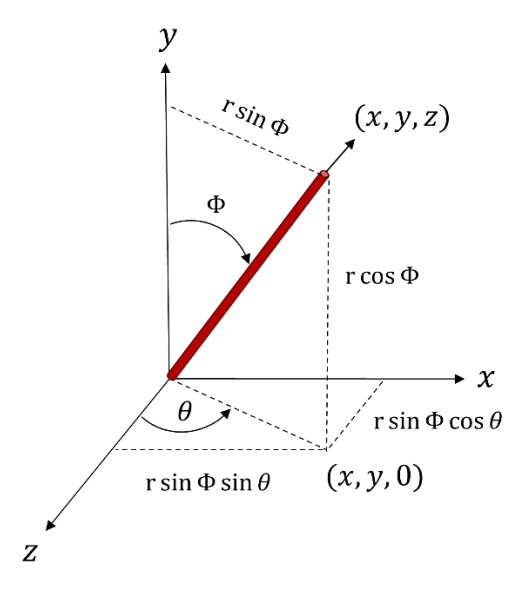


Figure 3.2 An example of the spherical coordinate used in generating the fiber positions.

$$x = r\sin\Phi\sin\theta \tag{3.16}$$

$$y = r\cos\Phi \tag{3.17}$$

$$z = r \sin \Phi \cos \theta \tag{3.18}$$

$$0 \le \theta \le 2\pi, \qquad 0 \le \phi \le \pi \tag{3.19}$$

Then, based on the number of fibers, one determines how many intervals are going to be divided on the surface of the sphere by inputting the  $n_{\Phi}$ , the intervals in  $\Phi$  direction.

$$dA = r^2 \sin \Phi \, d\theta \, d\Phi \, \underline{F}_{ij}^C = \underline{F}_{ij}^N + \underline{F}_{ij}^T \tag{3.20}$$

The interval of  $\theta$  in each layer between  $\Phi_i$  and  $\Phi_{i+1}$  is then calculated by  $\Delta\theta$  in the first layer ( $\Phi_1$  and  $\Phi_2$ ). Set r=1, then:

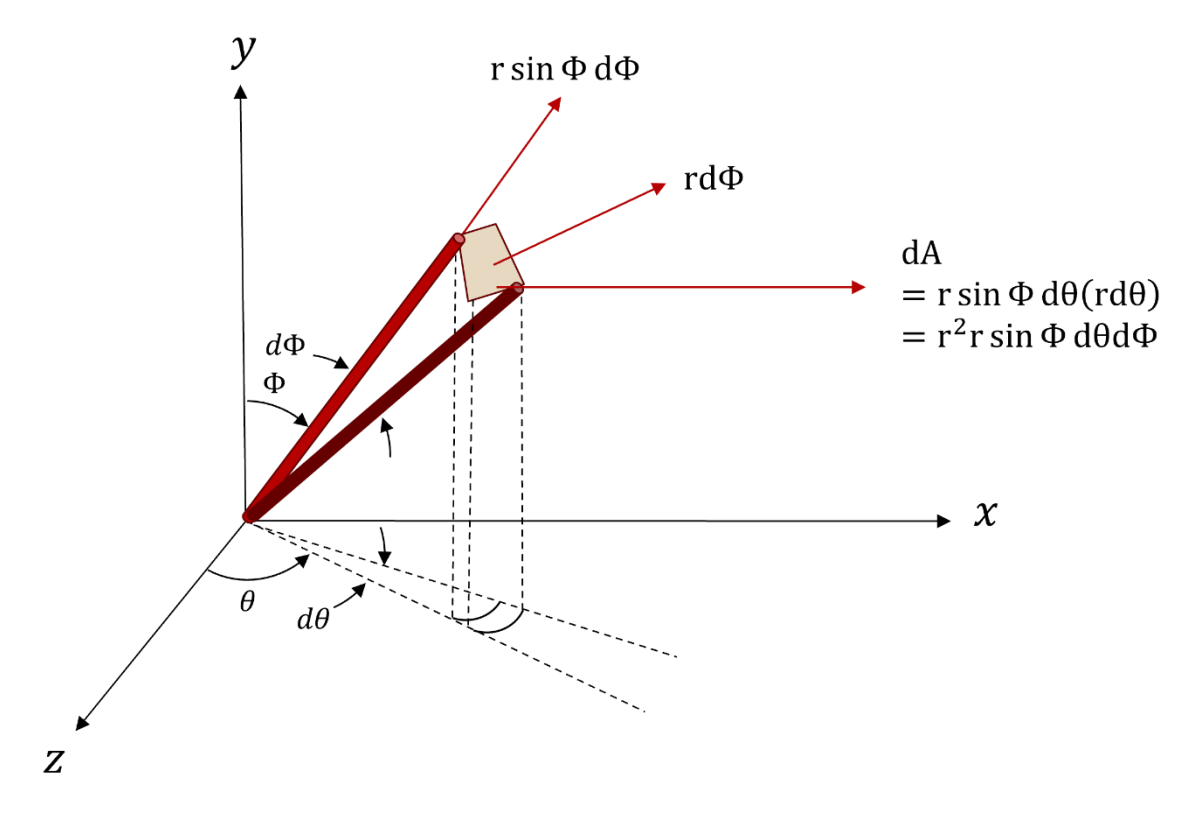


Figure 3.3 An example of the differential area when generating the fiber positions.

$$dA = \sin \Phi \, d\theta \, d\Phi \tag{3.21}$$

$$\int dA = \int_{0}^{\pi} \int_{0}^{2\pi} \sin \Phi \, d\theta \, d\Phi \tag{3.22}$$

$$\int dA = 2\pi \int_{0}^{2\pi} \sin \Phi \, d\Phi \tag{3.23}$$

Finally, one randomly chooses a fiber and places it in a small box.

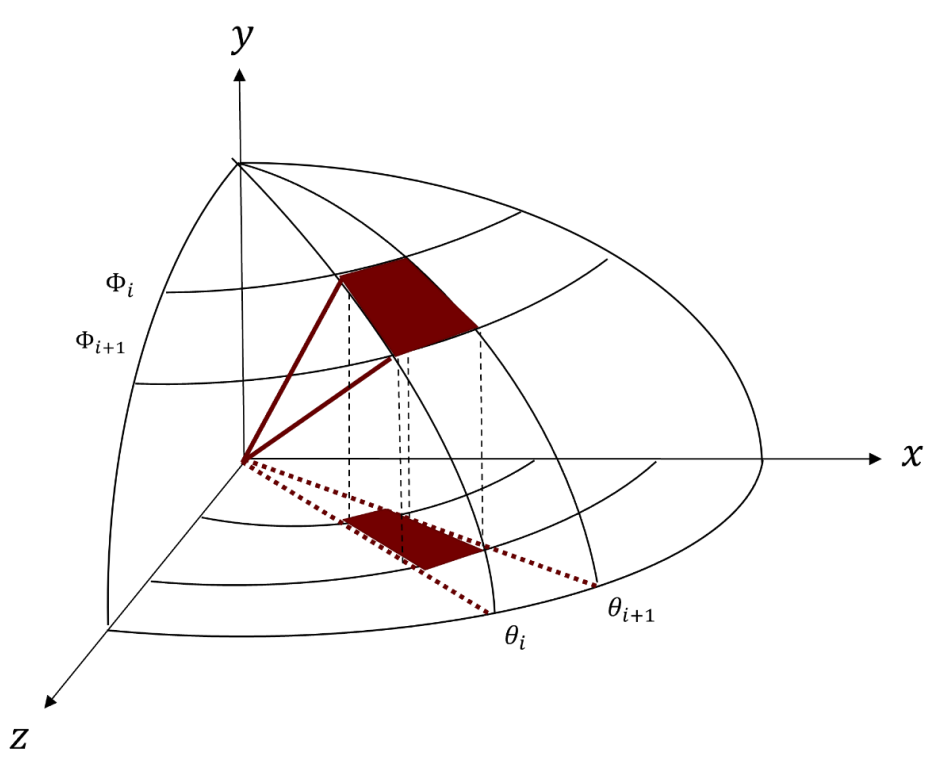


Figure 3.4 Fiber distribution and projection plane.

$$A_i = 2\pi \int_{\Phi_i}^{\Phi_{i+1}} \sin \Phi \, d\Phi \tag{3.24}$$

$$A_i = 2\pi(\cos\phi\Phi_i - \cos\Phi_{i+1}) \tag{3.25}$$

$$\Delta \Phi = \frac{\pi}{N} \tag{3.26}$$

Choose *N* equals to 16, 32, 64, 128, then:

$$\Phi_{\rm i} = i\Delta\Phi = \left(\frac{i}{N}\right)\pi\tag{3.27}$$

## Flow Chart for Random-Placed Method

The flowchart for the model is displayed below. Four steps are involved to generate a random orientation: inputting data, calculating angles, placing fibers, and outputting data.

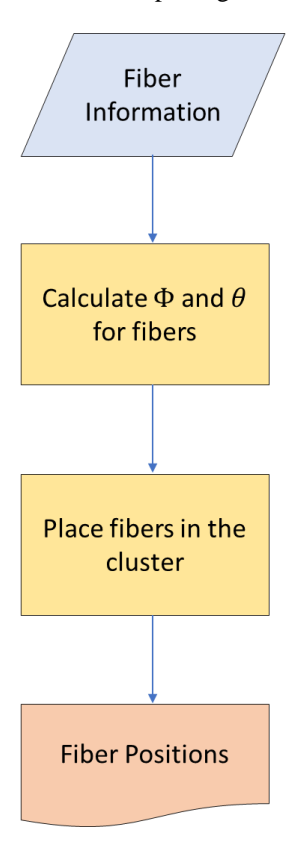


**Figure 3.5** The flow chart of generating a fiber cluster with randomlu placed position of fibers integrated into the algorithm.

#### Limitation

While the computational time for preparing a cluster before applying it to the shear cell can decrease from days to a few seconds, depending on the size and concentration of fibers, this new model is currently limited to generating randomly placed clusters. The next step involves utilizing and expanding this concept to generate a predetermined desired orientation set by users.

#### Pre-determined Orientation Method

In order to attain the desired fiber orientation, distinct from random orientation, the orientation tensor can be conceptualized as a linear combination, divisible into three components. Each component corresponds to a

different dimensionality—ranging from one to three dimensions. An example of such linear combinations is as follows:

For the orientation tensor  $[a_{11}, a_{22}, a_{33}] = [0.6, 0.3, 0.1]$ :

$$\begin{bmatrix} 0.6 & & \\ & 0.3 & \\ & & 0.1 \end{bmatrix} = \begin{bmatrix} 0.1 & & \\ & 0.1 & \\ & & 0.1 \end{bmatrix} + \begin{bmatrix} 0.2 & & \\ & & 0.2 & \\ & & & 0 \end{bmatrix} + \begin{bmatrix} 0.3 & & \\ & & 0 & \\ & & & 0 \end{bmatrix}$$
(3.28)

Each term can be described as a ratio of a random orientation with different dimensions:

$$\begin{bmatrix} 0.6 & & \\ & 0.3 & \\ & & 0.1 \end{bmatrix} = 0.3 \begin{bmatrix} 1/3 & & \\ & 1/3 & \\ & & 1/3 \end{bmatrix} + 0.4 \begin{bmatrix} 1/2 & & \\ & 1/2 & \\ & & 0 \end{bmatrix} + 0.3 \begin{bmatrix} 1 & & \\ & 0 & \\ & & 0 \end{bmatrix}$$
(3.29)

Then, to generate a cluster with the orientation [0.6, 0.3, 0.1], three subclusters of varying sizes are prepared per their ratios and three different orientations along the three dimensions [1/3, 1/3, 1/3], two dimensions [1/2, 1/2, 0], and one dimension [1, 0, 0]. However, the matrices presented above are diagonal matrices that signify the principal directions of fibers. If all nine tensors are to be employed in the program, an orthogonal transformation is necessary beforehand to derive the diagonal matrices from the original nine orientation tensors using eigenvalues and eigenvectors.

Lastly, the process involves combining three subclusters and following the steps outlined in the Randomly-Placed Method to position fibers within small boxes. In essence, this method can be applied to describe every orientation tensor.

### Flow Chart for Pre-determined Orientation Method

The steps for generating a predetermined orientation are similar to those of the Randomly Placed method. The distinction lies in the requirement of an additional step, involving the division of orientation tensors into three different dimensions, followed by the subsequent combination of three subclusters. The flowchart for this method is displayed below (Figure 3.6).

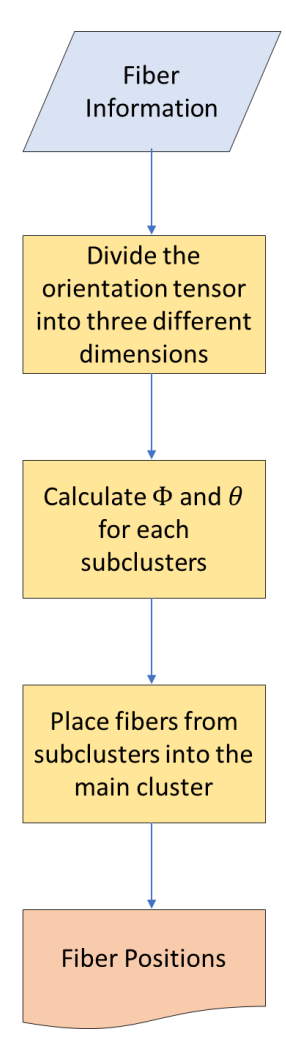


**Figure 3.6** The flow chart of generating a fiber cluster with a predetermined orientation integrated into the algorithm.

## Results

An example of an orientation tensor is shown below (Figure 3.7). A cluster with 5 wt% and its diagonal matrix of

$$\begin{bmatrix} a_{11}, & a_{22}, & a_{33} \end{bmatrix} = \begin{bmatrix} 0.6, & 0.3, & 0.1 \end{bmatrix} \text{ was transformed from } \begin{bmatrix} 0.34444 & -0.17778 & 0.15556 \\ -0.17778 & 0.41112 & -0.02222 \\ 0.15556 & -0.02222 & 0.24444 \end{bmatrix} \text{ by using }$$
 the eigenvalues = 
$$\begin{bmatrix} 0.66667 & 0.33333 & 0.66667 \\ -0.66667 & 0.66667 & 0.33333 \\ 0.33333 & 0.66667 & -0.66667 \end{bmatrix} .$$

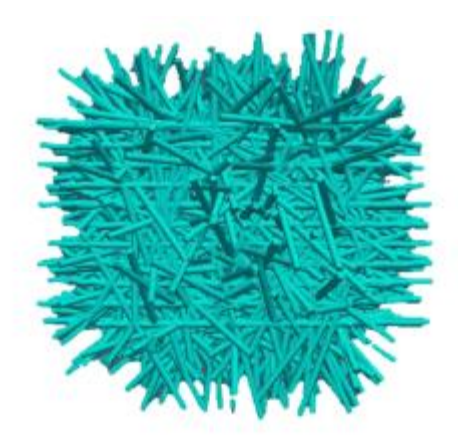


Figure 3.7 A 5 wt% cluster with 1331 fibers which orientation tensor  $[a_{11}, a_{22}, a_{33}] = [0.6, 0.3, 0.1]$ .

With this concept, fibers can be placed inside the box regardless of the concentration of the cluster. In other words, there's no need to execute the Pre-Compression step, as the fibers are already positioned within the desired box size. Additionally, there's no concern about achieving the desired orientation after the Pre-Compression step, as the end-use cluster is already generated. Following the generation of the cluster, the cell is subjected to the relaxation step. This step involves allowing fibers to pre-stretch using a very low shear rate, which prevents initial breakage caused by abnormal angles between nodes within a fiber. This process also aids in separating fibers that might overlap when placed in the box by utilizing excluded volume forces. When the distance between two fibers is smaller than their radius, the excluded volume forces will push the fibers apart from each other.

### 3.2.2. Implementing Fiber Length Distribution

The mechanistic model offers the advantage of simulating the behavior of a bundle of fibers under various flow conditions, both at the beginning and in the middle of a polymer process. When the model is applied to the start of the process, there is no issue in preparing a cluster, as the fibers remain unbroken and possess uniform lengths. However, clusters start exhibiting length distributions as fibers begin to break, particularly with longer fibers. If one initiates the simulation in the middle of the process, where a length distribution already exists as the initial state, the current program cannot reflect these different fiber lengths in the cluster. Fibers typically exhibit a length distribution after undergoing shear stress conditions. However, the current program could only generate uniform fiber lengths rather than those with a length distribution. Here, the fiber length distribution function is introduced

as input for cluster generation. Below shows the steps of integrating the length distribution when generating a fiber cluster for later simulation. To begin, it's necessary to prepare the fiber length distribution with the *initial histogram.in.*, as depicted in Figure 3.8.

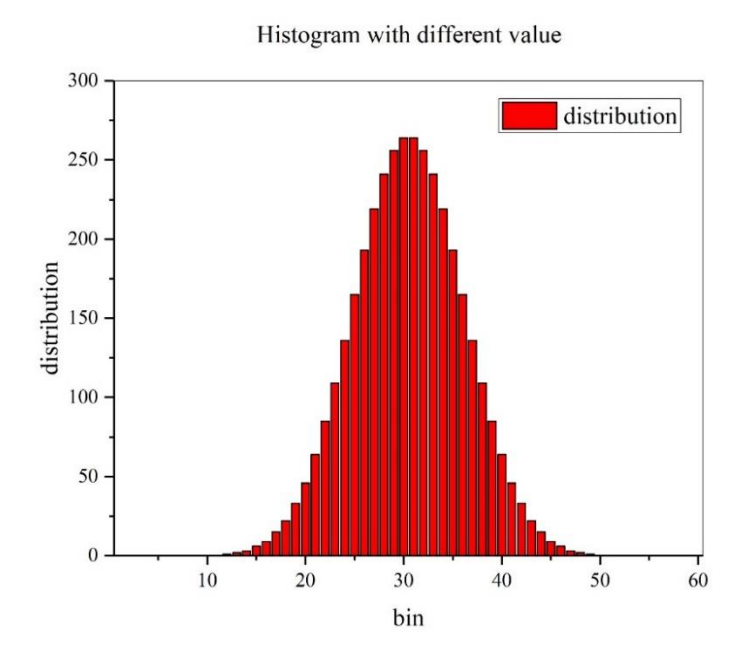


Figure 3.8 An example of fiber length distribution as an input for generating initial fiber cluster.

Next, it's necessary to check the probability, Equation (3.30), of each length placed in the bin(i) based on the  $initial\_histogram.in$  from the input folder.

Probability(i) = 
$$\frac{\text{bin heights}(i)}{\sum_{i=1}^{nbr \ bins} \text{bin heights}(i)} \underline{F}_{i}^{H} = 6\pi\mu a \left( \sum_{k=1}^{m} \underline{u}_{k}^{\infty} - m\underline{u}_{i} - \underline{w}_{i} \times \sum_{k=1}^{m} \underline{r}_{k} \right)$$
(3.30)

$$fiber(jL) \text{ in } bin(i) = \frac{\text{total segments of fiber}(jL) \times \text{probability}(i)}{\text{nbr segments of } jL}$$
(3.31)

Third, place all the fibers into bins according to the initial histogram file, starting with the shortest length (jL = 1), by determining how many fibers can be allocated to each bin(i). Next, distribute these fibers into bin(i) based on a Probability(i). Afterward, identify the available space to accommodate the remaining segments from the same fibers and allocate them to bin(i). Repeat this process until all the lengths generated in the histogram file have been placed in the cluster. With the steps mentioned above, the algorithm is able to generate a cluster with fiber length distribution.

## 3.3. Fiber Attrition Simulation

The general procedure of the direct fiber simulation can be described as shown in Figure 3.9. The preprocessing, cluster generation, includes organizing the fiber orientation and fiber length distribution information to generate a cluster that can represent the actual situation of the process. Once a bundle of the desired properties has been generated, the processing conditions and the computational setting along with the fiber position files from the cluster generation will be input into the shear cell algorithm. With the stored fiber positions during the computation, the algorithm is able to calculate the changes in fiber lengths and fiber orientation. Furthermore, the algorithm can capture the distribution of breakage curvature segment distances to further analyze how fiber motion and fiber rotation may impact the fiber breakage.

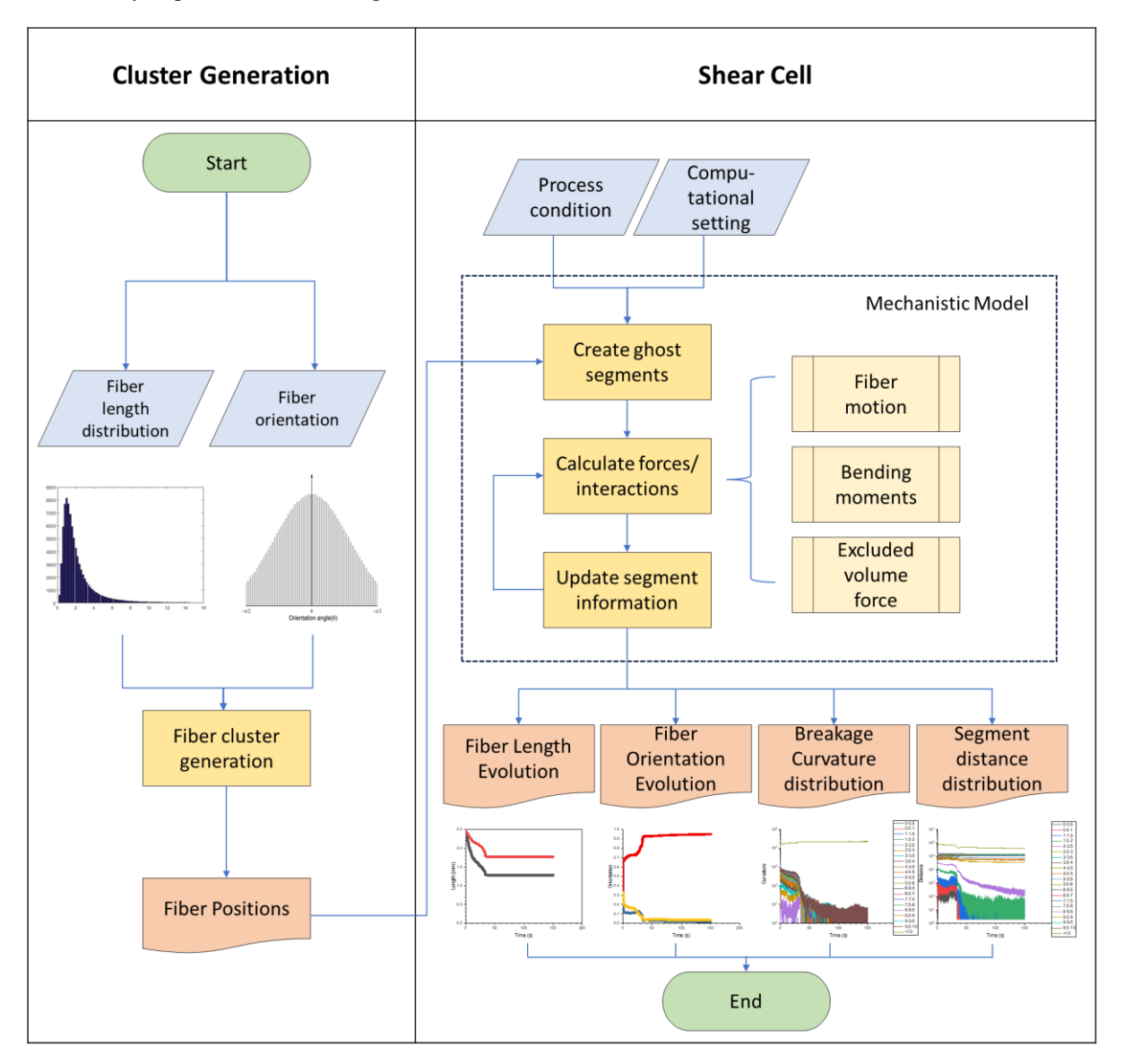


Figure 3.9 The flow chart of the Direct Fiber Simulation.

## 3.3.1. Update in the Program

Since the mechanistic model stores segment information to calculate the relative fiber motion for the next time step, it can compute the corresponding fiber orientation and length based on the segment's location within the defined box. However, due to a lack of maintenance after the code was initially developed, certain defects in the coding structure emerged, leading to unrealistic model performance, as depicted in Figure 3.10. For instance, in Figure 3.10, fibers of the same length exhibit varying rotational behaviors if divided into different segments. As a result, the code itself requires thorough diagnosis and maintenance.

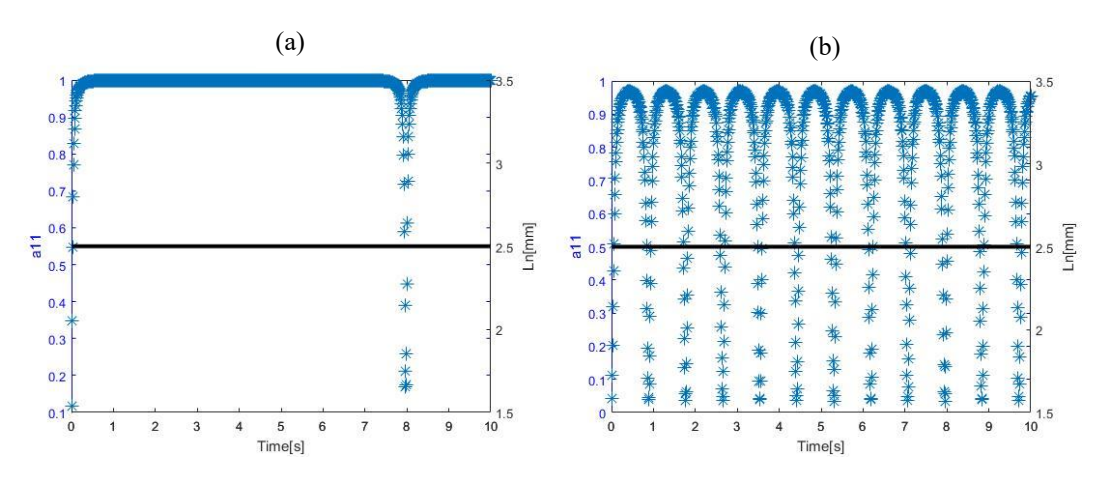


Figure 3.10 The orientation result in  $a_{11}$  direction using different number of segments to represent a single fiber: (a) 10 segments in a single fiber, (b) 25 segments in a single fiber.

#### The update

The program's structure and variables have been redefined to allow easier maintenance of the code and the potential to adapt the parallelization of the algorithm. For fiber motion, nine governing equations are employed to calculate the movement of each segment. The program can now store fiber locations in local and global matrices. Velocity profiles of each segment are now stored in separate variables, and hinge information is updated independently. To facilitate the simulation of a larger quantity of fibers simultaneously, periodic boundary conditions have been incorporated into the program. This is achieved by updating the calculation of boxes for ghost segments to align with the Lee Edward Boundary theory [51]. All image boxes have been corrected based on the Lee Edward theory. The handling of ghost segment information follows a different order now, and a new

method for calculating the location of ghost segments has been implemented. Additional program updates include updating fiber interaction forces by correcting the Distance Factor ( $B_0$ ) in calculating fiber interaction forces in equation (3.14).  $B_0$  is used to prevent the overlapping between fibers and to determine how many neighborhood segments should be considered when calculating the interaction forces.

In addition, the algorithm was only allowed to set a fixed dt during the computation. If an insufficient dt is selected, the result will not converge as shown in Figure 3.11 below.

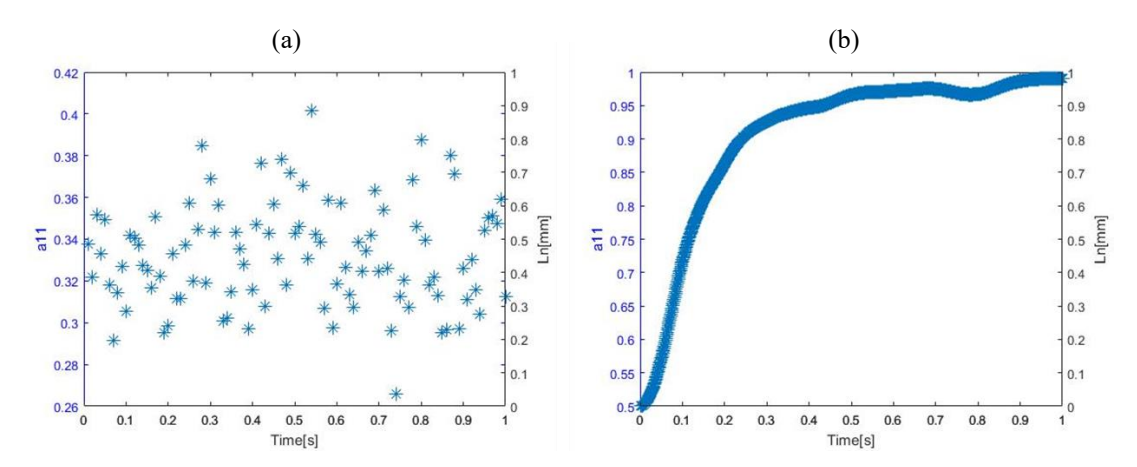


Figure 3.11 The orientation result in  $a_{11}$  direction with fixed dt set for the simulation: (a)  $dt = 10^{-5}$ , (b)  $dt = 10^{-6}$ .

To improve the process of calculating displacement using the provided time interval, denoted as dt, the time step is now automatically adjustable. Initially, the objective involves evaluating the displacement value based on the given input dt. Moreover, a benchmark for the minimum acceptable displacement, set at 10<sup>-10</sup>, is established in the algorithm. At each time step, a comparison is conducted between the displacement computed using the input dt and a predefined maximum displacement threshold. If the calculated displacement exceeds this threshold, an adjustment is triggered by activating the iteration variable and leads to a smaller dt. Then, the ratio is assessed, and if found to be greater than 1, the input dt is determined to be feasible. This implies that the displacement attained through the input dt remains sufficiently modest, rendering any further dt adjustments unnecessary. Lastly, the algorithm calculates the new displacement using the adjusted dt. Here, it demonstrates how the auto dt improves the computation stability and reduces computational time. The validation test was conducted with a cluster with fiber length of 0.25 mm and fiber content of 10 wt% as shown in Table 1. The simulations were run

for a duration of 0.1 second, allowing a comparison of the time costs for each condition.

**Table 1** The test input for evaluating the performance of adjusted dt with the mechanistic model.

	Fiber Cluster
Fiber Content	10 wt%
Fiber Length	0.25 mm
Fiber Aspect Ratio	5.26
<b>Number of Fibers</b>	138

Table 2 presents the necessary computational times for various preset values of dt in the simulation. Initially, a maximum value of  $dt = 10^{-6}$  is necessary to achieve convergence in the orientation computation. When a smaller value of dt, such as  $dt = 10^{-7}$ , is employed in the simulation, the required time increases by a factor of 10 compared to the original time. However, with the auto-adjust time step feature, the program now utilizes nearly the same computational time while delivering excellent performance in the simulation.

**Table 2** The time cost of different dt used in the simulation.

	Fixed Time Step, $dt = 10^{-6}$	Fixed Time Step, $dt = 10^{-7}$	Auto-adjust Time Step, $dt = 10^{-6} \sim 10^{-8}$
Computational Time	70.24 s	696.98 s	70.31 s

Additionally, with the integration of the auto-adjust time step into the algorithm, a significant improvement in algorithm stability is observed, as depicted in Figure 3.12. Previously, the orientation result in the  $a_{11}$  direction would not converge if an inappropriate dt was employed in the program. However, the algorithm can determine an appropriate dt that yields reasonable results after the update. Figure 3.12 illustrates that even when a smaller dt such as  $10^{-5}$  is initially set as an input, the program dynamically adjusts the dt during computation, resulting in performance equivalent to that achieved with a smaller dt such as  $10^{-6}$ .

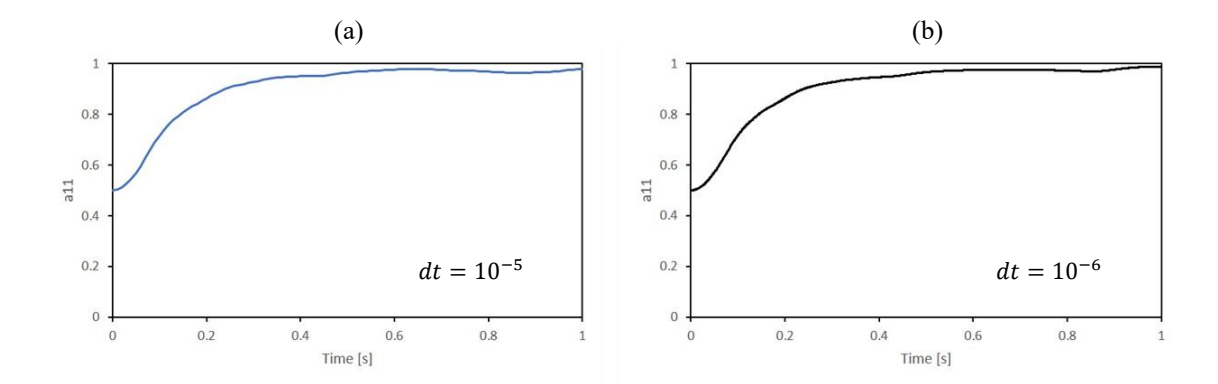
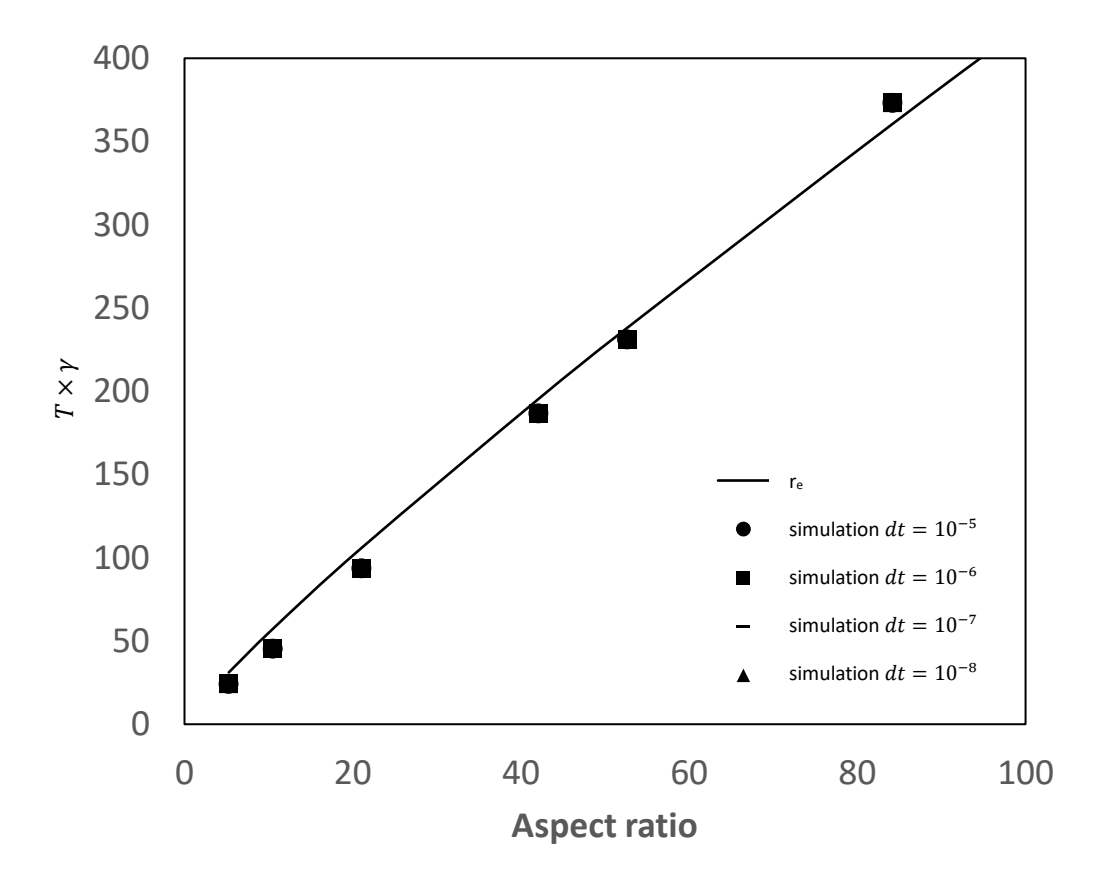


Figure 3.12 The orientation result in  $a_{11}$  direction with auto dt adjusted depends on the segment displacement for the simulation: (a) set input dt:  $dt = 10^{-5}$ , (b) set input  $dt = 10^{-6}$ .

# Evaluation of the update

A test was conducted to assess the effectiveness of the program maintenance and the update by comparing fiber rotation against the Jeffery model [52]. This comparison encompassed a range from short to long fibers in terms of fiber aspect ratio. As shown below, the model aligns with the Jeffery model after the program update. This alignment is even better than the previous model.



**Figure 3.13** The comparison between the simulation result from the updated algorithm of mechanistic model and the Jeffery rotation model with fiber aspect ratio below 100.

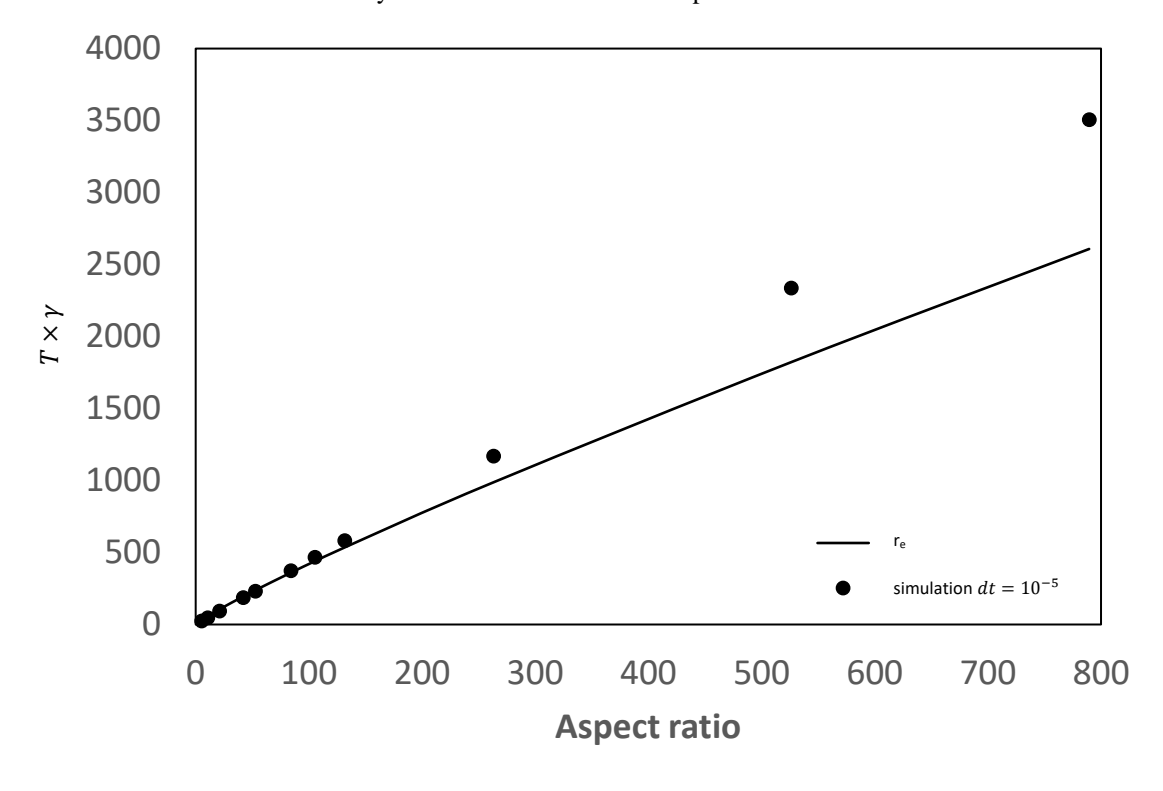


**Figure 3.14** The comparison between the simulation result from the updated algorithm of mechanistic model and the Jeffery rotation model with fiber aspect ratio from 0 to 800.

### 3.3.2. The effect of shear stress

In the mechanistic model, providing accurate stresses within the system is crucial to ensure a faithful representation of fiber flow in a polymer melt. Consequently, determining the appropriate shear stress to be employed in the model is vital for direct fiber simulation. As the shear cell in the mechanistic model mimics the evolution of a bundle of fibers flowing within the polymer melt, the stress it experiences can vary depending on the fiber cell's location. To guide researchers in finding the stress value that can represent the flow field, a leading commercial software in simulating the injection molding process, Moldex3D, is utilized to find the exact stress profile at each location of the flow field.

The following example illustrates the shear stress profile of an injection molded plaque over three different locations on the part. The simulation result is compared to the fiber length measurement done by Goris [2].

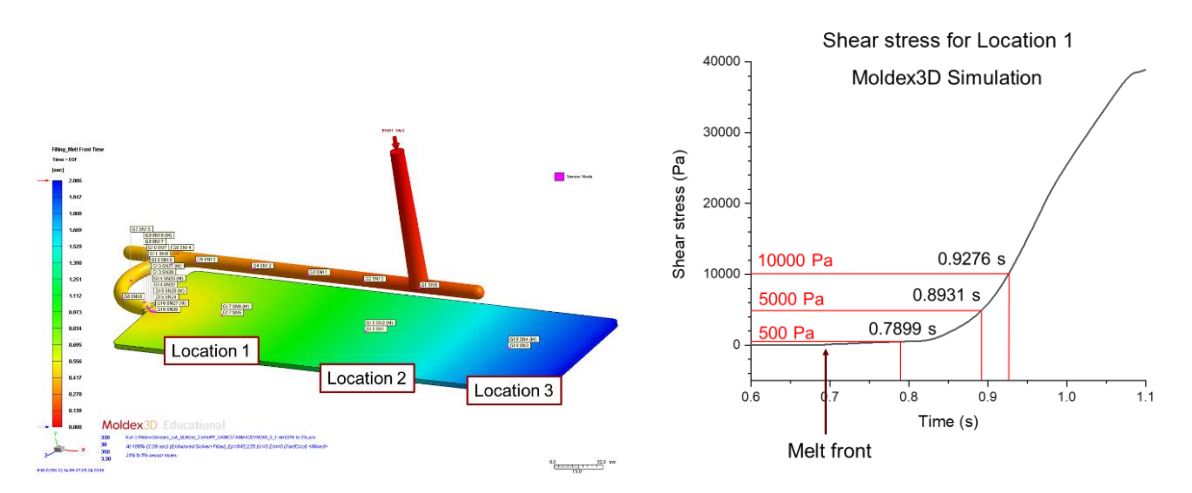


**Figure 3.15** The test location on an injection molded plaque with PPGF05 and the corresponding shear stress profile during the simulation using Moldex3D.

Here, an assumption is made that the longest fibers (15 mm) are nearing the point of breaking upon reaching Location 1. Consequently, the maximum fiber length within the cluster is adjusted to 7.5 mm. The segment length is refined to 0.1 mm to maintain a fiber aspect ratio of 5.26 for the flexible rotation. The simulation is initialized using the shear rate and viscosity at Location 1. As the melt front traveled to location 1, the shear stress begins to accumulate in that specific area. A range of shear stress values was selected based on the result in Figure 3.15 to see how the magnitude of shear stress will affect the fiber breakage. In cases where the shear stress is exceedingly

low, the forces within the shear cell prove inadequate to facilitate the division of fibers into segments, as depicted in Figure 3.16. Notably, no significant fiber damage is observed at stress levels of 1000 and 2500 Pa. A minimum stress of 3400 Pa within the system is required to initiate fiber breakage during the simulation.

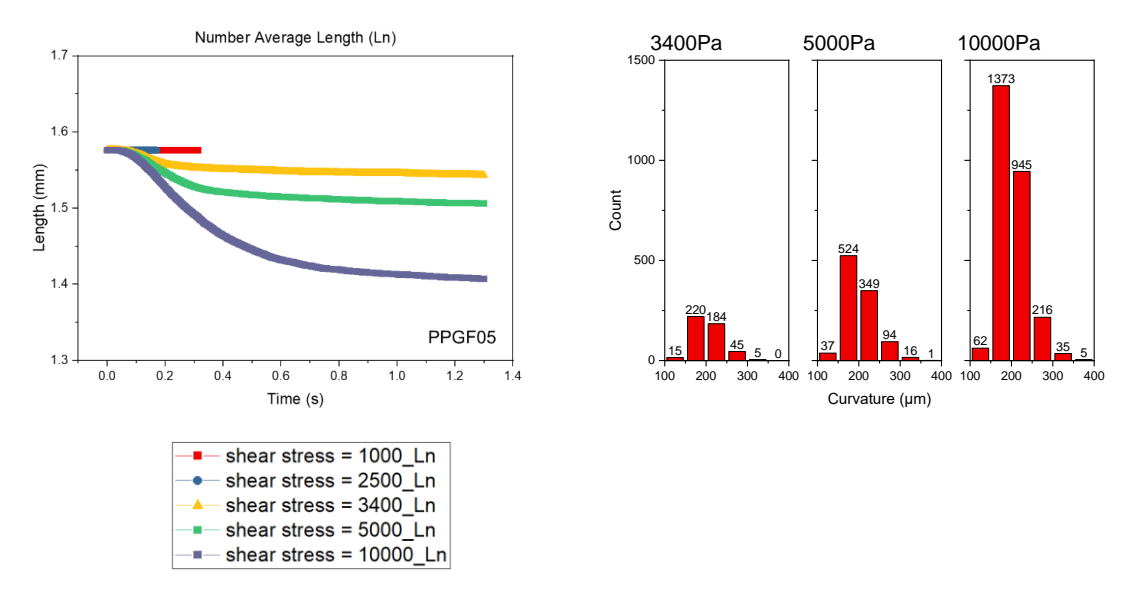


**Figure 3.16** The fiber attrition with various shear stress in the mechanistic model and the corresponding breakage distribution in the simulation.

By selecting the appropriate shear stress values from the flow field, the mechanistic model demonstrates high accuracy in predicting fiber attrition. Figure 3.17 demonstrates that the selected shear stress, obtained at 0.15 seconds after the melt front had reached location 1, yields the most optimal performance in predicting fiber attrition.

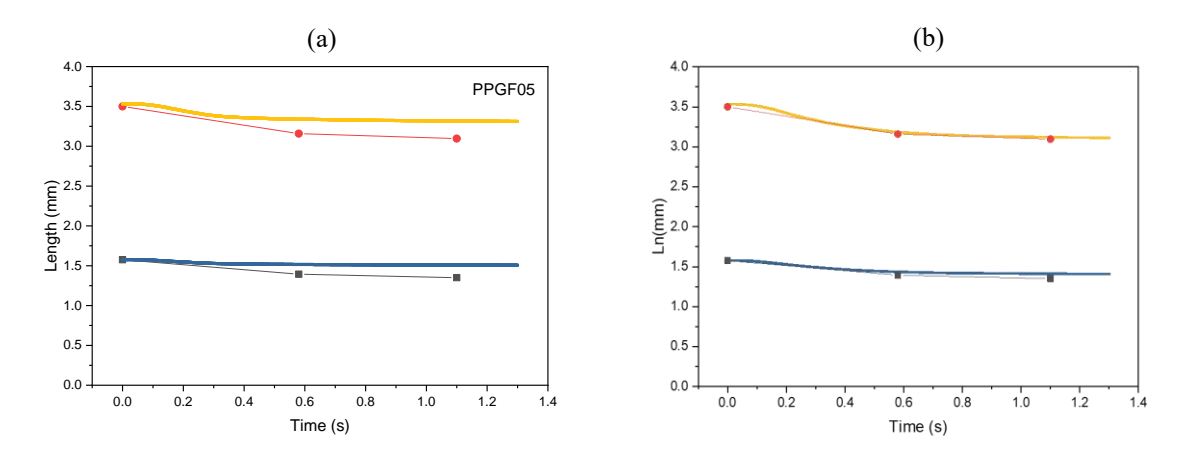
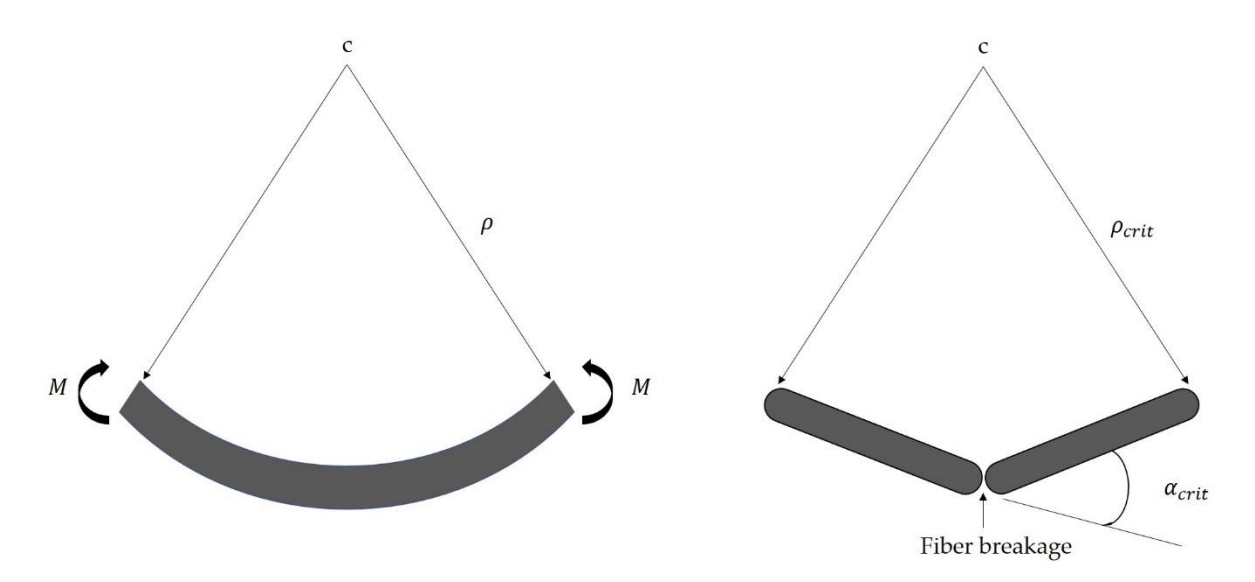


Figure 3.17 The Predicted  $L_W$  and  $L_N$  of simple shear flow simulation at varying shear stress with PPGF05: (a) Shear stress = 5000 Pa, (b) Shear stress = 10000 Pa.

# 3.3.3. Influence of Probability Theory on Fiber Damage

In the mechanistic model, the bending of a fiber is the only mechanism attributed to fiber deformation. Elongation and shear-deformation due to tensile, compression and shear loads are neglected. Thus, the bending behavior is implemented with the elastic beam theory [53]. In the model, the forces experienced by the fibers within the polymer matrix, which lead to bending and breaking, are approximated within the linear segments interconnected with flexible joints. To determine the breaking point, the local degree of bending is characterized by the radius of curvature at the connection points of two rods as shown in Figure 3.18. Furthermore, the critical curvature is used as an input parameter for the model to initiate fiber breakage. Once a fiber's segment curvature is below the assigned input parameter, the fiber will break at the joint of two connecting rods.



**Figure 3.18** Fiber deformation and approximation with bending theory: (a) Beam deformation with pure bending; (b) Approximation with rods and the expression of critical curvature during fiber breakage.

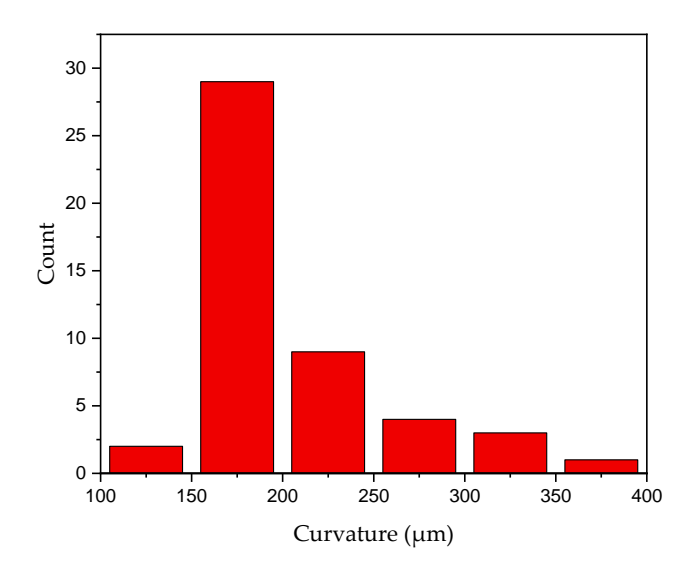


Figure 3.19 Breakage Distribution of the loop test using glass fibers.

To describe the fiber behavior during breakage under realistic conditions, a bending method was presented by Sinclair [54] using glass fibers. The tensile strength and Young's modulus were measured by twisting a loop in a fiber and pulling the ends until the loop breaks. A total of 48 experiments were performed and the non-Gaussian distribution resulted in an average value of 204.6 µm for the critical radius of curvature [55]. The values varied from 119 to 371 µm as seen in Figure 3.19. Based on these results, the mechanistic model was implemented to examine the effect of the excluded volume force constant. To validate the model, the result was compared with the Couette flow experiments using glass fiber-reinforced polypropylene (PP). The material used in this work was SABIC® STAMAX of Saudi Basic Industries Corporation (SABIC), Riyadh, Saudi Arabia, a reinforced polypropylene material. To set up a simulation, 1000 fibers with equal length of 2.5 mm were placed in a shear cell in Figure 3.20. The segment length in each fiber is a fixed value of 0.1mm with aspect ratio of 5.26 to ensure flexible rotation in the flow field [42]. In addition, Lee-Edwards periodic boundaries [56] were applied to all the cell walls to represent periodic conditions during the simulation as shown in Figure 3.20. A simple shear field with a shear rate of 16.65 s<sup>-1</sup> [21] in x-y plane was applied to the polymer matrix which corresponds to the hydrodynamic forces discussed previously. Table 3 shows the physical properties of fibers and the matrix.

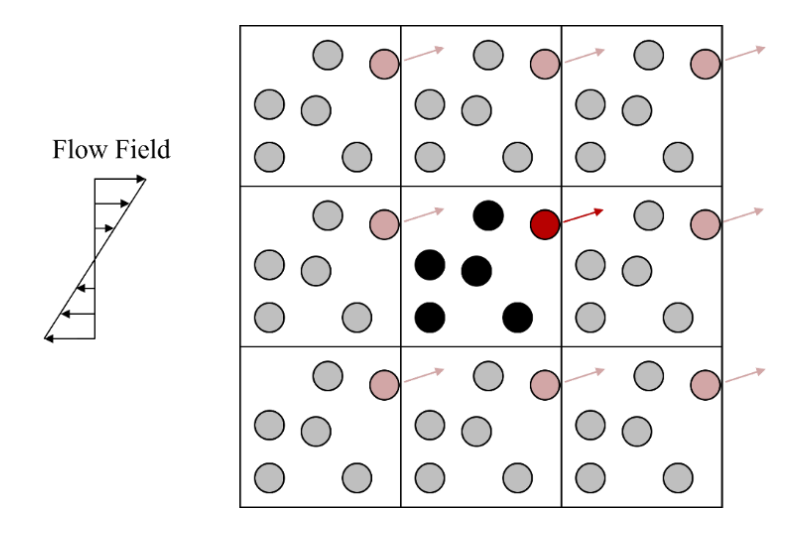
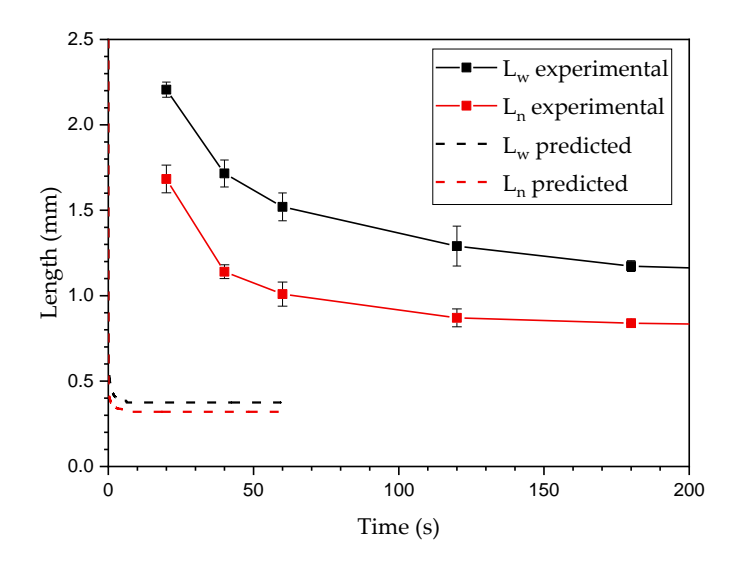


Figure 3.20 Shear cell with periodic boundary conditions.

**Table 3** Constant values of shear cell properties in simulation.

Parameter	Value
Viscosity (Matrix) [Pa-s]	200
Shear Rate [s <sup>-1</sup> ]	16.65
Fiber Young's Modulus [GPa]	73
Fiber diameter [µm]	19
Fiber Weight Fraction [%]	30
Time step [s]	$10^{-6}$ - $10^{-8}$

As stated in reference [13], the values of A and B in Equation (3.14) for the hydrodynamic effect remain unknown and must be adjusted for different processing condition. Values A and B have been chosen empirically, which are usually set in such a way that no fiber intersections are perceived, nor high repulsive forces are created. As suggested by [13], B was chosen to be 2 and A was tuned for each system with the relationship of shear rate  $\times$  viscosity/2 for the mechanistic model simulation which is 16.65 in this case. Figure 3.21 shows the number-average length ( $L_N$ ) and the weight-average length ( $L_W$ ) for the simulation. It is clear that when using the empirical method, breakage occurs too fast when is compared to experimental data. This shows that the traditional algorithm used for the simulation, where A = 1665, results in much higher excluded forces than the actual values. This causes fibers to break as they move closer to each other within the cluster. Thus, finding a proper repeatable method to determine the value for simulating fiber breakage is necessary and critical.



**Figure 3.21** Length evolution result by mechanistic model using an empirical excluded volume force constant compared to Couette flow experimental.

To further validate the model, the critical fiber breaking curvature and excluded volume force constant *A* were tuned to examine the variation of fiber length reduction. Table 4 shows the variables used in the simulation.

Table 4 Values varied in simulation.

Parameter	Value
Fiber Critical Curvature [µm]	200, 250, and 300
Excluded Volume Force Constant [-]	250, 500, and 750

Figure 3.22 shows the 5 second time evolution of L<sub>N</sub> at varying pre-demand breaking curvature from 200 μm, 250 μm, and 300 μm while keeping the same excluded volume force constant. As fibers start to bend, they reach a more significant critical curvature and result in a faster rate of breakage. As the force constant increases, the fiber experiences higher repulsive force as it approaches surrounding fibers. As two fibers approach each other, force increases until it reaches the maximum excluded volume force which is determined by the value of constant *A* in Equation (3.14). Thus, the influence of excluded volume force on fiber length reduction become more significant with higher critical breaking curvature. This trend can be seen in Figure 3.23 which varies the excluded volume force constant from 250 to 750 while keeping the same breaking curvature.

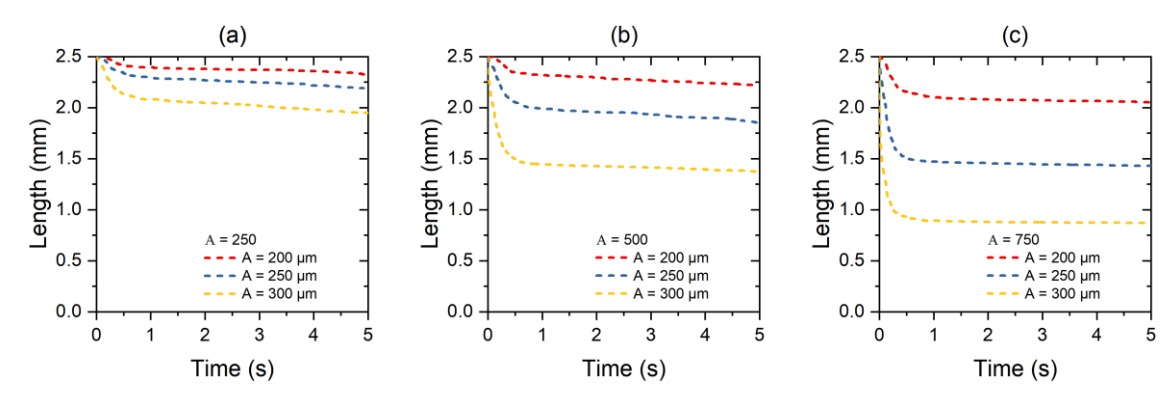


**Figure 3.22** Predicted  $L_N$  of simple shear flow simulation at varying fiber critical breaking curvature with three excluded volume force constants A from: (a) 250, (b) 500, (c) 750.

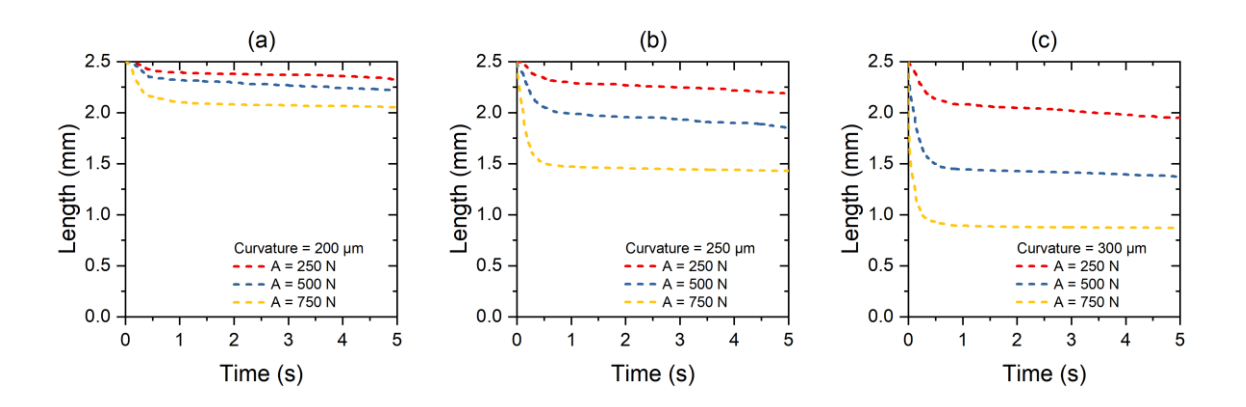
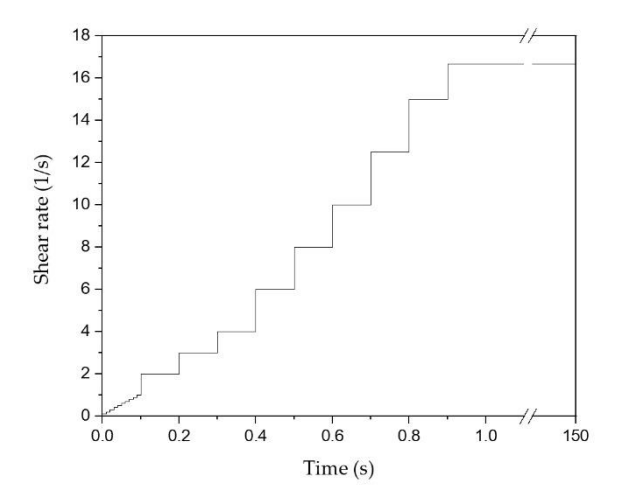


Figure 3.23 Predicted  $L_N$  of simple shear flow simulation at varying excluded volume force constant A with three critical curvature from: (a) 200  $\mu$ m, (b) 250  $\mu$ m, (c) 300  $\mu$ m.

# Fiber Relaxation

As discussed above, fibers were experiencing a higher breaking rate than experimental results. In order to place thousands of fibers within a small cell, fibers are forced into position with a critical angle which leads to entanglement and bending of the fibers within the cluster. This entanglement was a big issue during breakage prediction, and can cause overestimation of breakage during the early stage of the simulation. To achieve relaxation of the entanglements, the shear rate was not stepped up instantaneously, but instead, increased stepwise from 0 to 16.65 s<sup>-1</sup> within the first second of simulation time. This allows the relaxation of the bent fibers inside the cluster. The simulation shear rate remained at 16.65 s<sup>-1</sup> for the remaining 149 seconds (Figure 3.24). This technique allowed fibers to straighten out and thus reduce the number of critical angles between connecting joints, without leading to excessive and unrealistic fiber attrition at the beginning of the simulation.



**Figure 3.24** Stepwise increase profile in shear rate for fiber relaxation.

A relaxation test was done by tuning critical curvature from 200  $\mu$ m to 300  $\mu$ m while keeping the force constant A equal 500. Figure 3.25 presents the  $L_N$  evolution with the relaxation applied. Relaxation in the first second of the simulation significantly reduced the initial fiber breakage caused by entanglement during cluster generation. After the first second, the interaction with neighboring fibers caused by the flow field leads to decreases in fiber curvature which leading to breakage when the assigned critical curvature is reached.

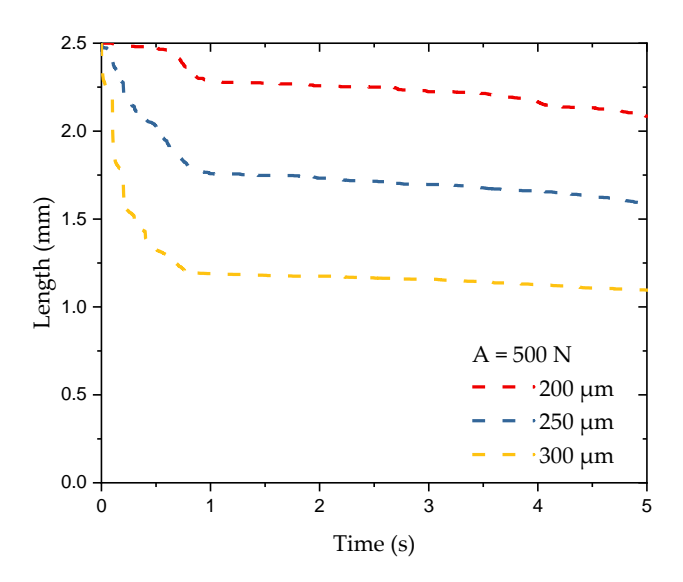
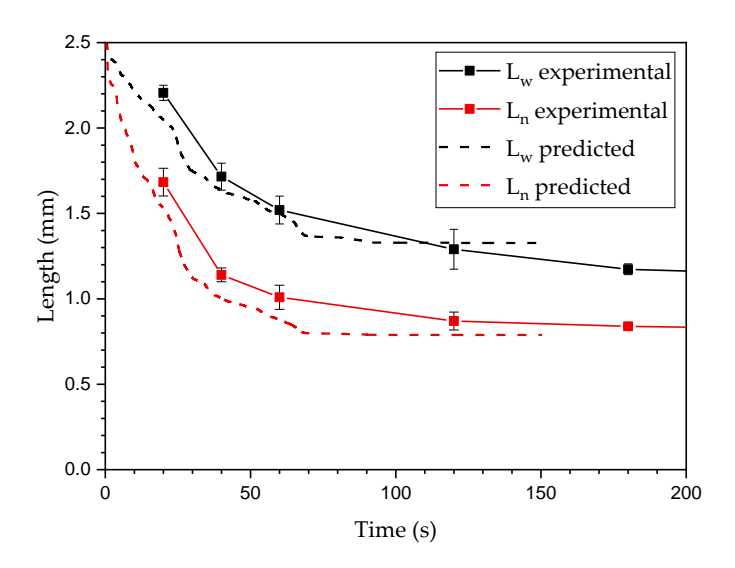


Figure 3.25 Predicted  $L_N$  of simple shear flow simulation at varying fiber critical breaking curvature with fiber relaxation applied to the first second in the simulation.

Figure 3.26 presents a comparison between the Couette experiment and the simulation for a critical curvature of 300  $\mu$ m and an excluded volume constant A of 500, with a shear rate increase from 0 to 16.65 s<sup>-1</sup> within the first second and remaining at 16.65 throughout the rest of the simulation. As seen in Figure 3.26, the initial breakage caused by an unsteady system is reduced significantly. The simulation matches the experimental results much better. However, there is a slightly faster reduction rate for both  $L_N$  and  $L_W$ , as well as a higher final unbreakable length.



**Figure 3.26** Fiber length evolution compared to the Couette flow experiment with fiber relaxation applied to the first second in simulation.

The fiber attrition model's final part introduces the fiber probability measurements. Figure 3.27 presents the breakage criteria with (b) and without (a) an experimental probability of failure distribution. This portion of the work introduces a probability function into the breakage simulation, as was similarly done by Çelik [55], which determines a range at which fibers may break. Fibers begin to have the probability of breaking when their curvature is smaller than the maximum curvature and will break when curvature reaches the minimum curvature (Figure 3.27b). Comparing to the fixed curvature, probability theory provides powerful tools to explain the breakage behavior as seen below, where m is chosen as 15 for this research (Figure 3.29),

$$x = \frac{\max curvature - curvature}{\max curvature - \min curvature}$$
(3.32)

Probability = 
$$\frac{\exp(m * x) - 1}{\exp(m) - 1}$$
 (3.33)

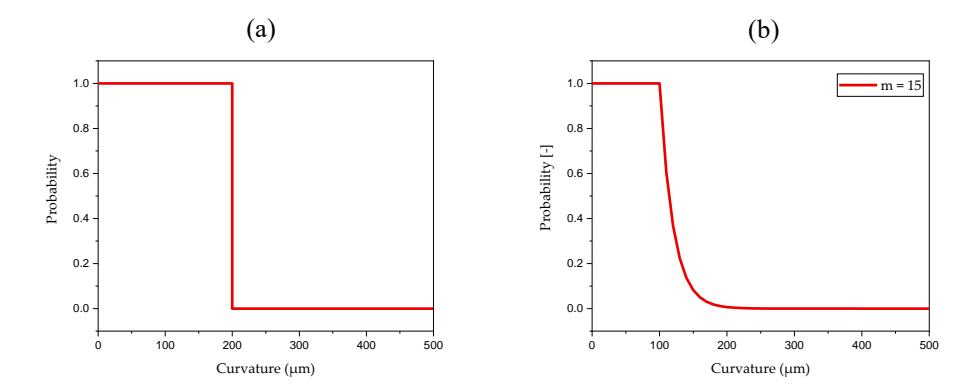
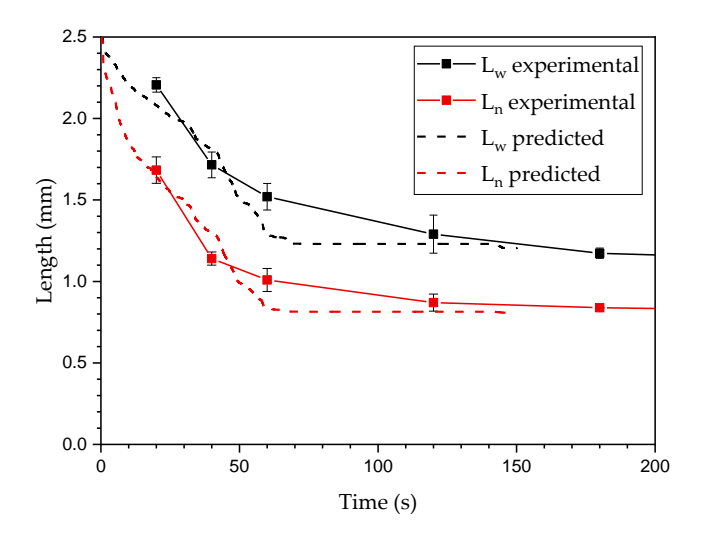


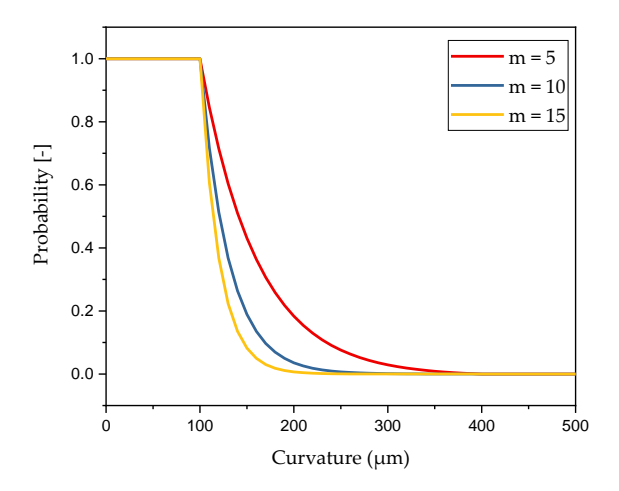
Figure 3.27 Different breakage models implemented in the mechanistic model: (a) Original breakage model; (b) probability breakage model when m = 15.

In Figure 3.28, the model showed a lower initial breakage rate and achieved nearly the experimental steady-state fiber length. Unlike the fixed critical breaking curvature, the relaxation allowed fibers to relieve the entanglement and achieve a steady state in the system, slowing down the breakage rate. As long fibers break into shorter fibers, the chance for fibers to contact each other is reduced, resulting in a higher alignment of fibers in the flow direction. Thus, fibers would gradually align in the flow direction, where the rate of breakage significantly reduces after about 60 seconds. However, in shear flow conditions influenced by Jeffrey orbits, if allowed sufficient time, the fibers eventually rotate and break, which can observe around the 150 second mark.

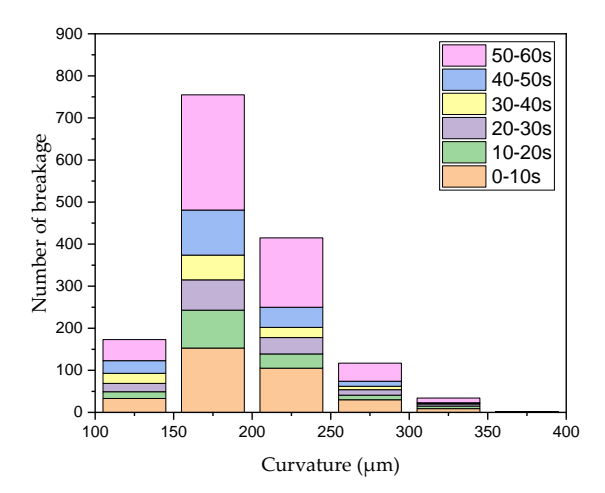


**Figure 3.28** Fiber length evolution compared to the Couette flow experiment with fiber relaxation and probability breakage applied to the first second in simulation.

The curvature at the break point for Figure 3.28 was recorded throughout the simulation and shown in Figure 3.30. Here, only the first 60 seconds are represented in the distribution, as the fiber length in the simulation remained relatively constant after this period. Compared to Figure 3.19 which shows the loop experimental result from [55], the predicted distribution showed a similar trend to the experimental data. There was a higher deviation in the range of 200 to 250  $\mu$ m and 350 to 400  $\mu$ m. This may be due to the value of m in Equation (3.33) selected for this research was too high for the system. Lowering the value of m will shift the curve to the right (Figure 3.29) which increases the probability for fibers to break at a larger curvature.



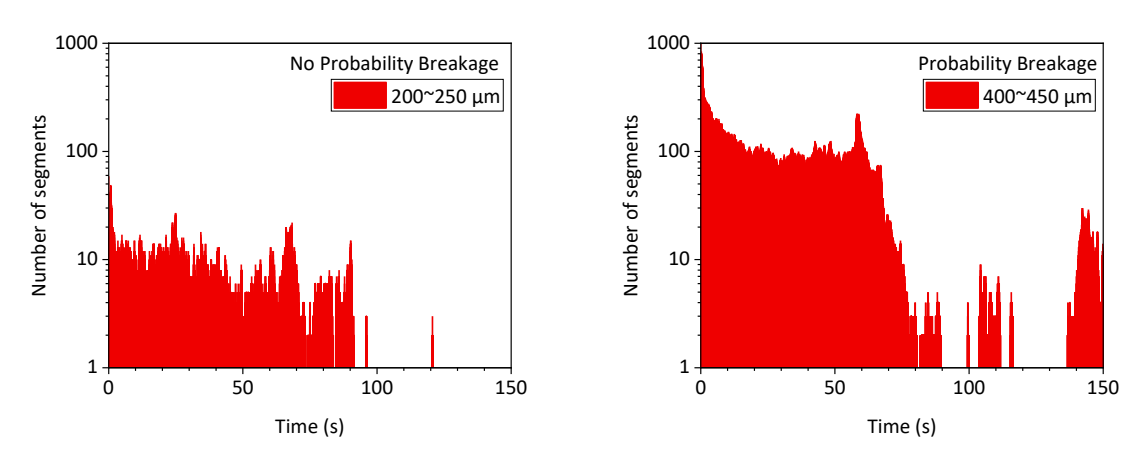
**Figure 3.29** Varying values of *m* for the probability breakage applied in the model.



**Figure 3.30** Breakage Distribution over time of simulation results with fiber relaxation and probability breakage model applied.

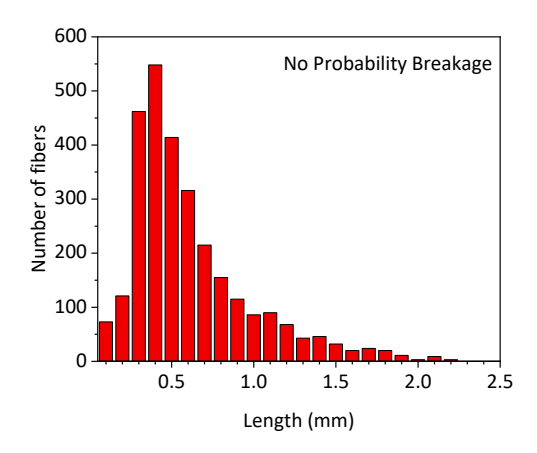
#### Segment's Curvature Distribution

The number of segments' curvature within 50 µm of the critical breaking point is recorded in Figure 3.31. The decreasing trend after 60 seconds for both No PB and PB indicates that the chance of breakage is reduced, which fits the result. Additionally, the increasing trend near 150 seconds for PB symbolizes the chance for fibers to break rising, which can be seen around 150 seconds in Figure 3.28.



**Figure 3.31** The distribution of which the segment's curvature is within 50  $\mu$ m of the critical breaking point: 200~250  $\mu$ m for No PB (Left); 400~450  $\mu$ m for PB (Right) in simulation.

The number of the longest fiber 2.5 mm is not included in the Figure 3.32. No PB shows a larger amount of shorter fibers in the system while PB has longer fibers in the system, and the length distribution shifts to the right.



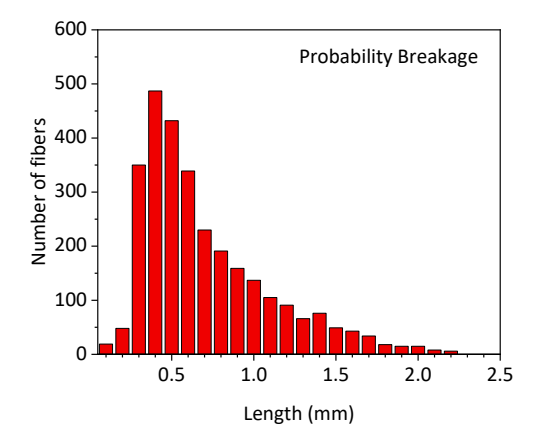


Figure 3.32 Fiber Length Distribution at the end of 150 second simulation.

# 3.3.4. Parallelization of the code

One of the factors preventing the mechanistic model being widely used in predicting fiber attrition is its extensive computational time, primarily attributed to the substantial dataset underpinning each case. Currently, researchers are constrained to employing a maximum of 500 fibers in simulations to approximate the comprehensive process landscape. However, industrial applications entail a minimum of several thousands of fibers. Furthermore, each fiber is represented as a chain of rods to emulate rotational behavior within polymer flow, introducing additional computational overhead for every time step. To enhance the accessibility of direct fiber simulation for broader applications, mitigating the computational time expenditure becomes imperative. Thus, speeding up the code has become crucial in this application. Two primary parallelization processes are widely employed today: MPI and OpenMP programs, which differ in their utilization of memory during computation.

The OpenMP program provides a standardized API for defining multi-threaded shared-memory programs. This program generates threads within parallel regions, utilizing multiple threads to enhance processing speed [57]. Communication among threads occurs through shared variables. However, it operates within a shared memory system, which constrains the number of processors within the system. The shared-memory system stores information within the same processor, limiting speed according to the number of processors within the system.

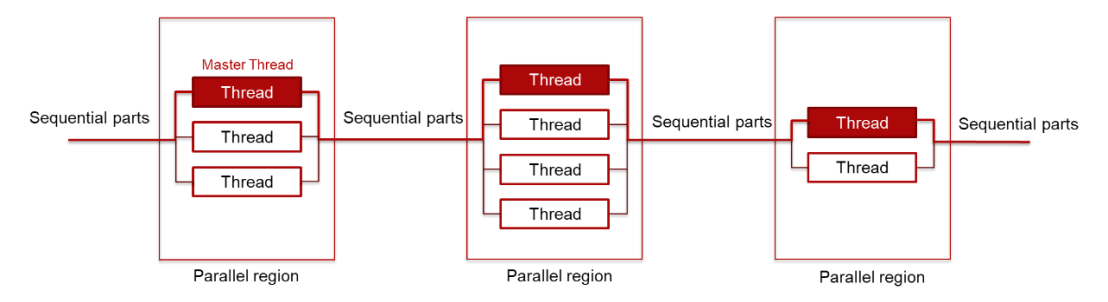


Figure 3.33 Computational structure of OpenMP program.

In contrast, the MPI program employs a Distributed Memory System characterized by high communication efficiency and practical parallel computation across processors [58]. This setup stores information separately, and messages are transmitted through an interconnect network. A greater number of processors corresponds to higher processing speeds.

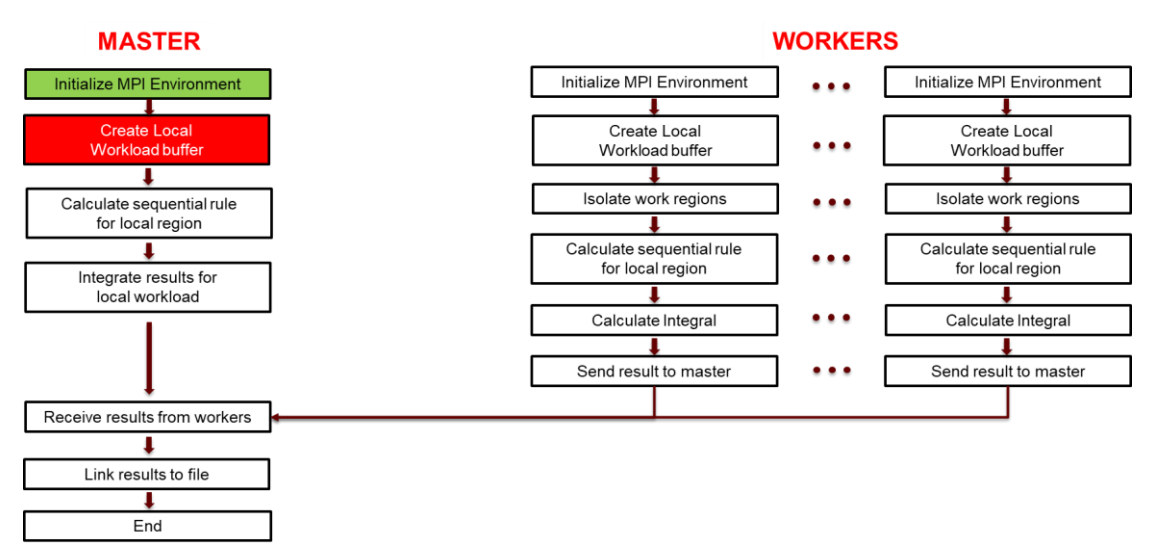


Figure 3.34 Computational structure of MPI Program.

By comparison, when a program requires multi-threading, opting for OpenMP is advisable. Conversely, employing an MPI program is more suitable if the code involves a substantial volume of message passing. Initially, dividing messages for message passing might pose challenges, but subsequent efforts are comparatively less demanding.

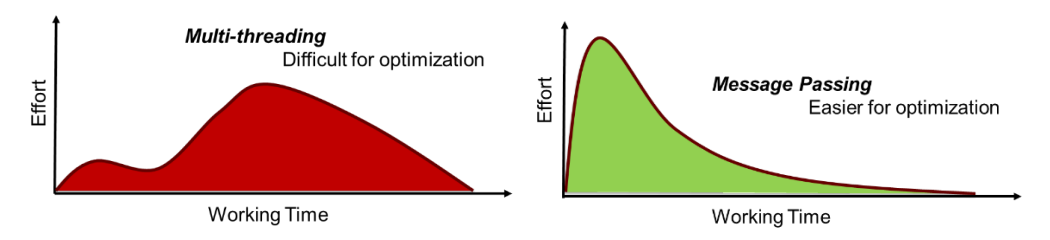


Figure 3.35 The working comparison between multi-threading and message passing in the algorithm [59].

### Assessing the Potential for Code Parallelization

In order to assess the feasibility of parallelizing the algorithm, it is crucial to comprehend the time allocation for each function within the model. This evaluation involves computing the time taken by each function during a single time step. Table 5 shows that the primary computational load for a single time step is distributed across two key sections: 78% of the time is dedicated to calculating the excluded volume force between fibers and walls, while 14.4% is allocated to calculating fiber motion.

**Table 5** The break-down of the time cost for each function in the algorithm.

Function	Computational Time for One Time Step	
Fiber Hinge Calculation	3.24 s	
Ghost Segments	14.01 s	
Excluded Volume Force	55.47 s	
Bending and Torque	3.02 s	
Fiber Motion	81.65 s	
Others	25.47 s	
Total Time	182.85 s	

The current algorithm assumes that each individual fiber is treated as a separate object, updated only in relation to the current status of other fibers. This characteristic renders the current code highly amenable to parallelization, as the computation for each fiber remains independent. Therefore, the parallelization process will primarily concentrate on the excluded volume force calculation and fiber motion. In summary, the MPI program was chosen as it is designed to accelerate communication processes, where interactions occur through data exchange and

synchronization across various cores via message passing. A process can belong to multiple communicators, with additional communicators co-existing.

#### Two Cores

The parallelization was first conducted by utilizing two cores: one acts as the main core (id = 0) to process and dispatch fiber information requiring computation during each time step to another core, while the primary calculations are performed in the second core (id = 1), as illustrated in Figure 3.36. All fibers' information is transmitted to core id = 1 at each time step. Once the calculation of fiber motion for the new time step is complete, the final information is sent back to the main core (id = 0).

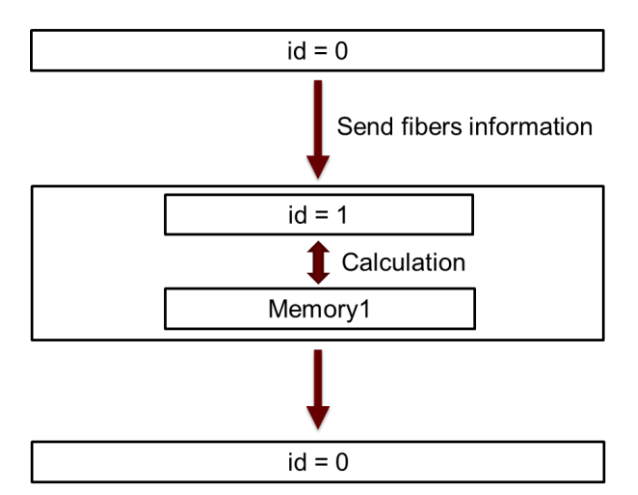


Figure 3.36 The flow chart of communicating process in algorithm with two cores utilized in computation.

# Multiple Cores

Once the two cores had been set up and tested to work for the MPI environment, the parallelization was further expended to allow assigning multiple cores for the computation work. The second method employed for parallelization involves leveraging multiple cores during function calculations. Each core now retains its own set of information. Upon completing the computation, the core returns the information to the main core identified as id = 0.

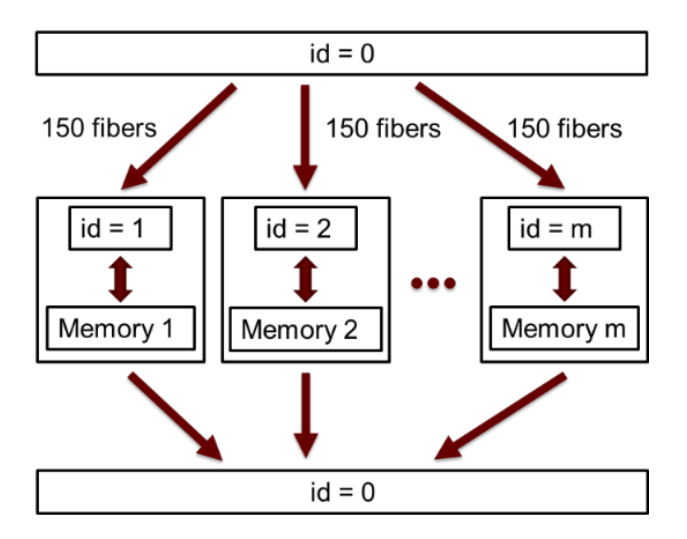


Figure 3.37 The flow chart of communicating process in algorithm with multiple cores utilized in computation.

With the multiple-core computation environment introduced in the algorithm, the program can be further sped up in comparison to using only two cores in the computer.

#### Amdahl's law

Amdahl's Law is a principle in computer architecture and parallel computing that quantifies the potential speedup of a program when some parts of it are made parallel while other parts remain serial (single-threaded) [60, 61]. It was formulated by Gene Amdahl in 1967 [62]. The law provides a way to estimate the maximum achievable speedup of a task given a certain amount of parallelization. The formula for Amdahl's Law is as follow:

Speedup = 
$$\frac{1}{[(1-P)+(P/N)]}$$
 (3.34)

Where Speedup is the theoretical improvement limitation in performance achieved by parallelizing a program, P is the fraction of the program that can be parallelized, and N is the number of processing units used for parallel execution.

The key insight from Amdahl's Law is that the potential speedup is limited by the portion of the program that cannot be parallelized. As the number of processing units (N) increases, the impact of the non-parallelizable portion (1 - P) becomes more significant, eventually limiting the overall speedup [63, 64]. This law emphasizes that improving a program's performance through parallelization requires a focus on both the parallelizable fraction

of the code and the overhead introduced by synchronization and communication between parallel tasks. There is a limitation on how fast the code can be accelerated. Although it underestimates the importance of balancing efforts between improving the parallelizable portions of the code and the non-parallelizable portions, it is often used nowadays to provide an initial assessment of the realistic performance of parallelization.

A test sample for evaluating the performance of the parallelization program is presented in Table 6. A total of 1000 fibers with a starting length of 2.5 mm is used to test the performance of the parallelization with different cores used during the computation.

**Table 6** Test environment for evaluating the performance of the parallelization for the algorithm.

	Values	
Fiber length	2.5 mm	
Fiber number	1000	
Segment per fiber	25	
Cell size	1.5mm * 1.5mm * 1.5mm	
Shear rate	$16.65 \text{ s}^{-1}$	
dt	10-6	

The time required for two functions, fiber motion, and exclude volume force, was extracted, and compared in Table 7 and Table 8. For shorter durations in the simulation, the speedup ratio isn't notably significant. Nevertheless, with more time steps being calculated in the simulation, more fiber breakage happened within the flow field. This resulted in more segment information that needed to be computed at each time step. Here, parallelization demonstrates its efficacy when dealing with greater amounts of data that necessitate processing at each time step, consequently reducing the computational time.

Table 7 The computational time required for calculating fiber motion in the algorithm.

	150 Time Steps	1,500 Time Steps	15,000 Time Steps
Non-Parallelization (2018)	40.31 s	386.36 s	4760.85 s
MPI (2 cores)	39.54 s	283.27 s	2074.23 s
MPI (3 cores)	20.44 s	143.34 s	1113.24 s

MPI (4 cores)	14.23 s	97.63 s	747.23 s

**Table 8** The computational time required for calculating excluded volume force in the algorithm.

	150 Time Steps	1,500 Time Steps	15,000 Time Steps
Non-Parallelization (2018)	32.81 s	313.58 s	3705.95 s
MPI (2 cores)	24.86 s	150.73 s	1384.45 s
MPI (3 cores)	17.39 s	105.97 s	1012.27 s
MPI (4 cores)	14.86 s	93.52 s	825.82 s

Table 9 presents the computation time comparison between different versions throughout the updates made in this research. With the maintenance of the code and the update of the algorithm structure, there has already been a significant improvement in computing efficiency. Furthermore, with the additional parallelization, which utilizes multiple cores for computation, the mechanistic model has shown even greater improvement.

**Table 9** Total computational time required for 15,000-time steps for different version of the algorithm.

	Non-	Non-			
	Parallelization	Parallelization	MPI (2 cores)	MPI (3 cores)	MPI (4 cores)
	(2018)	(2019)			
Time cost	10138.38 s	4682.64 s	4150.99 s	2876.50 s	2273.72 s

In summary, the MPI program is specialized in communication processes, where a process interaction includes data exchange and synchronization among different cores through message passing. Additionally, a code redesign enabling parallel processing has significantly reduced analysis times, depending on the number of cores used in computing, while enhancing user-friendliness.

# 4. Modified fiber breakage model

#### 4.1. Introduction

Until now, major orientation models, including Folgar-Tucker model [65], ARD-RSC Model [66] and iARD-RPR Model [36, 67] were based on the concept of Jeffery's single-fiber equation [52], but by expanding from a single fiber to multiple fibers in the fluid, several mechanisms affect the motion of fibers. As fiber length is crucial in improving the mechanical performance of a molded product, an increase in fiber length correlates with the increased strength of the product. Bechara et al [23] proposed a modified breakage model by using the unbreakable length of fibers in the process instead of probability function. Researchers also determined that parts are stronger in the direction of fiber alignment if both fiber length and volume fraction are increased [7]. However, fibers in the polymer melt often break during polymer processing due to the intense viscous forces during flow and deformation. While short fibers are easier to align to flow direction than long fibers, long fibers experience a higher breakage rate with higher shear rate. There is little research that relates the fiber orientation with fiber attrition during processing; therefore, it is essential to understand how flow-fiber coupling affects the fiber orientation during the process, thus impacting the fiber breakage prediction. This study discusses the correlation between fiber orientation and fiber breakage using the modified breakage model with CAE simulation. In addition, the modified breakage model is also validated to search for satisfactory model parameters with injection molding process.

To estimate the mechanical behavior of a product, it is necessary to predict the process-induced fiber breakage. In 1959, Forgacs et al. [19] proposed that the Young's modulus and the fibers' geometrical properties describe the critical shear stress that provokes fiber buckling. It is evident from this that fibers tend to break under light loads when the aspect ratio is high. Hinch [20] later calculated the deformation of an ideal elastic particle in a shear flow using the Slender Body theory. To determine the repeatable length degradation of glass fibers at various fiber concentrations, initial fiber lengths, residence times, melt temperatures, and processing speeds, Goris et al. [21] developed an experimental setup using a Couette rheometer in conjunction with the fiber length measurement.

This setup provides good insight into measuring the fiber length. However, no simulation tool accurately predicts the final fiber length in a molded part, as the phenomenon of fiber breakage is not fully understood. Thus, the numerical simulation is applied to investigate the phenomena of fiber breakage.

Some continuum models, which are very different from particle-level simulations, have been developed to obtain the macroscopic picture of breakage by solving the balance equation of fiber length distribution [4, 22]. Phelps et al. [4] presented a quantitative model to describe fiber attrition based on buckling as the driving mechanism for fiber breakage during processing. Phelp's model is based on three fitting parameters: the breakage coefficient (CB), the hydrodynamic drag coefficient ( $\zeta$ ) and the distribution shape factor (S). They defined the critical force needed to cause buckling ( $F_{crit}$ ) and the critical flow regimen ( $\dot{\gamma}_{crit}$ ) that cause buckling as a function of fiber characteristics and flow parameters:

$$F_{crit} = \frac{\pi^3 E_f D^4}{64 L_i^2} \tag{4.1}$$

$$\dot{\gamma}_{crit} = \frac{\pi^3 E_f D^4}{4\zeta \eta_m L_i^4} \tag{4.2}$$

where  $E_f$  is the Young's modulus, D is the fiber diameter,  $L_i$  is the fiber length,  $\eta_m$  is matrix viscosity, and  $\zeta$  is the drag coefficient. This model introduces a Normal or Weibull probability distribution that determines the location along the fiber's axis where failure is likely to occur. However, this approach does not consider the fiber breakage caused by fiber volume fraction, which ignores fiber-fiber interactions as a source of damage. A novel modified breakage model is then developed in Polymer Engineering Center by Bechara et al [23].

$$L_{\infty} = \lambda \left(\frac{\sigma_u \, d_f^2}{\eta_m \dot{\gamma}}\right)^{0.5} \tag{4.3}$$

The coefficient  $\lambda$  is a material-dependent property and a measure of fiber-fiber interactions that cause fiber attrition during processing. The parameter is assumed to capture the effects of fiber concentration (fiber-fiber interactions) and fiber-wall interactions.  $\lambda$  as a function of fiber content is obtained from the measured  $L_{W\infty}$  values of the Couette rheometer experiment [23]. The linear correlation between  $\dot{\gamma}$  and  $k_f$  leads to a straightforward expression for the breakage rate coefficient:

$$k_f = \xi \dot{\gamma} \tag{4.4}$$

where  $\xi$  is a scale factor for the rate of deformation. Reducing the number of fitting parameters introduced when developing a model is beneficial since this makes the approach more robust, and potentially reduces the number of experiments needed to determine such parameters [24].

To fully understand the micromechanical picture of fiber breakage, particle simulation is necessary to develop an understanding on the details of concentrated fiber suspension dynamics [25-29]. Until now, single particle models are not accurate enough or well developed to investigate the degradation mechanisms at fiber level due to expensive computation. Therefore, a particle level model developed at PEC at the University of Wisconsin-Madison will be extended to gain better understanding of fiber damage.

# 4.2. Modeling Approaches

The modified breakage model was validated using a research version of Moldex3D, a leading CAE software for the plastic injection molding industry, to find suitable parameters for the model. To implement a user-defined fiber breakage model, the Solver API for Fiber which supports Moldex3D Enhanced Flow Solver was used in this study. Additionally, the empirical model parameters from the Phelps model were used as an input for a Moldex3D simulation to compare with the modified breakage model. Below were the forms of equations implemented in the Solver API for the validation of modified breakage model:

$$\frac{DL}{Dt} = -k_f(L - L_{\infty}) = f(:)$$
(4.5)

$$L(t=0) = L_0 (4.6)$$

where L is the fiber length,  $L_0$  is the initial fiber length, f(:) is the user-defined source term, and  $\frac{DL}{Dt}$  is the material derivative.

Scale of deformation -  $\xi$ 

Given that  $\lambda$  was determined based on Couette flow experiments [23], the  $\xi$  value was iterated to identify the

optimal value during the simulation. To establish the suitable range for  $\xi$  within the model, the average simulated fiber length over the thickness direction at each measured location was compared to experimental values as shown in Figure 4.1.

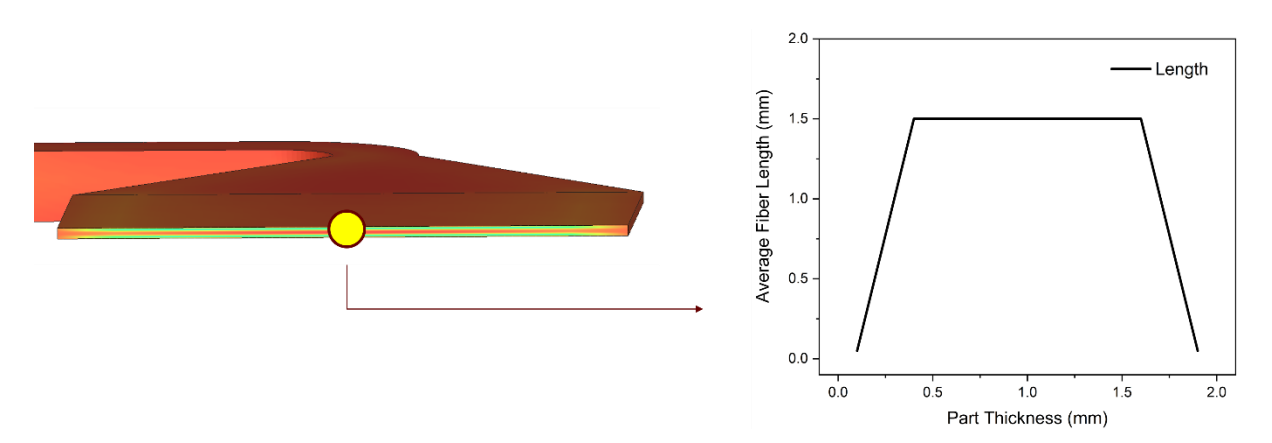


Figure 4.1 The procedure of extracting fiber length distribution data from simulation over the part thickness.

Based on the values extracted from the simulation, the difference between the simulated length and the measured value is presented as error percentage which is calculated as shown below in Equation (4.7).

$$error\% = \frac{|simulation - experiment|}{experiment} \times 100\%$$
 (4.7)

To evaluate the performance of the modified fiber breakage model regarding the prediction of length reduction throughout the manufacturing process, the error percentages at each measured location are averaged to provide an overall view of the simulation.

Ave error% = 
$$\frac{\sum_{i} \text{Loc. } i \%}{i}$$
 (4.8)

The iteration of  $\xi$  was halted when an inflection point in the average error percentage was observed in the simulation results as shown in Figure 4.2. Each data point on the graph corresponds to an individual simulation.

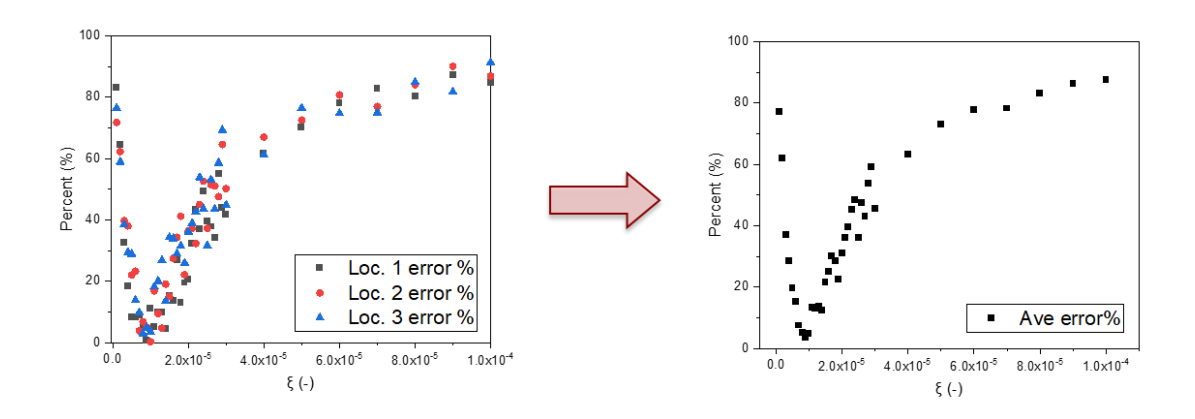


Figure 4.2 The procedure of calculating the average error percentage from a simulation result.

# 4.3. Effect on Fiber-Flow Coupling (Plaque)

As discussed in Chapter 4.2, the leading polymer processing simulation software, Moldex3D, was used to implement the modified breakage model as a user-defined fiber attrition prediction and validate its performance. To study the proposed model within the injection molding process, the software requires an input of initial fiber length. The software uses this input to initiate the computation of length deduction during the injection molding simulation. Consequently, an injection-molded plaque provided by SABIC was utilized to validate the model and to examine the influence of viscosity on the prediction using the modified breakage model at the same time. In addition, the flow-fiber coupling model introduced by Favaloro et al. [32] uses an effective scalar viscosity to approximate the complete anisotropic viscosity tensor, along with an effective matrix shearing strain rate. This flow-fiber coupling model offers a cost-effective approach for incorporating the coupling behavior into computational simulations and is applied to this study.

### Fiber Length Measurement

The fiber length measurement was conducted using a technique developed at the Polymer Engineering Center (PEC), which has been validated against standard commercial methods. This technique ensures reliable results by sampling between 10,000 to 100,000 fibers and extracting at least three samples for each test condition. Figure

4.3 illustrates the primary steps of the measurement process. The introduction of the down sampling step is driven by two reasons. First, even a small sample consists of millions of fibers, making it cumbersome and unnecessary to process images with such a large quantity of fibers. Using a smaller subset produces equivalent results [2]. Second, fibers at the sample's edges might have suffered damage during the extraction step and should therefore not be considered in the length distribution. The down sampling step selectively captures longer fibers, necessitating a correction to account for this bias [68].

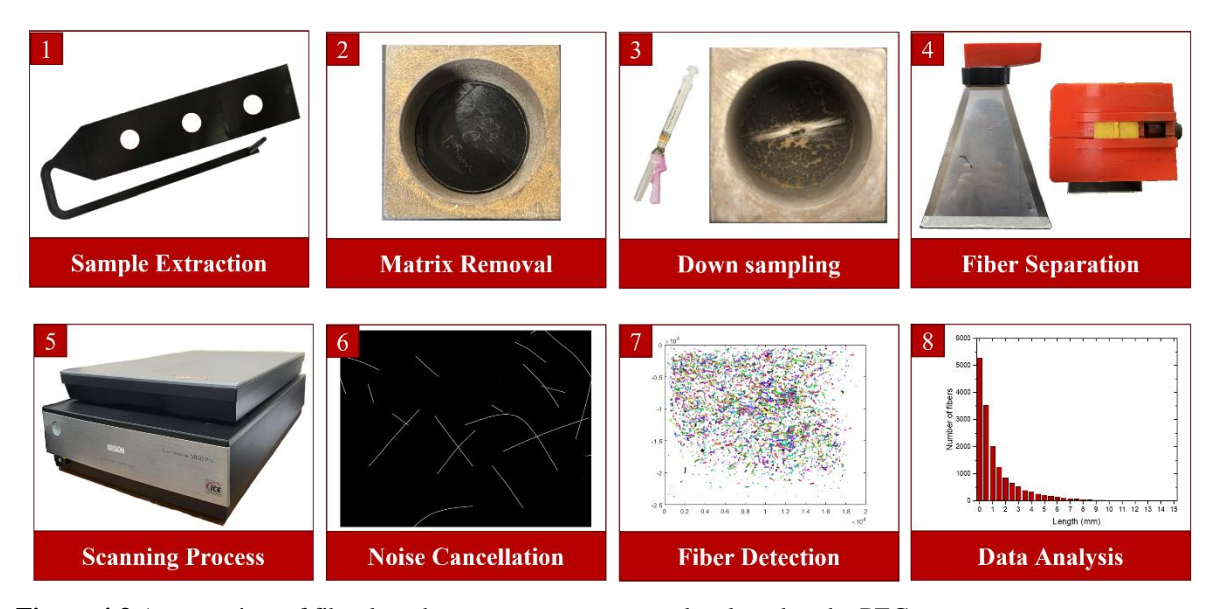
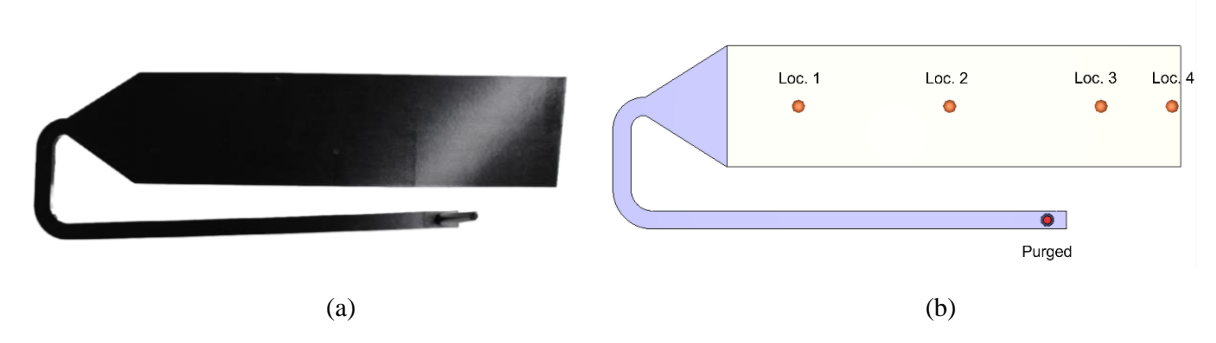


Figure 4.3 An overview of fiber length measurement process developed at the PEC.

In this study, fiber length measurements were performed on injection molded plaques provided by SABIC. These plaques had two different fiber contents: STAMAX 20YM240 (PPGF20) and STAMAX 30YM240 (PPGF30), and they had dimensions of  $102\times305\times1.5$  mm³ and  $102\times305\times2.0$  mm³, respectively. The geometry of the molded plaques and the specific extraction locations are depicted in Figure 4.4. An overview of the measurement conditions can be found in Table 10. To ensure accuracy and minimize human errors throughout the process, 6-8 samples were measured for each type of plaque, ensuring reliable results for subsequent validation. Specifically, Location 4, positioned 5 mm away from the end of the plaque, was selected to provide a comprehensive understanding of length degradation along the length of the plaques.



**Figure 4.4** The injection molded plaque for fiber length measurements, (a) the geometry of molded plaques, (b) the sample location extracted from the plaques.

**Table 10** An overview of fiber length measurement parameters.

	Thickness	Location	No. of Samples at Each Location
PPGF20	1.5 mm 2.0 mm	Purged, Loc.1,  Loc. 2, Loc. 3,	6-8
PPGF30	1.5 mm 2.0 mm	Loc. 4	<b>V</b> 0

The results obtained from the fiber length measurements are presented in Figure 4.5. The results show that fiber length exhibits significant variation within the purged material across all four conditions. While burning off the matrix for samples extracted from the purged location, certain fiber bundles persisted even after traveling through the barrel section of the injection molding machine. This persistence contributed to a substantial variance in the calculated  $L_W$ , as these longer fibers held greater weight in the calculation. As the polymer melt entered the mold cavity through the gate, the fibers experienced significant breakage, resulting in a relatively stable length compared to that of the purged location. A higher degree of fiber breakage was observed for PPGF30, owing to the larger number of fibers present, which consequently led to higher frequency in fiber-fiber interactions and subsequent breakage throughout the process. Moreover, the average fiber length for injection molded plaques did not follow the general decreasing trend; instead, it exhibited a slight increase toward the end of the part.

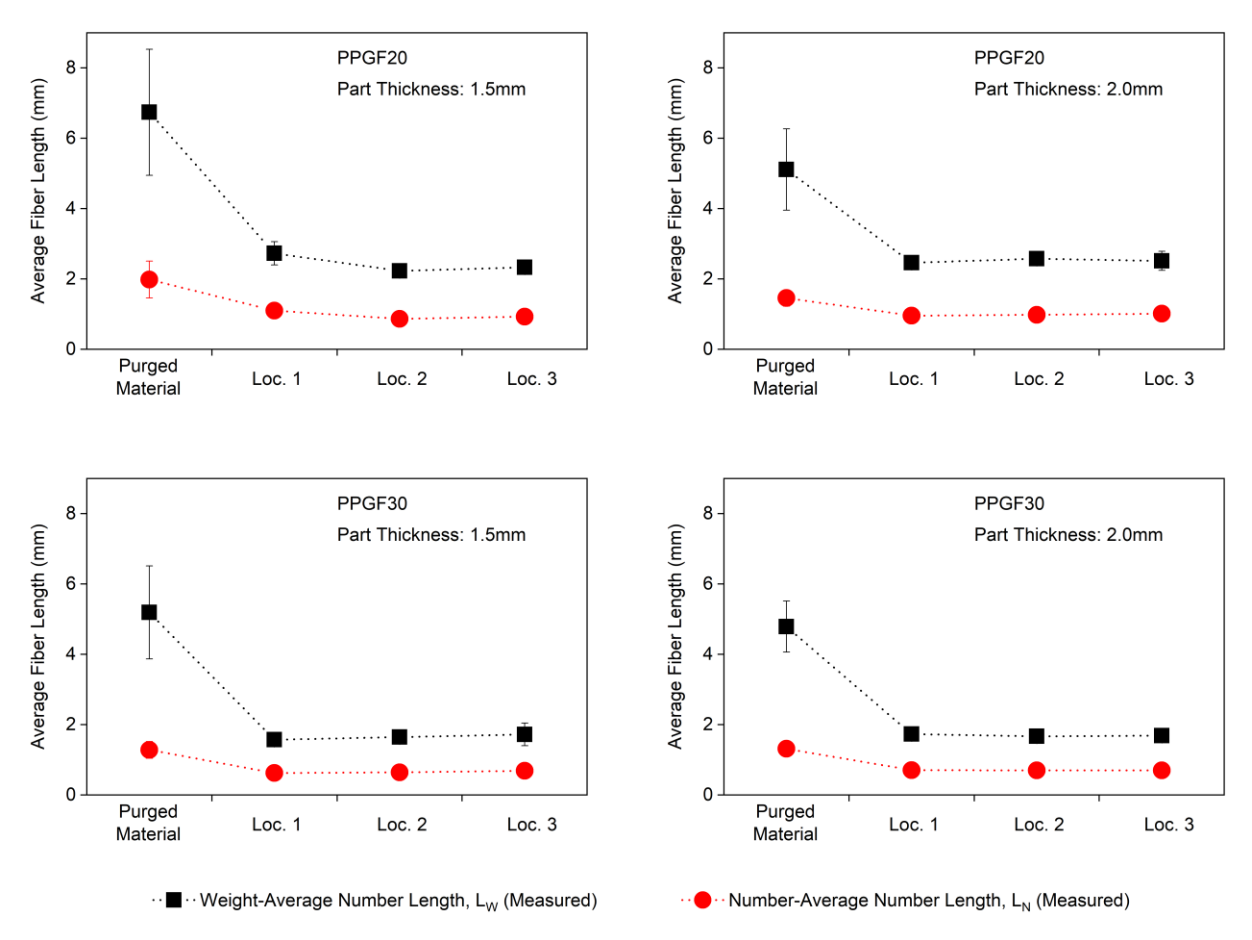
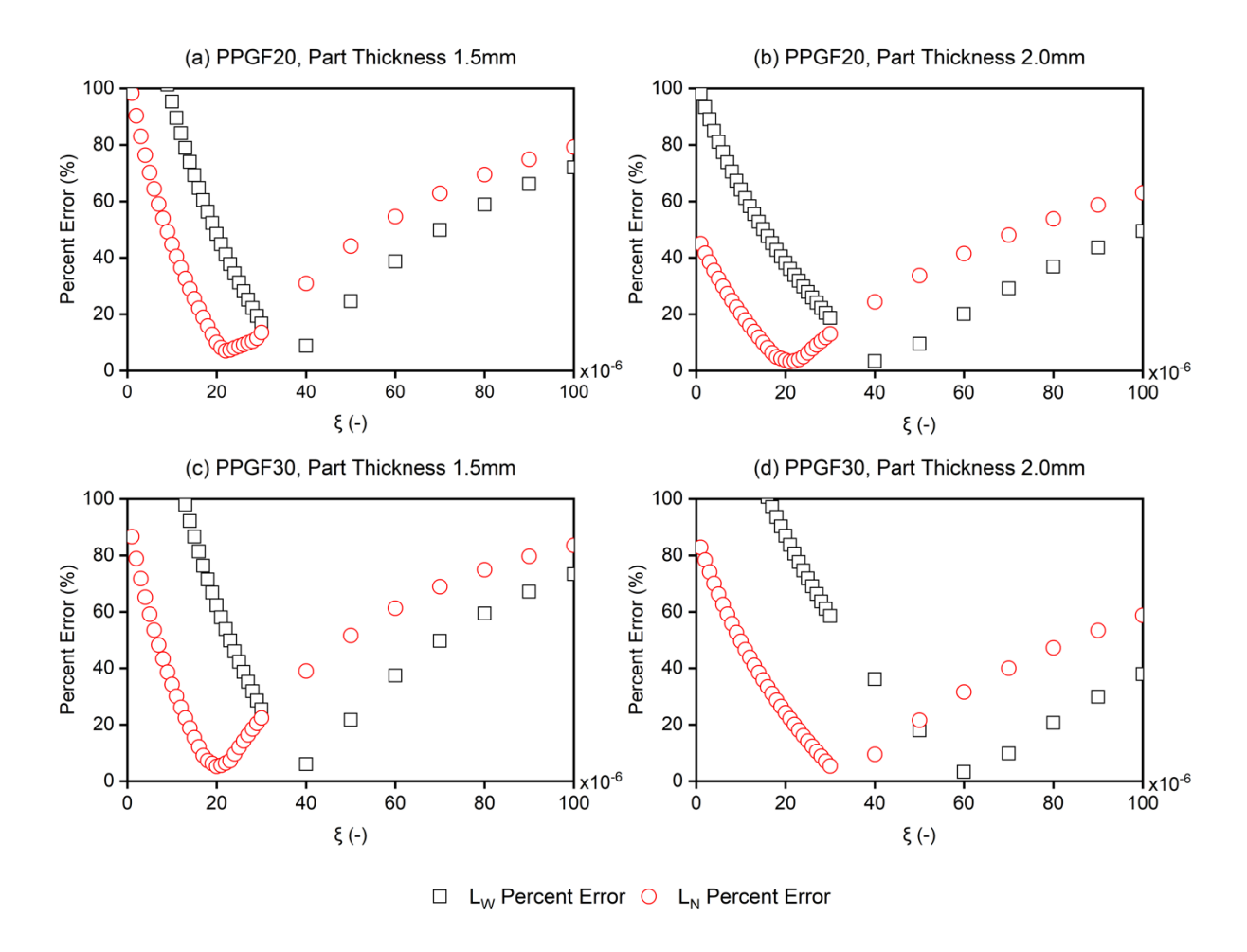


Figure 4.5 Result of the local fiber length measurement for all trials, showing the number-average fiber length,  $L_N$ , and the weight-average fiber length,  $L_W$  at four locations: in the purged material, close to the gate (Loc.1), at the center of the plate (Loc.2), and at the end of the flow (Loc.3)

# Modeling Approach

The fiber length measurement result from the purged material in Figure 4.5 was utilized as the initial fiber length in the Moldex3D simulation. To emulate the evolution of  $L_W$  and  $L_N$  respectively, separate simulations were conducted to represent the length changes for each result individually. Following the steps outlined in chapter 4.2, the  $\xi$  distribution was calculated and presented in Figure 4.6 for the injection-molded plaque. With no fiber-flow coupling enabled in the simulation, the viscosity of the flow field remains unaffected by the fiber orientation during simulation. In other words, the viscosity within the flow field remains constant across all simulations, and as a result, the only factor influencing the prediction of fiber length is its initial input value. Furthermore, it clearly demonstrates a trend that for lower fiber aspect ratios like  $L_N$ , the  $\xi$  distribution shifts to the left, whereas the curves shift to the right for  $L_W$ . Consequently, the  $\xi$  distribution presents an organized trend in the plots.



**Figure 4.6** The average percent error of  $\xi$  value for simulation result without fiber-flow coupling calculation of fiber length degradation for PPGF20 and PPGF30 with two thickness of plaques in Moldex3D.

When fiber-flow coupling calculation is enabled, the fiber orientation influences the viscosity. Distinct fiber lengths might orient differently within the flow field, thus influencing the viscosity during calculations. Figure 4.7 displays the distribution results for fiber-flow coupling enabled within the simulation. The curves for error% of  $L_W$  slightly shift to the left compared to  $L_N$ , indicating that a lower  $\xi$  corresponds to a reduced rate of deformation and leads to longer fiber length. Compared to Figure 4.6, the  $\xi$  distribution for different fiber aspect ratios shows higher convergence and lower values.

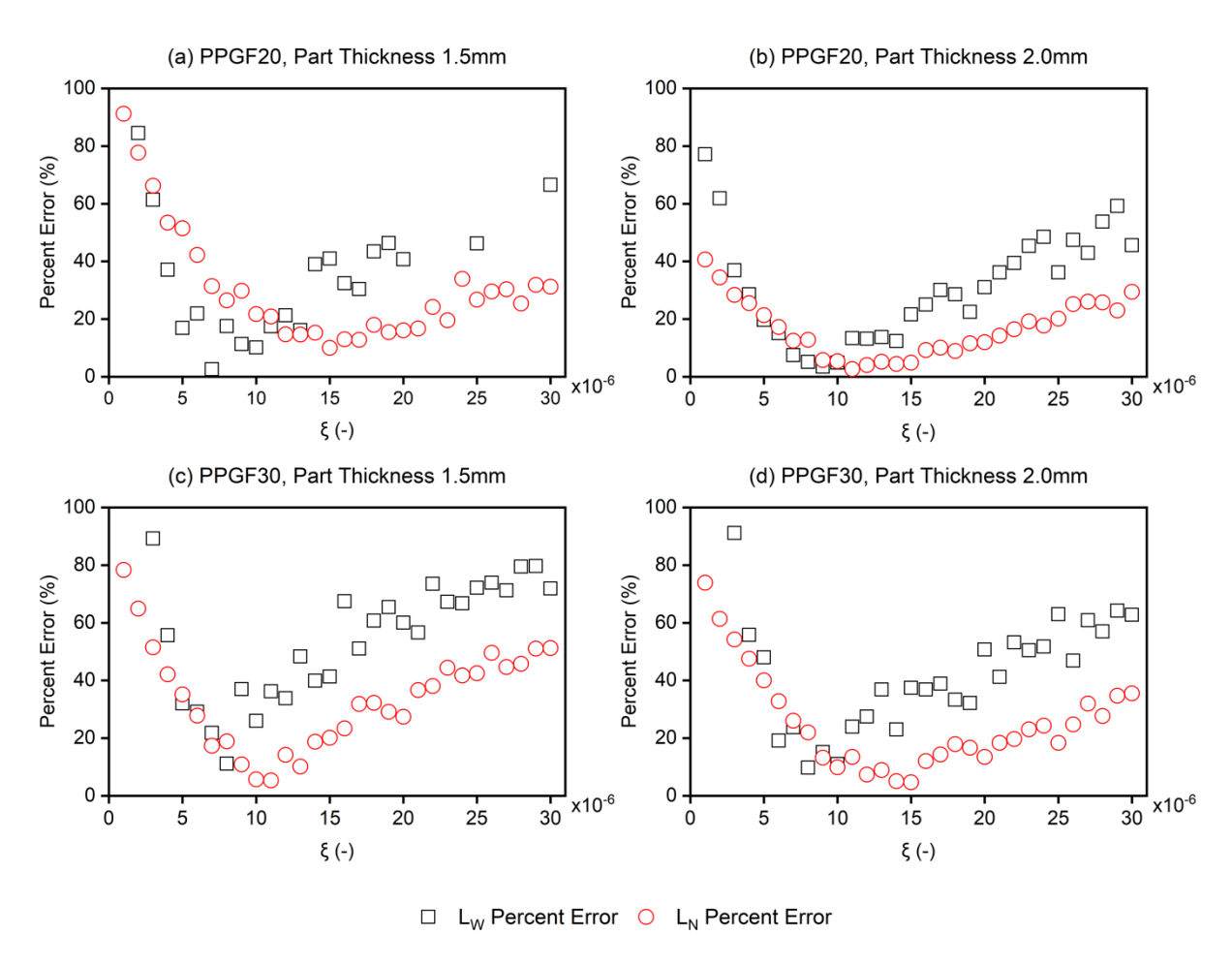


**Figure 4.7** The average percent error of  $\xi$  *value* for simulation result with fiber-flow coupling calculation of fiber length degradation for PPGF20 and PPGF30 with two thickness of plaques in Moldex3D.

# Prediction accuracy based on different fiber initial L/D

Using the optimized value obtained from Figure 4.6 and Figure 4.7, the optimal  $\xi$  values were plotted against various fiber aspect ratios and two different fiber contents. The predicted  $\xi$  values, calculated based on the fiber aspect ratios extracted from Figure 4.5, were then compared to the fiber length measurements depicted in Figure 4.8 and Figure 4.9. The results showed a high level of agreement in prediction accuracy for the calculated  $\xi$  values. This agreement serves as a crucial reference for future applications of the model.

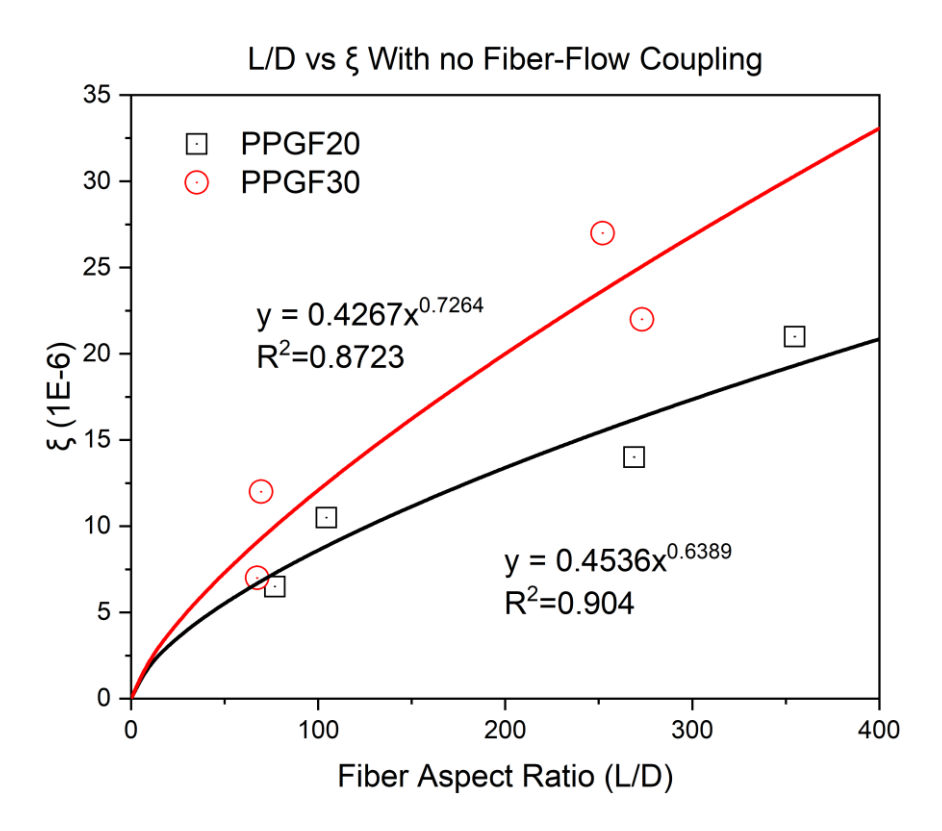
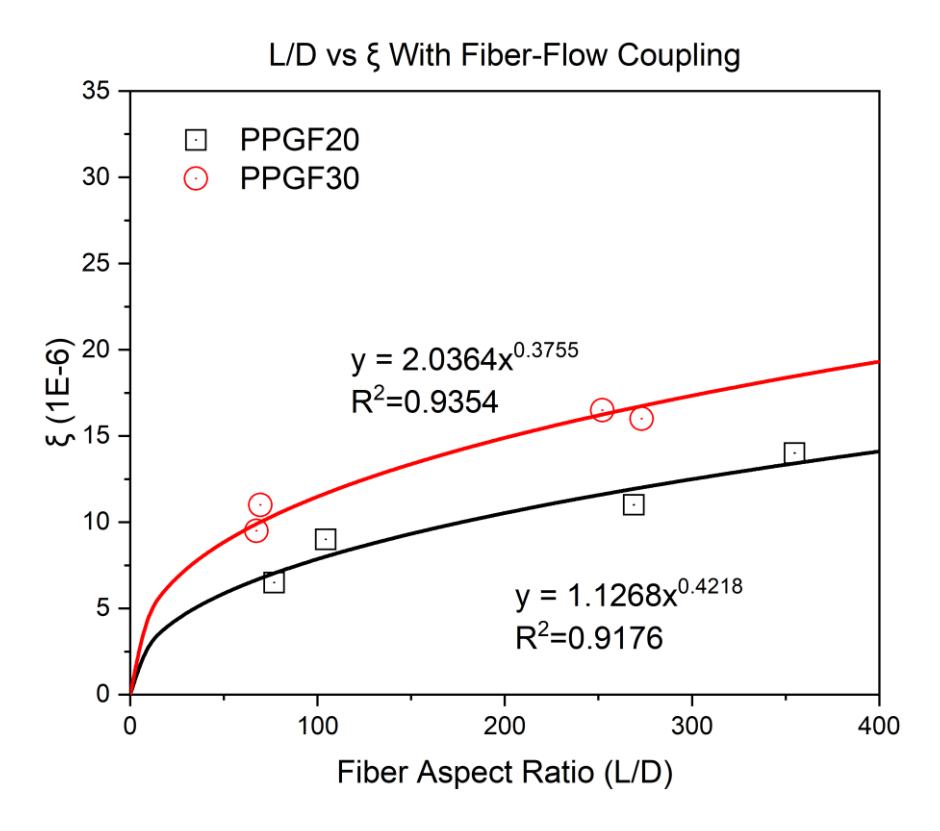


Figure 4.8 The optimum  $\xi$  from the simulation with disable fiber-flow coupling calculation as function of the initial fiber aspect ratio.



**Figure 4.9** The optimum  $\xi$  from the simulation with enable fiber-flow coupling calculation as function of the initial fiber aspect ratio.

Due to limitations in the processing conditions at the site, fibers might not achieve complete dispersion after passing through the plasticizing unit. This can lead to considerable variations in fiber length measurement results in the purged materials. To address this, a range of different fiber L/D ratios falling within the measurement range were employed to cross-validate the  $\xi$  predictions in Figure 4.7. The results presented in Table 11 demonstrate a noteworthy concurrence for fiber-flow coupling simulations with PPGF20 as an example. In other words, users can refer to the chart, select an appropriate  $\xi$  value based on the fiber aspect ratio, and anticipate good agreement under comparable processing conditions.

**Table 11** The validation test result with a different initial fiber length as input for the simulation.

No.	Material	Part	Fiber	Accuracy for Fiber-
110.	Materiai	Thickness	L/D	Flow Coupling
1	PPGF20	1.5	77	94%
2	FFGF20	1.5 mm	269	91%

#### Phelps model vs Modified breakage model

Using the optimum value found in Figure 4.7, Figure 4.10 presented the  $L_W$  results from Moldex3D simulation by comparing the Phelps model and modified breakage model. Additionally, the empirical model parameters from the Phelps model were used as an input for a Moldex3D simulation to compare with the modified breakage model. For the  $L_W$  result, the modified breakage model has good agreement in predicting the length degradation for both PPGF20 and PPGF30. While the Phelps model has more deviation in predicting the  $L_W$  for lower fiber content material. Using the optimum value for  $L_N$  found from Figure 4.7, Figure 4.11 presented the  $L_N$  results from Moldex3D simulation by comparing the Phelps and modified breakage models. For PPGF20, the modified breakage model agrees well with the experimental data. For PPGF30, the Phelps and modified breakage models yield a similar length degradation prediction. The modified breakage model generally showed good agreement compared to the Phelps model.

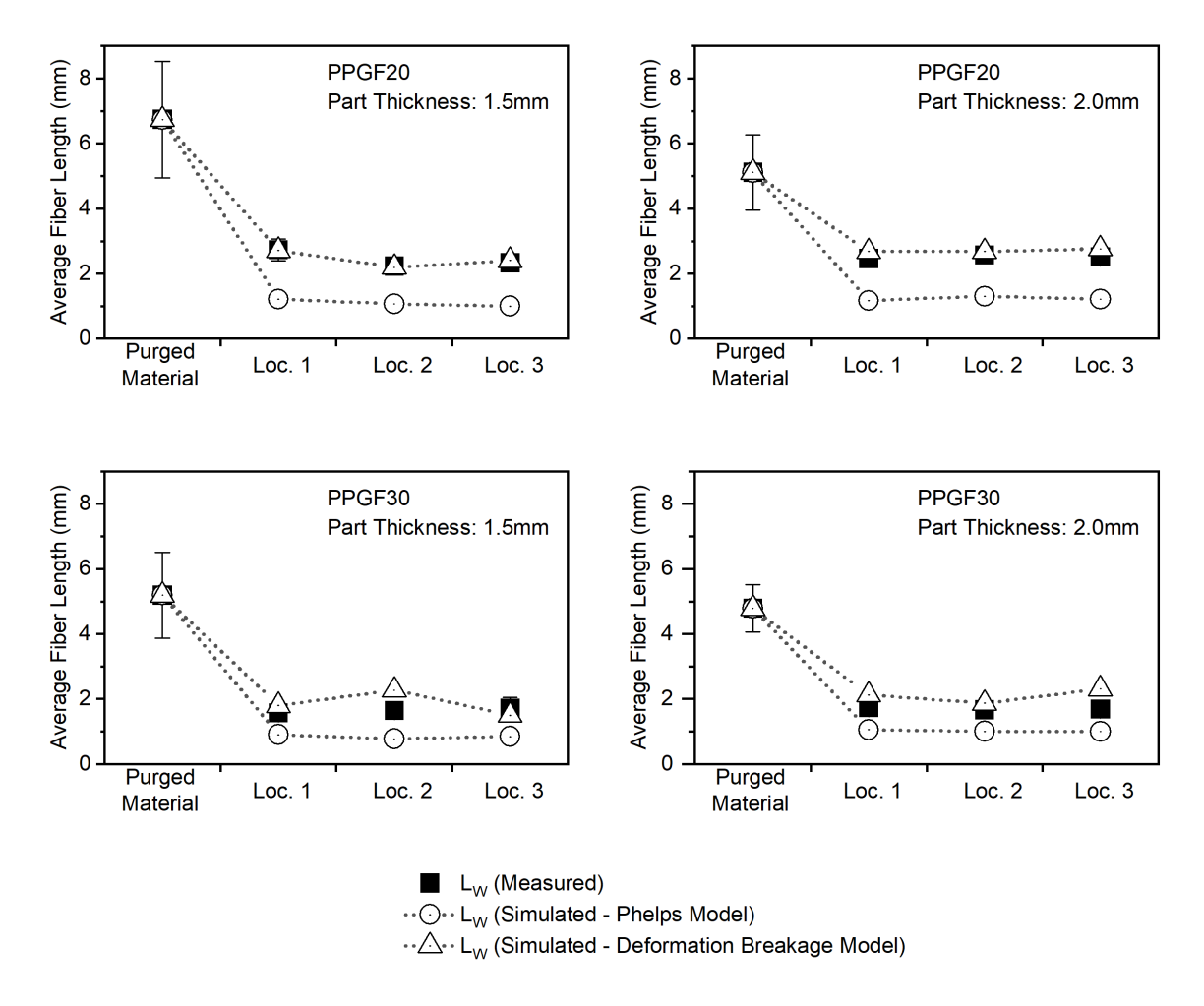
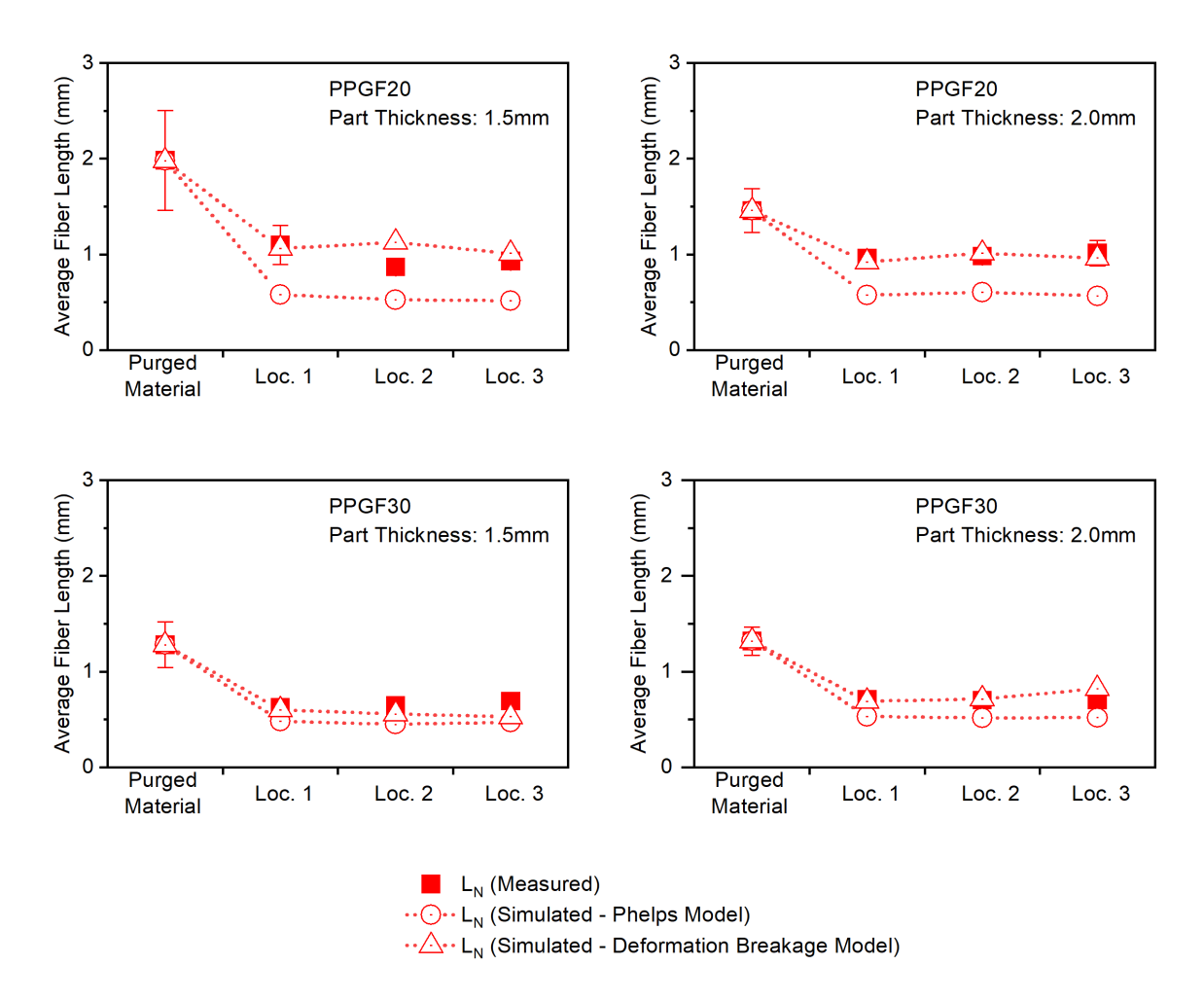


Figure 4.10 The comparison of weight-average fiber length  $(L_W)$  degradation between the modified breakage model and Phelps model for PPGF20 and PPGF30 with for 1.5 and 2mm-thick injection molded plaque.



**Figure 4.11** The comparison of number average fiber length ( $L_N$ ) degradation between the modified breakage model and Phelps model for PPGF20 and PPGF30 for 1.5 and 2 mm-thick injection molded plaque.

## 4.4. Effect on fiber length distribution

As fibers in the polymer matrix undergo the injection molding machine, the forces they are experiencing will cause them to break into segments with a length distribution. Since fiber length is crucial for determining the mechanical behavior of the final injection-molded part, understanding the length distribution will help researchers gain deeper insights into the process and further enhance it. Recognizing how fiber lengths change throughout the injection molding process aids in designing parts with more uniform properties, thereby reducing weak points in the final part. The knowledge acquired from studying fiber length distribution ultimately contributes to manufacturing parts with reliable and predictable performance. Due to the limitations of the software, providing a fiber length distribution as an initial input for the simulation is unfeasible. In order to investigate the distribution

of fiber breakage for each fiber length and understand how breakage occurs throughout the process, an extensive simulation was carried out using the geometry of an injection molded plaque and the optimal  $\xi$  determined in Chapter 4.3. Table 12 showed the initial fiber length used in the simulation ranged from 0.5mm to 15mm, with increments of 0.5mm, while the  $\xi$  value remained constant for all tested fiber lengths. After the simulation, the simulated average fiber length at each location were extracted from each location. The measured fiber length distribution at the purged location was used as a reference for determining the percentage of each length that experienced breakage during the simulation. This simulated fiber length distribution was then compared to the measured distribution profile at each test location.

**Table 12** The test input of integrating the fiber length distribution into simulation.

	Values			
Material	PPGF20, PPGF30			
Part Thickness 1.5 mm, 2.0 mm				
<b>Initial Fiber Length</b>	0.5 mm~15 mm			

In Figure 4.12, the length distribution for PPGF20 with a part thickness of 1.5 mm showed a strong agreement between the measured and simulated results when compared to  $L_W$  and  $L_N$ , respectively. The remaining results are provided in the appendix. However, the simulated distribution consistently shifts to the right, indicating that the model underestimates fiber breakage when employing the length distribution in the simulation. This may due to only one  $\xi$  value is utilized throughout the simulation with multiple initial fiber length conditions. This trend is observable in all locations except for location 4, which is next to the edge of the end part. In location 4, the measured results indicate the presence of a significant number of longer fibers that have been carried to the end of the part by the flow field which is not reflected in the simulation. The fiber length distribution for rest of the test conditions are provided in Appendix A.

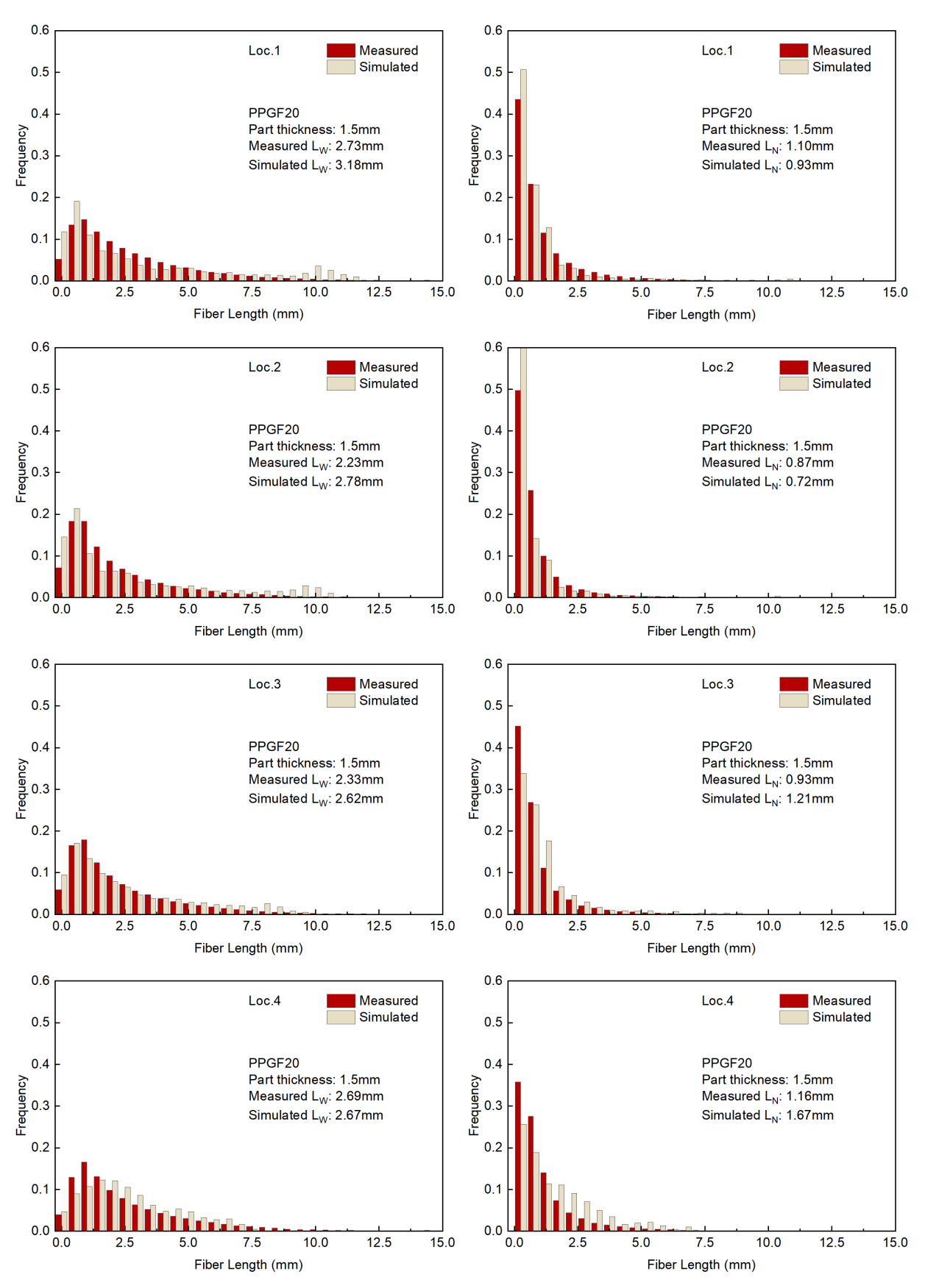


**Figure 4.12** The comparison of fiber length distribution between the measured results and the simulated fiber length distribution at four locations for PPGF20, 1.5 mm-thick injection molded plaque.

Using the simulated fiber length distribution,  $L_W$  and  $L_N$ , which consider the distribution, were calculated and then compared with the measured data. The comparison is shown in Figure 4.13. The results showed a good correlation with the  $L_N$  data, while slightly underpredicting the fiber breakage and thus resulting in slightly longer lengths in  $L_W$ .

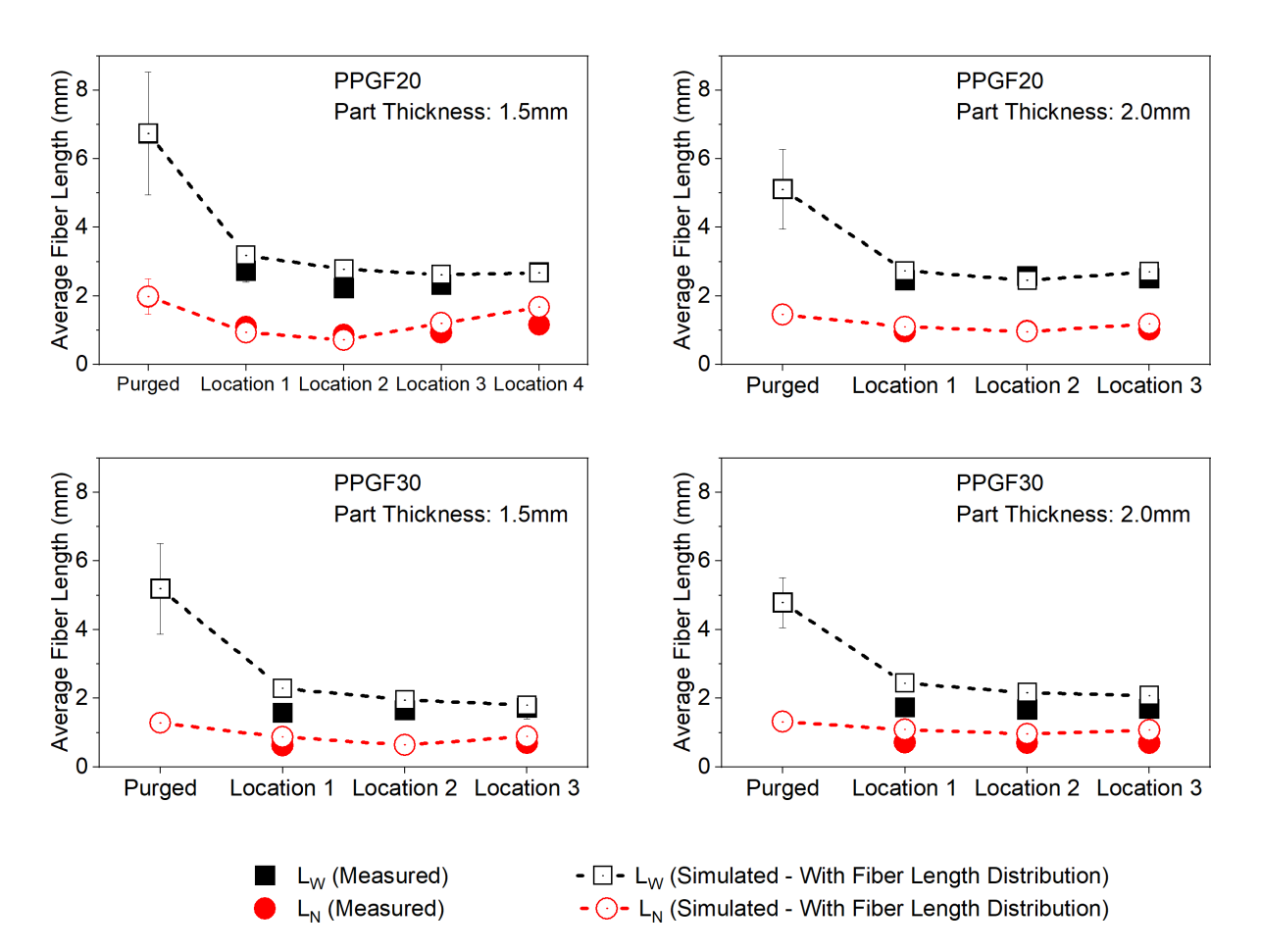


**Figure 4.13** The comparison of average fiber length degradation between the measured length and the simulated length with fiber length distribution integrated for PPGF20 and PPGF30 for 1.5 and 2 mm-thick injection molded plaque.

## 4.5. Effect on part geometry (Plaque vs Tailgate)

The second geometry employed in this study to validate the modified breakage model is the tailgate. The tailgate, found at the rear of a car, is typically installed in hatchback vehicles to facilitate opening and closing actions. It features a prominent central aperture designed for accommodating the backlight window. Various other apertures are also integrated to install components like the backlight, wiper motors, and a lifting handle. As for surface

finishing, it can be covered with leather or employ materials that don't necessitate post-processing to achieve a smooth surface, such as panels crafted from Polypropylene. In industrial production, tailgates are often manufactured using a combination of hot and cold runner systems. This approach aids in producing large components while expediting the manufacturing process. During production, the hot runner remains within the mold, while the cold runner is ejected along with the manufactured part. Subsequently, the cold runner system is trimmed post-ejection. Given the requirement for high-impact resistance, tailgates often employ materials with high fiber content to enhance their strength. In this study, the materials STAMAX 30YM240 (PPGF30) and STAMAX 40YM240 (PPGF40) were utilized to investigate the impact of geometry using the modified breakage model.

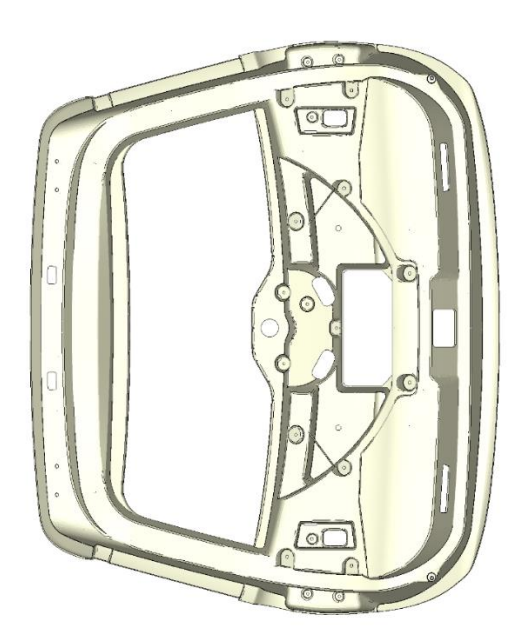


Figure 4.14 The geometry of an injection molded tailgate.

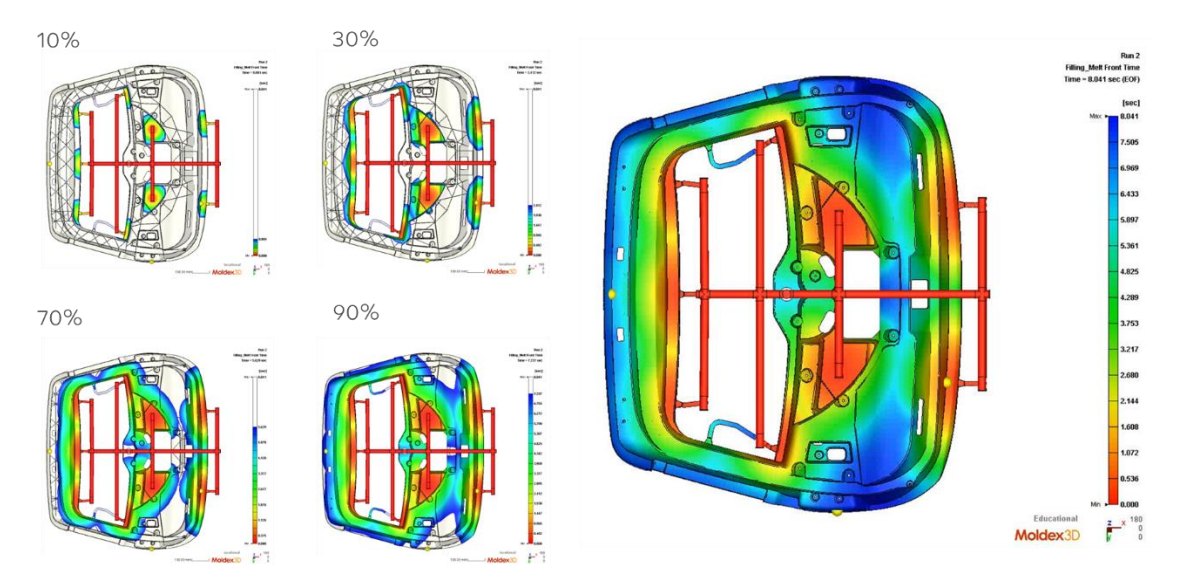
The mesh used in this study is the Solid mesh (BLM) in Moldex3D, and the processing condition is listed in Table 13.

Table 13 Processing condition of manufacturing injection molded tailgate part.

Parameter	Moldex3D		
Mold material	Aluminum 7075		

Mold temperature	50°C
Melt temperature	250°C
V/P switchover	99.5 % of volume
Injection time	8.0 s
Injection rate	616.7 cc/s

Figure 4.15 shows the filling result in the case of nine gates. The melt front showed that the polymer melt is injecting into the part simultaneously with the filling time of 8 seconds. Due to the large quantity of the gates used in the mold, multiple melt fronts are present within the mold. This may cause potential weak points such as the weld lines appearing on the part's surface. As the tailgate serves as a hinged door or panel at the rear of the vehicle, providing access to the cargo area, its mechanical strength is also a critical factor that must be carefully considered during manufacturing.



**Figure 4.15** The flow front profile of an injection molded tailgate at dfferent filling percentage with all gates open at once during injection stage.

Given that the tailgate not only offers access to the cargo area but also contributes to the vehicle's overall structural integrity, its strength and durability play a significant role in ensuring the safety of both passengers and transported goods. To achieve this, the orientation of fibers inside the part also needs to be considered during manufacturing.

Consequently, the alignment of fibers within the part plays a critical role in determining the part's strength and minimizing warpage during the cooling stage of injection molding. To achieve these goals, a valve gate system is introduced in this study. The valve gate system controls the flow of melted material within the mold, thereby influencing the final orientation of fibers within the part. This system involves a valve gate at the junction between the hot and cold runner channels. A movable pin within the valve gate can be adjusted vertically to control the gate openings and closures during the process to regulate the flow direction of the molten material. In other words, the integration of valve gates within the hot runner system empowers the control of material flow direction within the mold, subsequently impacting fiber orientation within the part and, in turn, influencing the warpage of the final injection-molded component. To change the filling behavior, altering the runner system is the only way as the part design is already fixed. In this study, nine valve gates are used in the hot runner system; the sequence of the gates is listed in Table 14.

Table 14 The sequence of the valve gate used in the hot runner for the injection molded tailgate.

Valve Gate	Open (%)	Close (%)	Open (%)	Close (%)
G1	99	End of Packing		
G2	83	End of Packing		
G3	83	End of Packing		
G4	63	End of Packing		
G5	63	End of Packing		
G6	49	69	100	End of Packing
G7	49	69	100	End of Packing
G8	0	69	100	End of Packing
G9	0	69	100	End of Packing

With the controlled valve gate, one can see that the melt front is now flowing from the right to left, as shown in Figure 4.16. The melt front is uniform across the part, providing a stable system for fibers to flow inside.

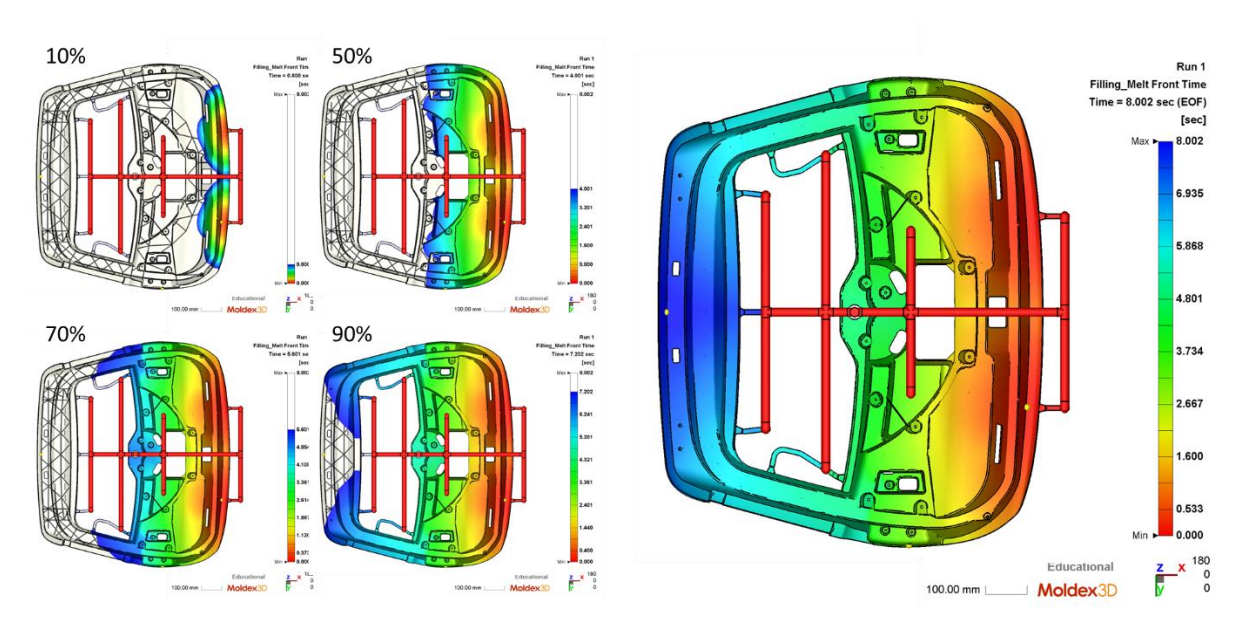


**Figure 4.16** The flow front of an injection molded tailgate at dfferent filling percentage with a predefined gates opening and clouses sequence during the process.

As the gate location is fixed, the optimization of the process is limited to controlling the valve gate's opening and closing times. This control depends on when the melt front reaches the gate area. When comparing two different filling pattern cases, the operation of the valve gate in a hot runner system can impact sprue pressure, as shown in Figure 4.17. In the case where all gates open at once, the sprue pressure generally increases and reaches its maximum at the end of filling. In contrast, for the valve gate case, the spike in the pressure profile is associated with each valve gate's opening time. Since more material passes through a gate each time a valve gate opens in the middle of the process, that gate experiences higher pressure than the others. Given the complex shape of the tailgate part, the ability to control the valve gate's opening and closing times allows for more precise control over how the mold cavity is filled.

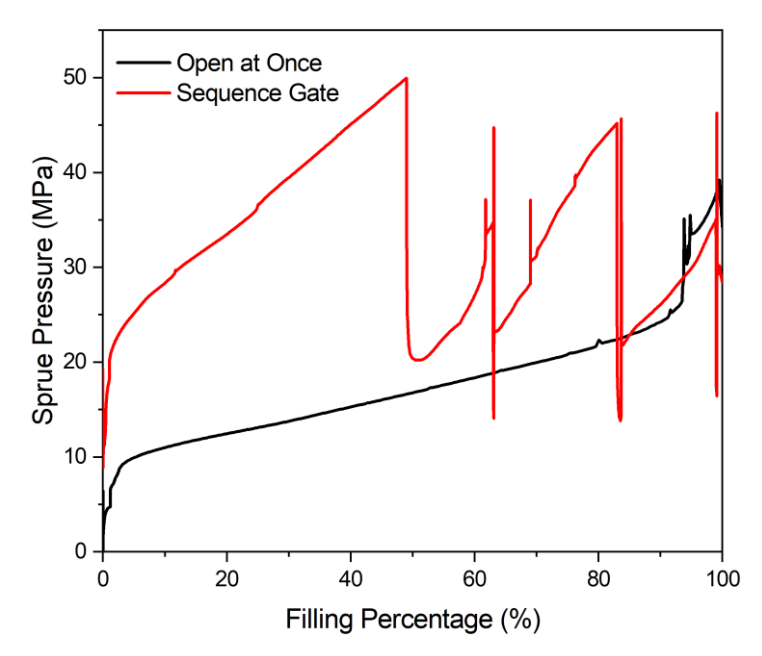


**Figure 4.17** The sprue pressure of two different valve gate open system: open all at once and sequence open for the injection molded tailgate.

Next, the fiber lengths were subsequently extracted from three distinct locations on the part: at the gate entrance (P1), halfway through the filling process (P2), and at the end of the filling (P3), as depicted in Figure 4.18. These results were then compared to the simulation outcomes to validate the efficacy of the modified breakage model. The fiber length from the purged material was employed to establish the initial fiber length. This approach bypasses the plasticizing section of the injection molding machine, focusing solely on analyzing the reduction in fiber length within the mold.

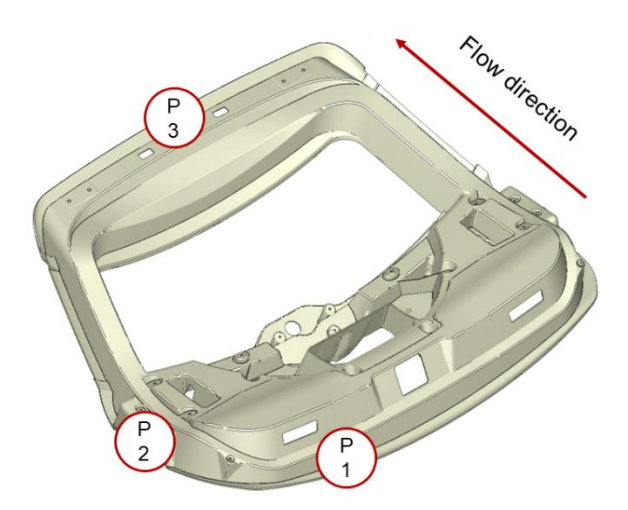


**Figure 4.18** Fiber length measurement at three locations of an injection molded tailgate where P1 is in the beginning of the filling, P2 is at 50% of the filling, and P3 is at the end of filling.

Following the procedure described in Chapter 4.2, the  $\xi$  distributions for PPGF30 and PPGF40 of the tailgate were obtained and the result of fiber attrition prediction from the optimum  $\xi$  are presented in Figure 4.19.

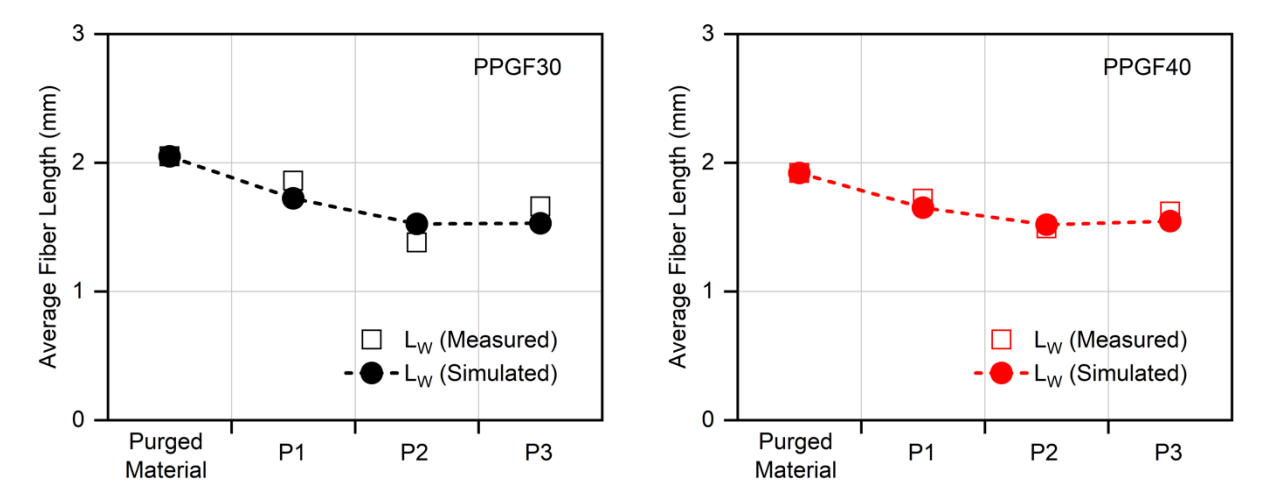


**Figure 4.19** The comparison of average fiber length degradation between the modified breakage model and the measured result for PPGF30 and PPGF40 for the injection molded tailgate.

While the results demonstrated a favorable alignment, indicating the model's capability to predict fiber attrition within injection molding when the correct  $\xi$  is utilized, there is a concern when applying this model to various part designs. This concern arises due to the  $\xi$  distribution displaying an offset for the two different geometries that have been validated thus far, as illustrated in Figure 4.20. The  $\xi$  distribution consistently exhibits a similar trend under comparable processing conditions. Interestingly, neither the fiber content in a material nor the part's thickness seems to significantly influence the  $\xi$  distribution, when compared to variations in processing conditions.

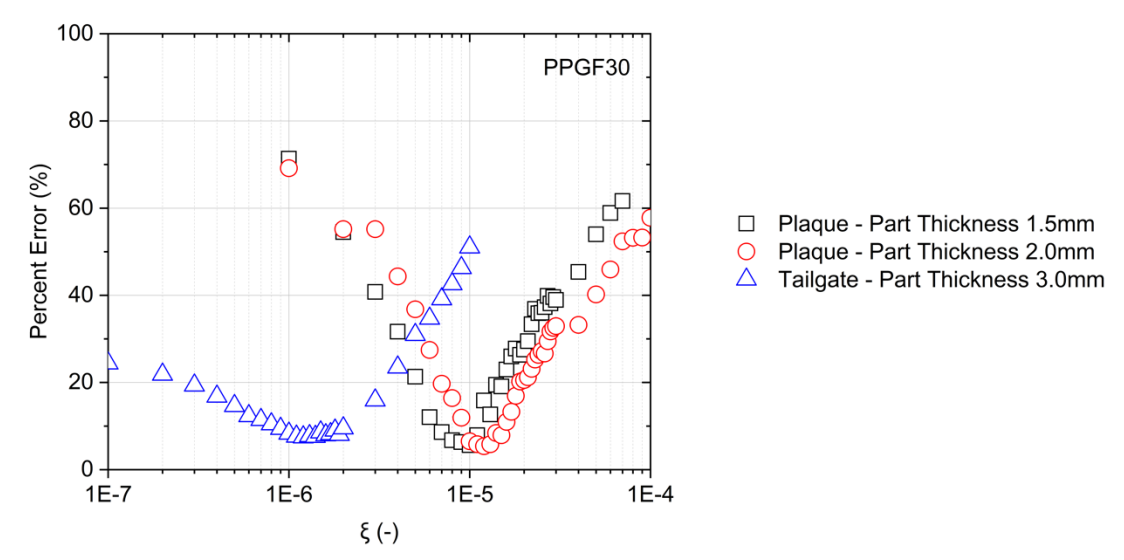


**Figure 4.20** The  $\xi$  distribution of the same material (PPGF30) with two different geometries and part thickness.

To enhance the applicability of this model for users, the establishment of a standardized set of parameters is imperative. Up until now, the model has been subjected to testing with two distinct geometries: the simple plaque and the tailgate with different fiber contents and part thickness as shown in Table 15. Analyzing the distribution of variation between the predicted and actual fiber lengths, it becomes evident that the parameter  $\xi$  can deviate by an order of magnitude. Therefore, determining the key factor responsible for this deviation becomes an essential goal.

**Table 15** The comparison of the cases that has been validated using the modified fiber breakage model.

	Plaque	Tailgate		
Geometry				
Material	PPGF20, PPGF30	PPGF30, PPGF40		
Part Volume	36 cc	4933 сс		
Thickness	1.5 mm, 2.0 mm	3.0 mm		

When considering fiber breakage, researchers commonly rely on two determining factors to characterize the ability of fiber attrition during polymer processing: shear rate and shear stress. Both factors will be analyzed in the following section.

#### Shear Rate Profile

Without fiber-flow coupling, the viscosity profile remains unaffected by the fiber orientation. In other words, both shear rate and shear stress profile remain constant for same fiber content material, regardless of the initially chosen fiber aspect ratio for the simulation. While employing flow coupling consideration, the length of fibers now impacts the viscosity profile and thus leads to a distribution of the shear rate in the simulation. Thinner the part led to a higher shear rate. Overall, the shear rate for injection molded plaque remains relatively consistent as the melt front is continuously injected into the mold. In the case of the tailgate, the shear rate undergoes significant fluctuations due to the control exerted by the sequence of the valve gates in the hot runner system. Figure 4.21 presents the shear rate profile around P1. Once Gate 9 is closed at a filling percentage of 69%, there's a significant drop in the shear rate profile of the tailgate as no more material is injected through Gate 9 which is closest to P1.

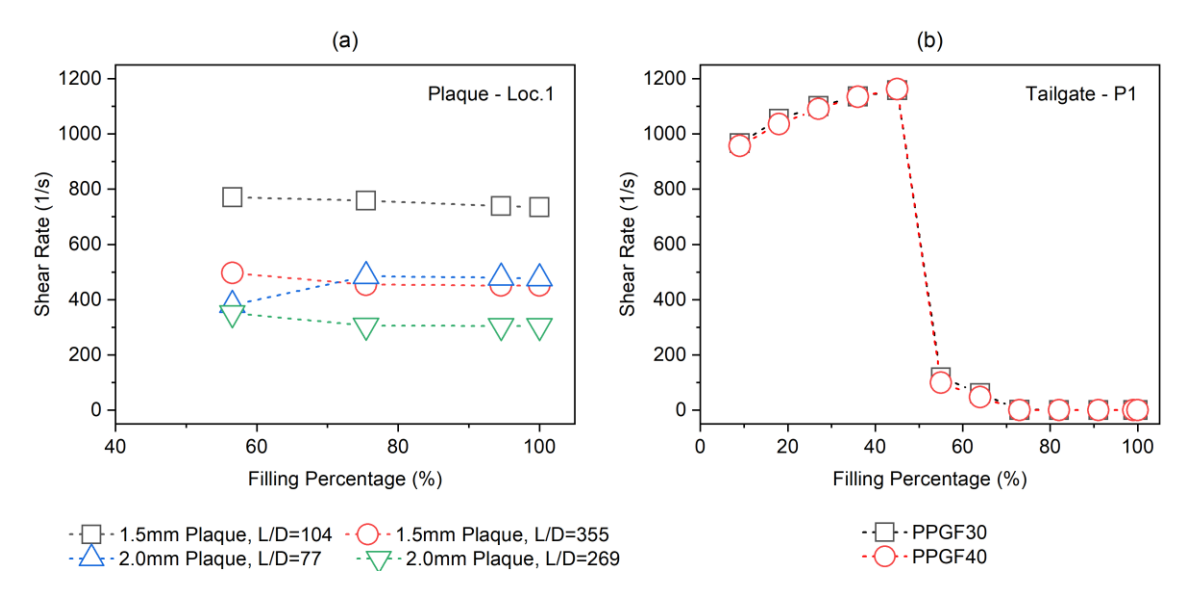


**Figure 4.21** The average shear rate profile across the part thickness in the simulation: (a) Location one in injection molded plaque, (b) P1 in injection molded tailgate

Next, the optimal  $\xi$  values have been determined based on the length predictions from the simulation. The shear rate profiles corresponding to each optimal  $\xi$ , selected for injection molded plaques with varying fiber content and part thickness, were extracted and compared to the profile associated with the tailgate part. The distinctions are illustrated in Figure 4.22. Notably, there is no indication of a positive relationship between the optimal  $\xi$  and the shear rate profile within the simulation.

	Case 1	Case 2	Case 3	Case 4	Case 5	Case 6	Case 7	Case 8
Computational	No Fiber-Flow Coupling			Eiber Flow Counling				
Environment				Fiber-Flow Coupling				
Part Thickness	1.5mm	1.5mm	2.0mm	2.0mm	1.5mm	1.5mm	2.0mm	2.0mm
Fiber <i>L/D</i>	104	355	77	269	104	355	77	269

**Table 16** The cases condition studied to analyze the relationship between two different geometries.

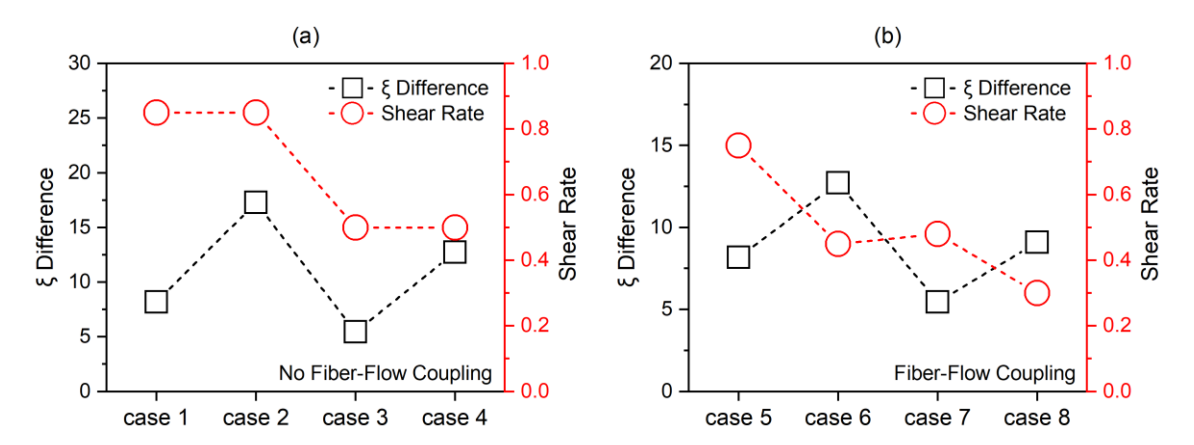


**Figure 4.22** The comparison between the  $\xi$  difference of plaque versus tailgate and the difference in shear rate profile: (a) no fiber-flow coupling enabled in computation, (b) fiber-flow coupling enabled in computation.

#### Shear Stress Profile

On the other hand, the shear stress varies significantly with different  $\xi$  values employed within the system (Figure 4.23). Lower  $\xi$  values correspond to a reduced rate of deformation, leading to a deceleration in fiber breakage. Consequently, the system exhibits higher shear stress levels. The difference is more significant with higher fiber L/D ratio. Though it is not a linear relationship, it can be observed that higher L/D ratio will lead to higher shear stress in the system. In the case of the tailgate, the shear stress drops when the nearby gate is closed due to the sequence in the valve gates. However, it maintains a relatively constant level in comparison to the shear rate profile. This stability is attributed to the fact that even when the nearby gate is closed, the melt continues to flow out from other gates. The melt flow might also circulate back to P1, leading to ongoing fiber breakage throughout the process.

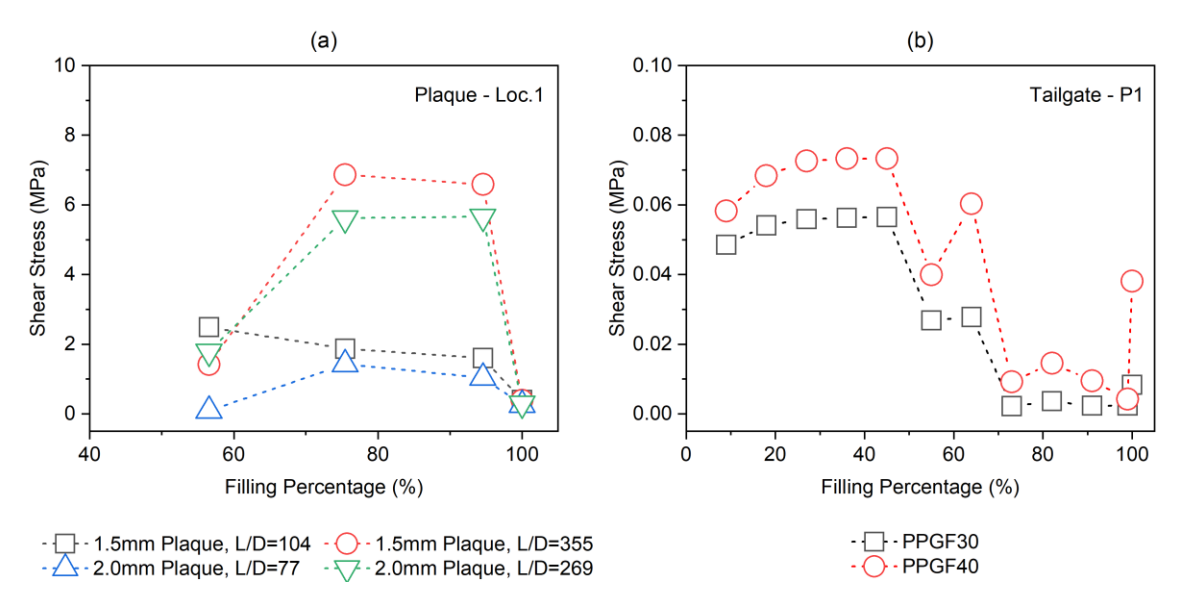


**Figure 4.23** The average shear stress profile across the part thickness in the simulation: (a) Location one in injection molded plaque, (b) P1 in injection molded tailgate

Next, the shear stress profiles corresponding to each optimal  $\xi$ , selected for injection molded plaques were also extracted and compared to the profile associated with the tailgate part. The distinctions are illustrated in Figure 4.24. Unlike the shear rate, there's a strong correlation between the optimal  $\xi$  and the corresponding shear stress profile in the simulation. This is a promising finding as now there's a guideline for researchers to follow when applying the modified breakage model to a different processing condition or a different part geometry.

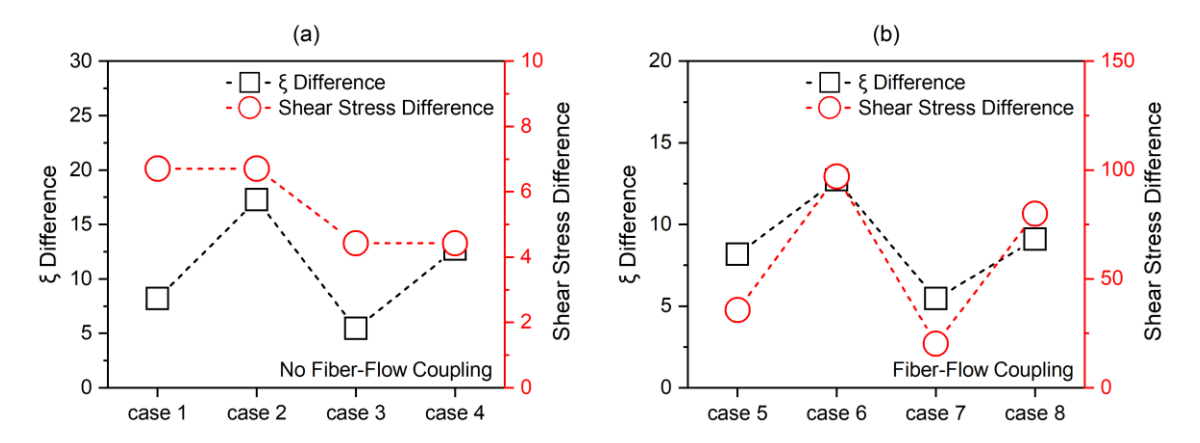
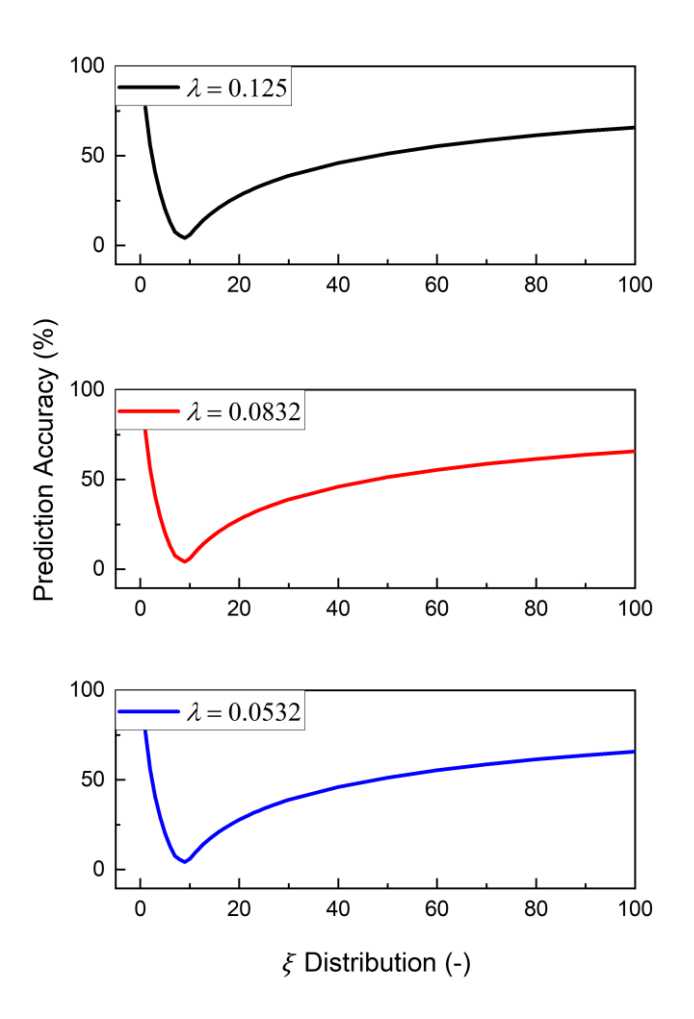


Figure 4.24 The comparison between the  $\xi$  difference of plaque versus tailgate and the difference in shear stress profile: (a) no fiber-flow coupling enabled in computation, (b) fiber-flow coupling enabled in computation.

# 5. Shear Stress Induced Fiber Attrition Model

During the investigation into the influence of  $\lambda$  on fiber length prediction, no robust evidence has shown a significant impact of  $\lambda$  on the simulation results (Figure 5.1). Initially,  $\lambda$  was assigned as a parameter solely dependent on the fiber content within the material, immune to the effects of processing conditions.



**Figure 5.1** The  $\xi$  distribution with different  $\lambda$  values used in the simulation.

Figure 5.2 below showed that  $L_W$  decreased from 15 mm down to 1.5 mm for 50 rpm and to 0.75 mm for 100 rpm from the Couette flow rheometer experimental results conducted by Bechara [23].

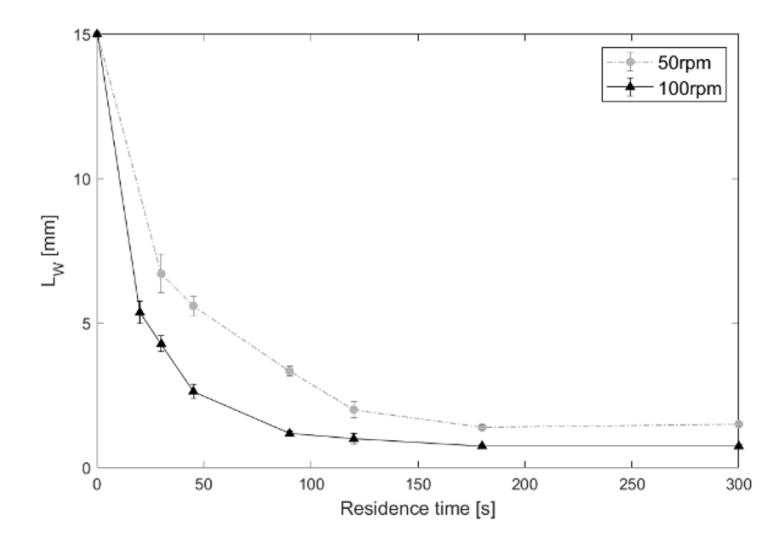


**Figure 5.2** The reduction in fiber length as a function of residence time for PPGF30 at two rotational speeds with a melt temperature of 250°C [23].

Below the  $\lambda$  value was validated with the fiber length data extracted from Figure 5.2.As the fiber's young's modulus and diameter is known, the matrix viscosity was estimated with the material data sheet of PPGF30 at 250°C, and the shear rate was calculated based on the rotational speed of the experiment. The calculation is shown below:

$$\lambda_{50\text{rpm}} = \frac{\ln(\frac{L_{\infty,1}}{d_f})}{\left(\frac{\sigma_u}{\eta_{m,1}\dot{\gamma}_1}\right)^{1/2}} = \frac{\ln(1.500/0.019)}{\text{power}(2.00\text{E}+10/49585.017, 0.50)} = 1.2431\text{E} - 01$$

$$L_{\infty,2}$$
(5.1)

$$\lambda_{100\text{rpm}} = \frac{\ln(\frac{L_{\infty,2}}{d_f})}{\left(\frac{\sigma_u}{\eta_{m,2}\dot{\gamma}_2}\right)^{1/2}} = \frac{\ln(0.75/0.019)}{\text{power}(2.00\text{E}+10/82749.493, 0.50)} = 8.0293\text{E} - 02$$
 (5.2)

Based on the provided experimental conditions, it is evident that the calculated  $\lambda$  differs even within materials of the same fiber content. As discussed earlier,  $\lambda$  was initially defined as a material-dependent parameter, implying its consistency within materials with the same fiber content material. Upon comparing with the average interaction coefficient presented in Figure 5.3, it becomes apparent that  $\lambda_{100\text{rpm}}$  demonstrates a more favorable correlation with the reference. In contrast,  $\lambda_{50\text{rpm}}$  aligns more closely with the 20 wt% value listed in the reference. This suggests that  $\lambda$  is influenced not only by the fiber content within the material but also by the speed of the flow field which is the rpm in this case.

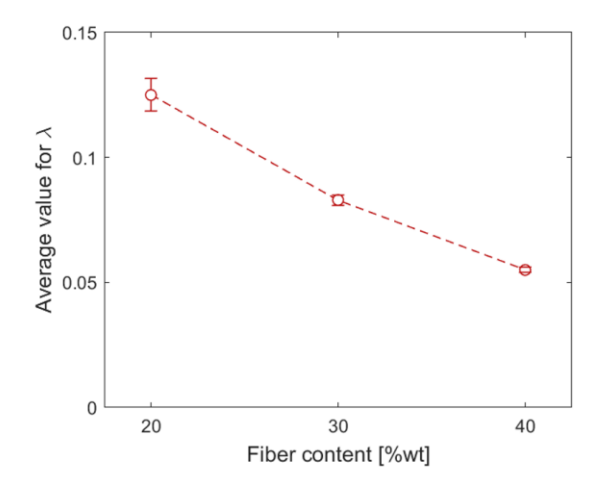


**Figure 5.3** Average interaction coefficient  $\lambda$  as function of fiber concentration [27].

However,  $\lambda$  should be pure material dependent parameter and have no influence on the experimental condition according to the original assumption. Hence, the  $k_f$  in the original equation is only related to the shear rate. However, according to the simulation result in Figure 4.24, it shows higher correlation with the shear stress instead. This makes more sense because if the shear rate of the flow field is large but the viscosity is small, the shear stress in the system may not be sufficient to break a fiber. Thus, the modified breakage model has been reorganized, and a dimensionless analysis has been conducted to understand the relationship between each parameter in the following section.

Equation (4.5) and equation (4.6) was reorganized with dimensionless analysis as equation (5.3) where y is set between 1 to 0. This dimensionless analysis eliminates the influence of the initial fiber length ( $L_0$ ) and the final fiber length ( $L_\infty$ ). Thus, any values of  $L_\infty$  and processing condition can be accommodated with an appropriate choice of  $k_f$  for the fiber attrition prediction.

$$y = \frac{L - L_{\infty}}{L_0 - L_{\infty}} \tag{5.3}$$

The corresponding boundary conditions of the y:

$$y(0) = \frac{L(0) - L_{\infty}}{L_0 - L_{\infty}} = \frac{L_0 - L_{\infty}}{L_0 - L_{\infty}} = 1$$
 (5.4)

$$y(\infty) = \frac{L(\infty) - L_{\infty}}{L_0 - L_{\infty}} = \frac{L_{\infty} - L_{\infty}}{L_0 - L_{\infty}} = 0$$
 (5.5)

If derived the y equation with time,

$$\frac{Dy}{Dt} = -k_f y \tag{5.6}$$

After the integration and applied the boundary condition when y(0) = 1

$$y = \frac{L - L_{\infty}}{L_0 - L_{\infty}} = e^{-k_f t} \tag{5.7}$$

The new expression of  $L_{\infty}$  and  $k_f$  is as below,

$$\frac{L_{\infty}}{d_f} = f\left(\frac{\sigma_u}{\eta_m \dot{\gamma}}\right) = \lambda \left(\frac{\sigma_u}{\eta_m \dot{\gamma}}\right)^{\alpha} = \lambda \left(\frac{\eta_m \dot{\gamma}}{\sigma_u}\right)^{-\alpha} \tag{5.8}$$

$$k_f = g\left(\frac{\sigma_u}{\eta_m \dot{\gamma}}\right) = k_0 \left(\frac{\sigma_u}{\eta_m \dot{\gamma}}\right)^{-\beta} = k_0 \left(\frac{\eta_m \dot{\gamma}}{\sigma_u}\right)^{\beta} \tag{5.9}$$

These new expressions will have four parameters:  $\alpha$ ,  $\beta$ ,  $k_0$ , and  $\lambda$  instead of only two parameters ( $\lambda$  and  $\xi$ ). As discussed above in chapter 4.5 which shear rate is not directly related, the new expression of  $k_f$  (Equation (5.9)) is now related to the shear stress of the flow field. The unit of  $k_0$  is the same as  $k_f$  where the unit is  $s^{-1}$ , and  $\left(\frac{\sigma_u}{\eta_m \dot{\gamma}}\right)$  is dimensionless Fiber breakage is now represented by the friction stress instead of shear rate. Thus,  $k_0$  has nothing to do with the flow field, nor with the fiber length. For example, if temperature changes, the original  $k_f$  expression cannot account for the difference in viscosity with respect to temperature changes. Consequently, all processing temperatures will yield the same fiber breakage rate. However, since the viscosity of the polymer matrix varies with processing temperature, longer fibers have higher resistant over the flow and thus the  $k_f$  may also change. In addition, with the two experiments shown in Figure 5.2,  $k_f$  can be obtained by fitting the curves in the figure. The corresponding  $k_f$  from different rpm of the experiment will result in different values as shown below.

$$k_{f.50\text{rpm}} = 0.0279 \tag{5.10}$$

$$k_{f,100\text{rpm}} = 0.0500$$
 (5.11)

With the calculated  $k_f$ , the fiber length reduction curves over the different residence time with two different rotation speed can be regenerated below:

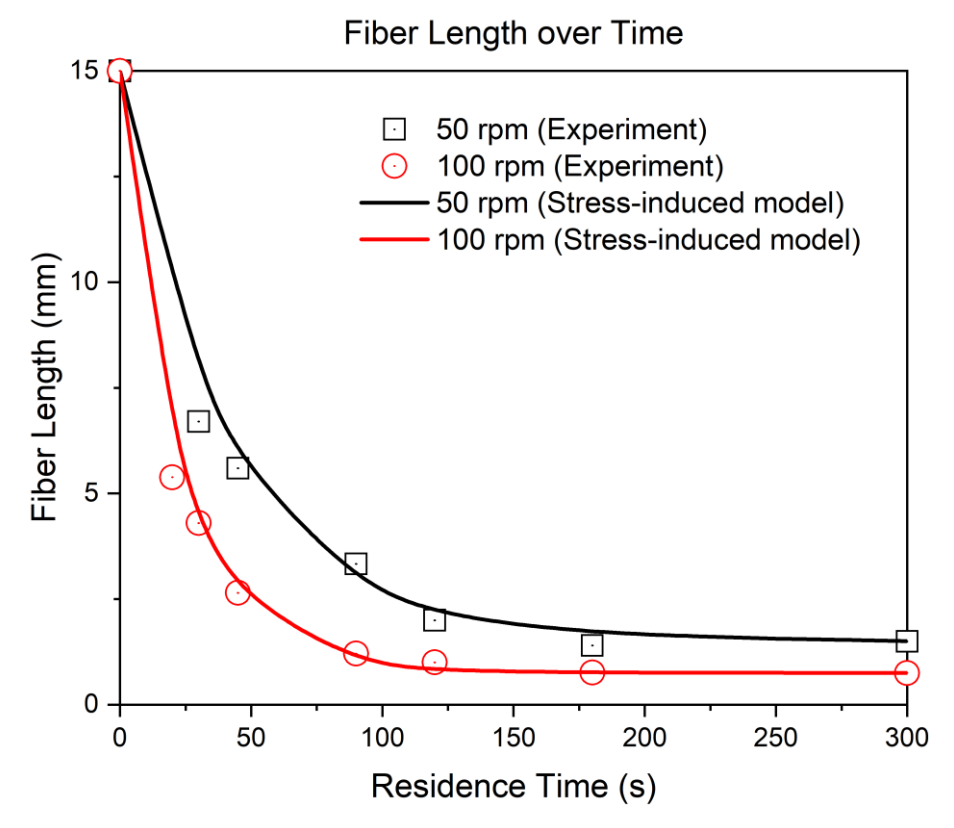


**Figure 5.4** The fitting curves of fiber length reduction over residence time with calculated  $k_f$ .

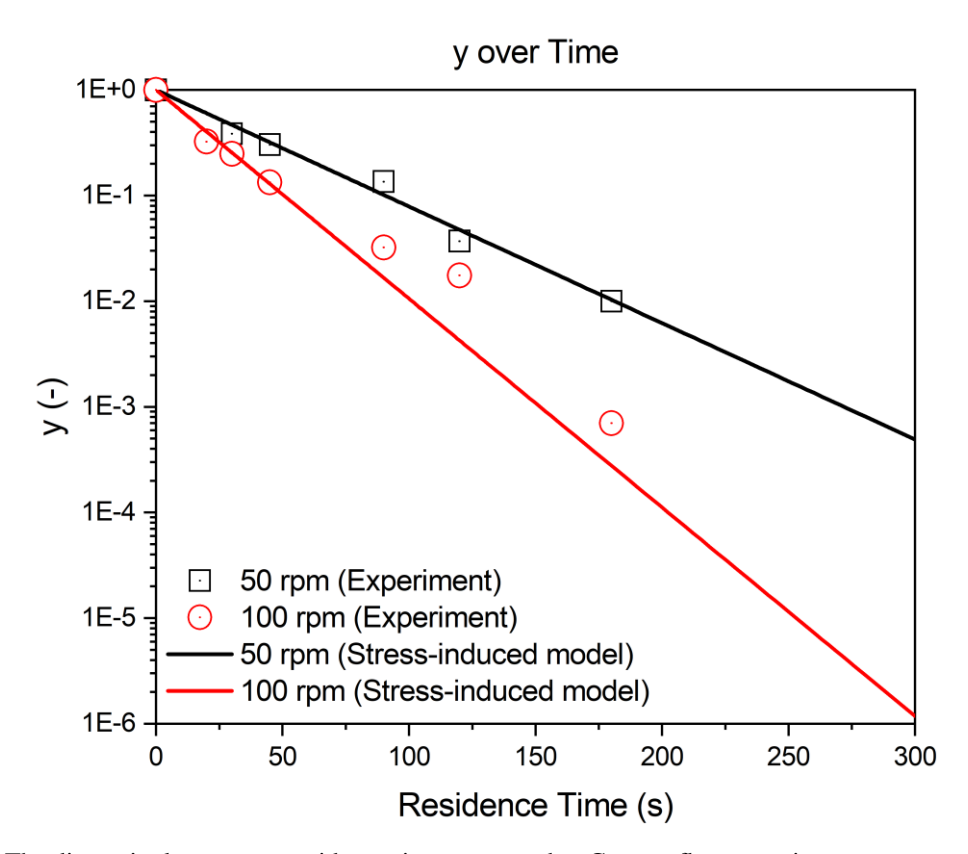


Figure 5.5 The dimensionless y over residence time compared to Couette flow experiments.

In addition, with the two  $L_{\infty}$  from Couette flow experiments in Figure 5.2, it is possible to calculate  $\lambda$  and  $\alpha$  in equation (5.8) as shown below:

$$\alpha = \frac{ln(\frac{L_{1\infty}}{L_{2\infty}})}{ln(\frac{\eta_2\dot{\gamma}_2}{\eta_1\dot{\gamma}_1})} = \frac{ln(1.500/0.750)}{ln(82749.493/49585.017)} = 1.353462$$
 (5.12)

$$\lambda = \frac{\ln(\frac{L_{1\infty}}{d_f})}{\left(\frac{\sigma_u}{\eta_{1m}\dot{\gamma}_1}\right)^{\alpha}} = \frac{\ln(1.500/0.019)}{\text{power}(2.00\text{E}+10/49585.017, 1.353462)} = 2.0430\text{E}-06$$
 (5.13)

Here  $\alpha = 1.35$  which is different from the original equation (4.3) where  $\alpha = 0.5$ . This newly derived value satisfies two different rotation speeds: 50 rpm and 100 rpm in the study, which means that the new  $\alpha$  and  $\lambda$  values are valid for the same fiber content even with different rotational speeds in the system.

Instead of the linear relationship as in equation (4.4), the  $k_f$  is regenerated with  $\beta$  as the curve slope:

$$k_f = \xi \dot{\gamma}^\beta \tag{5.14}$$

Using experimental data in Figure 5.2 to validate  $\beta$  value:

$$\beta_A = \frac{\ln(\frac{k_{f,1}}{k_{f,2}})}{\ln(\frac{\dot{\gamma}_1}{\dot{\gamma}_2})} = \frac{\ln(0.0500/0.0279)}{\ln(36.652/18.326)} = 0.841663$$
 (5.15)

Here can see that the rate of deformation does not have a linear relationship with the shear rate in the system. Thus, with the  $k_f$  calculated above in equation (5.10) and equation (5.11), equation (5.9) the slope of the curves will be  $\beta_B$  as below:

$$\beta_{\rm B} = \frac{\ln(\frac{k_{f,1}}{k_{f,2}})}{\ln(\frac{\eta_1\dot{\gamma}_1}{\eta_2\dot{\gamma}_2})} = \frac{\ln(0.0500/0.0279)}{\ln(82749/49584)} = 1.1392$$
 (5.16)

And the corresponding  $k_0$  value:

$$k_{0, 50RPM} = \frac{k_{f,1}}{\left(\frac{\eta_m \dot{\gamma}}{\sigma_u}\right)^{\beta_B}} = \frac{0.0279}{\left(\frac{49584.86}{2.00E+10}\right)^{1.1392}} = 6.7821E+04$$
(5.17)

$$k_{0, 100RPM} = \frac{k_{f,2}}{\left(\frac{\eta_m \dot{\gamma}}{\sigma_u}\right)^{\beta_B}} = \frac{0.0500}{\left(\frac{82749.23}{2.00E+10}\right)^{1.1392}} = 6.7821E+04$$
(5.18)

Where  $\dot{\gamma} = cN$ , N=RPN of the Couette flow experiment. Interesting enough, the  $k_0$  is the same for two different

rpm used in the experiment.

Now the new model has nothing to do with the flow field. Therefore, this stress induced model can be applied to a wider range of conditions without adjusting the parameters each time. The future work involves validating this new approach with current data in hand.

## 6. Summary

A particle-level model for computing the breakage behavior for glass fiber in a polypropylene matrix under simple shear flow was studied. The simulation first showed how the variables can be tuned to obtain detailed information about breakage during the processing and develop an understanding of the fiber length reduction. Based on the results obtained from the simulation, the length validation on fiber breakage was performed and compared with the Couette flow experiment. However, unsteady initial breakage was observed due to high fiber volume fraction material used for the experiment. A relaxation of the artificial fiber entanglement was introduced to the system. Moreover, a loop test with glass fibers showed a breakage distribution. This probability theory was introduced in the simulation to describe the breakage behavior better. The results had good agreement with the experimental data. The variations in accuracy of the breakage prediction shows that there is still a lack of understanding the mechanisms involved in the fiber breakage and the respective translation to the numerical models. One of the remaining problems is the noise in predicting the distance between the system's fibers and the curvature evolution. In future work, the prediction quality can be further improved by further reviewing the model and understanding the influence of forces employed in the system.

The modified fiber attrition model was implemented into Moldex3D and validated using PPGF20 and PPGF30 to find the optimum value of the fitting parameters. As lambda is a set value for different fiber content, this study focused on flow-fiber coupling with fiber attrition model. The length of purged materials from injection molding process determined the start point for fiber orientation and fiber attrition prediction. The length of three locations on the plaque were extracted to validate the new fiber attrition model. The simulation results showed good agreement with the injection molded plaques. It was observed that for different fiber content and different part thickness, the optimum value for fitting parameter of the modified breakage model is still within the same range. This will save time for users on adjusting parameters for the modified fiber breakage model while still obtaining a satisfactory fiber attrition prediction for polymer processing. The relationship between the parameters and the initial fiber aspect ratio has been identified, providing a better understanding for selecting optimal parameters in

the simulation. By manually inputting various fiber aspect ratios as the starting point of the simulation, it is also possible to obtain the breakage distribution throughout the manufacturing process. Furthermore, the modified breakage model has been applied to a complex part geometry application, specifically a tailgate, demonstrating the model's capability to predict fiber length reduction in an industrial setting. However, the results exhibit a stronger correlation with the shear stress profile in the system rather than the shear rate profile. Consequently, the model has been revised to incorporate shear stress into the consideration of the rate of deformation during breakage.

#### 6.1. Recommendations for future work

First, it is essential to investigate how the modified breakage model impacts warpage results in the injection molding process. Since fiber orientation plays a critical role in determining warpage outcomes in injection molding, the utilization of fiber-flow coupling will be crucial for studying the influence of fiber length on warpage results. Additionally, it is also worthwhile to understand the relationship between fiber length and its impact on orientation predictions. A comprehensive understanding of how variations in fiber length affect orientation predictions is fundamental for enhancing the overall quality of molded parts.

Furthermore, a comprehensive examination can be conducted to determine how the modified breakage model improves the accuracy of predicting mechanical properties in injection-molded components. Different mechanical testing results from injection-molded parts can be closely compared to the model's predictions against real-world mechanical property outcomes.

Lastly, in the context of the newly proposed shear stress-induced fiber breakage model, it is advisable to extend the experiments to include varying rotational speeds, including 4 rpm. This expanded experimentation will serve to validate the four newly proposed parameters.

#### 6.2. Publications

#### **Published**

- [1] S.Kugler, C. Cruz, A. Kech, **T.-C. Chang**, and T. Osswald, "Workflow for Enhanced Fiber Orientation Prediction of Short Fiber-reinforced Thermoplastics," in Annual Technical Conference—ANTEC, Conference Proceeding (2020).
- [2] **T.-C. Chang**, A. Bechara Senior, H. Celik, D. Brands, A. Yanev, and T. Osswald, "Validation of fiber breakage in simple shear flow with direct fiber simulation," J. Compos. Sci. 4, 134 (2020).
- [3] Yang, H.G.; Román, A.J.; **Chang, T.C.**; Yu, C.L.; Jiang, J.; Shotwell, D.; Chen, E.W.; Osswald, T.A.; Turng, L.S. Cell morphologies, mechanical properties, and fiber orientation of glass fiber-reinforced polyamide composites: Influence of subcritical gas-laden pellet injection molding foaming technology. Phys. Fluids (2022).

#### Under preparation

- [1] Polymer Composites: Modeling fiber orientation evolution with different fiber concentration in simple shear flow with direct fiber simulation.
- [2] Polymer Composites: Modification of the Slit Method Orientation Analysis Algorithm to allow for 3D Fiber Orientation Distribution Analysis
- [3] *Journal of Non-Newtonian Fluid Mechanics*: Modeling fiber length attrition in injection molding of long fiber-reinforced thermoplastics.

## 7. Reference

- [1] Yao, J., Zhou, Z., Zhou, H. "Highway Engineering Composite Material and Its Application." Highw. Eng. Compos. Mater. 2019, pp. 1-9.
- [2] Goris, S. "Characterization of the Process-Induced Fiber Configuration of Long Glass Fiber-Reinforced Thermoplastics." Ph.D. Thesis, University of Wisconsin-Madison, Madison, WI, USA, 2017.
- [3] Osswald, T., Menges, G. "Materials Science of Polymers for Engineers, 3rd ed." Hanser Publisher, 2012.
- [4] Phelps, J. H., Abd EI-Rahman, A.I., Kunc, V., Tucker, C. L. "A model for fiber length attrition in injection molded long-fiber composites." Compos. Part Appl. Sci. Manuf. 2013, pp. 11-21.
- [5] Thomason, J. L. "The influence of fiber length and concentration on the properties of glass fiber reinforced polypropylene. 7. Interface strength and fiber strain in injection molded long fiber PP at high fiber content." Compos. Part Appl. Sci. Manuf. 2007, pp. 210–216.
- [6] Ning, H., Lu, N., Hassen, A.A., Chawla, K., Selim, M., Pillay, S. "A review of Long fiber thermoplastic (LFT) composites." Int. Mater. Rev. 2019, pp. 164–188.
- [7] Fu, S.Y., Hu, X., Yue, C.Y. "Effects of fiber length and orientation distributions on the mechanical properties of short-fiber-reinforced polymers: A Review." Int. J. Mater. Res. 1999, pp. 74–83.
- [8] Thomason, J. L., Vlug, M. A. "Influence of fiber length and concentration on the properties of glass fiber-reinforced polypropylene: 4. Impact Properties." Composites Part A: Applied Science and Manufacturing, 1997, pp. 277-288.
- [9] Herakovich, C. T. "Mechanics of Fibrous Composites, First Edition." John Wiley and Sons, Inc., 1998.
- [10] Goris, S., Simon, S., Montoya, C., Bechara, A., Candal, MV., Brands, D., Yanev, A., Osswald, T. "Experimental study on fiber attrition of long glass fiber-reinforced thermoplastics under controlled conditions in a Couette flow." Proceedings of the Annual technical conference of the Society of Plastics Engineers, Anaheim, USA, 2017, pp. 1-9.
- [11] Kugler, S.K., Lambert, G.M., Cruz, C., Kech, A., Osswald, T.A., Baird, D.G. "Macroscopic fiber orientation model evaluation for concentrated short fiber reinforced polymers in comparison to experimental data". "Polymer Composites." 2020, pp. 2542–2556.
- [12] Evans, D. J., Morris, O. P. "Non-Newtonian molecular dynamics." Computer Physics Reports. 1984, pp. 297-343.

- [13] Phelps, J. H. "Processing-microstructure models for short- and long-fiber thermoplastic composites," 2009, pp. 1-9.
- [14] Advani, S. G., and C. L. Tucker III. "The use of tensors to describe and predict fiber orientation in short fiber composites." "Journal of Rheology" 1987, pp. 751–784.
- [15] Phelps, J., Abd El-Rahman, A., Kunc, V., & Tucker, C. "A model for fiber length attrition in injection-molded long-fiber composites." "Composites Part A: Applied Science and Manufacturing," 2013, pp. 11-21.
- [16] Rohde, M., Ebel, A., Wolef-Fabris, F., & Altstadt, V. "Influence of Processing Parameters on the fiber length and impact properties of Injection Molded long glass fiber reinforced polypropylene." "International Polymer Processing," 2011, pp. 292-303.
- [17] Nguyen, B. N.; Bapanapalli, S. K.; Holbery, J. D.; Smith, M. T.; Junc, V.; Frame, B. J.; Phelps, J. H.; Tucker, C. "Fiber length and orientation in long-fiber injection-molded thermoplastics Part I: Modeling of Microstructure and Elastic Properties." "Journal of Composites Materials," 2008, pp. 1003-1029.
- [18] YILMAZER, U.; CANSEVER, M. "Effects of processing conditions on the fiber length distribution and mechanical properties of glass fiber reinforced nylon-6." "Polymer Composites," 2002, pp. 61-71.
- [19] Forgacs, O. L.; Mason, S. G. "Particle motions in sheared suspensions. IX. Spin and deformation of threadlike particles." "Journal of Colloid Science," 1959, pp. 457-472.
- [20] Hinch, E. J. "The distortion of a flexible inextensible thread in a shearing flow." "Journal of Fluid Mechanics," 1976, pp. 317-333.
- [21] Goris, S., Simon, S., Montoya, C., Bechara, A., Candal, MV., Brands, D., Yanev, A., Osswald, T. "Experimental study on fiber attrition of long glass fiber-reinforced thermoplastics under controlled conditions in a Couette flow." Proceedings of the Annual technical conference of the Society of Plastics Engineers, Anaheim, USA, 2017, pp. 1-9.
- [22] Huang, C.T; Tseng, H.C. "Simulation prediction of the fiber breakage history in regular and barrier structure screws in injection molding." Polym Eng Sci, 2018, pp. 452-459.
- [23] Bechara, A., Goris, S., Yanev, A., Brands, D., & Osswald, T. "Novel modeling approach for fiber breakage during molding of long fiber-reinforced thermoplastics." Physics of Fluids, 2021, 33, 073318.
- [24] Dyson, F. "A meeting with Enrico Fermi." Nature, 2004, 427.
- [25] Ross, R.F.; Klingenberg, D.J. "Dynamic simulation of flexible fibers composed of linked rigid bodies." J Chem Phys, 1997, 106, pp. 2949-2960.

- [26] Schmid, C.F.; Switzer, L.H.; Klingenberg, D.J. "Simulations of fiber flocculation: Effects of fiber properties and interfiber friction." J Rheol, 2000, 44, pp. 781-809.
- [27] Joung, C.G.; Phan-Thien, N.; Fan, X.J. "Direct simulation of flexible fibers." J Non-Newtonian Fluid Mech, 2001, 99, pp. 1-36.
- [28] Londoño-Hurtado, A.; Osswald, T. "Fiber jamming and fiber matrix separation during compression molding." J Plastics Tech, 2006, 2(4), pp. 1-17.
- [29] Sasayama, T.; Inagaki, M. "Simplified bead-chain model for direct fiber simulation in viscous flow." J Non-Newtonian Fluid Mech, 2017, 250, pp. 52-58.
- [30] Ericsson KA, Toll S, Manson JAE. "The two-way interaction between anisotropic flow and fiber orientation in squeeze flow." J Rheol., 1997;41:491.
- [31] Dweib MA, Brádaigh CMÓ. "Anisotropic modeling of isothermal squeezing flow of Glass-Mat reinforced thermoplastics (GMT)." Polym Compos, 1998;19:588–99.
- [32] Favaloro, A. J. "Rheological behavior and manufacturing simulation of prepreg platelet molding system." PhD thesis. Purdue University, 2017.
- [33] Tseng, H.-C.; Favaloro, A. J. "A new anisotropic viscous constitutive model for composites molding simulation." Composites, Part A, 2018, 115, 112.
- [34] Tseng, H.-C.; Favaloro, A. J. "The use of informed isotropic constitutive equation to simulate anisotropic rheological behaviors in fiber suspensions." J. Rheol., 2019, 63, 263.
- [35] Tseng, H.-C.; Chang, R.-Y.; Hsu, C.-H. "Phenomenological improvements to predictive models of fiber orientation in concentrated suspensions." J. Rheol., 2013, 57, 1597.
- [36] Tseng H-C, Chang R-Y, Hsu C-H. "An objective tensor to predict anisotropic fiber orientation in concentrated suspensions." J Rheol., 2016;60:215–24.
- [37] Tseng, H.-C.; Chang, R.-Y.; Hsu, C.-H. "Improved fiber orientation predictions for injection molded fiber composites." Compos Part A Appl Sci Manuf, 2017;99:65–75.
- [38] Tseng, H.-C.; Chang, R.-Y.; Hsu, C.-H. "Method and computer readable media for determining orientation of fibers in a fluid, U.S. patent pending in USPTO with publication application number of US-2012-0330627-A1, 2012.
- [39] Hoffman, R.L. "Discontinuous and dilatant viscosity behavior in concentrated suspensions. 1. Observation of a flow instability." T. Soc. Rheol., 1972, 16, pp. 155–173.

- [40] Barnes, H.A. "Shear-thickening (dilatancy) in suspension of nonaggregating solid particles dispersed in Newtonian liquids." J. Rheol., 1989, 33, pp. 329–366.
- [41] Sundararajakumar, R.R.; Koch, D.L. "Structure and properties of sheared fiber suspensions with mechanical contacts." J. Non-Newton. Fluid Mech., 1997, 73, pp. 205–239.
- [42] Pérez, C. "The Use of a Direct Particle Simulation to Predict Fiber Motion in Polymer Processing." Ph.D. Thesis, University of Wisconsin-Madison, Madison, WI, USA, 2016.
- [43] Osswald, T.; Ghandi, U.; Goris. "Discontinuous Fiber Reinforced Composites, 1st ed." Carl-Hanser Verlag: Munich, Germany, 2020.
- [44] Wang, G.; Yu, W.; Zhou, C. "Optimization of the rod chain model to simulate the motions of a long flexible fiber in simple shear flows." European Journal of Mechanics B/Fluids, 2006, 25, pp. 337-347.
- [45] Anczurowski, E.; Mason, S. G. "The kinetics of flowing dispersions: II. Equilibrium orientations of rods and discs (theoretical)." J Colloid Science, 1967, 23, pp. 522-532.
- [46] Anczurowski, E.; Mason, S. G. "The kinetics of flowing dispersions: III. Equilibrium orientations of rods and discs (experimental)." J Colloid Science, 1967, 23, pp. 533-546.
- [47] Switzer, L. H.; Klingenberg, D. J. "Rheology of sheared flexible fiber suspensions via fiber-level simulations." J Rheology. 2003, 47, pp. 759-778.
- [48] Lindström, S. B.; Uesaka, T. "Simulation of the motion of flexible fibers in viscous fluid flow." Physics of Fluids. 2007, 19, p. 113307.
- [49] Mason, S. G.; Manley, R. S. J. "Particle Motions in Sheared Suspensions: Orientations and Interactions of Rigid Rods." Proceedings of the Royal Society of London A: Mathematical, Physical and Engineering Sciences. 1956, 238, pp. 117-131.
- [50] Goldsmith, H. L.; Mason, S. G. "The flow of suspensions through tubes. I. Single spheres, rods, and discs." J Colloid Science. 1962, 17, pp. 448-476.
- [51] Lees AW, Edwards SF, "The computer study of transport processes under extreme conditions," J Phys C Solid State Phys., 1972.
- [52] Jeffery, G. B. "The Motion of Ellipsoid Particles Immersed in a Viscous Fluid." "Proceedings of the Royal Society of London. Series A," 1922, pp. 161-179.
- [53] Beer, Ferdinand P., E. Russell Johnston Jr., and John T. DeWolf. "Mechanics of Materials." Publisher, 2020.

- [54] Sinclair, D. A. "Bending Method for Measurement of the Tensile Strength and Young's Modulus of Glass Fibers." Journal of Applied Physics. 1950, 21, pp. 380-386.
- [55] Çelik, H. "Numerical Study to Predict Fiber Motion and Fiber Attrition of Long-Fiber-Reinforced Thermoplastics during the Injection Molding Process using a Single Particle Model." M.Sc. Thesis, IKV, RWTH Aachen University, Germany, 2017.
- [56] Evans, D. J.; Morris, O. P. "Non-Newtonian molecular dynamics." Computer Physics Reports, 1984, 1, pp. 297-343.
- [57] Chapman, B.; Jost, G.; van der Pas, R. "Using OpenMP: Portable Shared Memory Parallel Programming." MIT Press: Cambridge, MA, USA, 2007.
- [58] William, G. "Using MPI: Portable Parallel Programming with the Message-Passing Interface." MIT Press: Cambridge, MA, USA, 1999.
- [59] Tim Mattson. "Recent developments in parallel programming: the good, the bad, and the ugly." Euro-Par 2013.
- [60] El-Rewini, H.; Abd-El-Barr, M. "Advanced Computer Architecture and Parallel Processing." John Wiley & Sons, Inc.: Hoboken, NJ, USA, 2005.
- [61] Gebali, F. "Algorithms and Parallel Computing." John Wiley & Sons, Inc.: Hoboken, NJ, USA, 2011.
- [62] Amdahl, G. M. "Validity of the Single Processor Approach to Achieving Large-Scale Computing Capabilities." AFIPS Conference Proceedings, 1967, 30, 483-485.
- [63] Hager, G.; Wellein, G. "Introduction to High Performance Computing for Scientists and Engineers." CRC Press: Boca Raton, FL, USA, 2010.
- [64] Dongarra, J.J.; Foster, I.; Fox, G.C. "Sourcebook of Parallel Computing." Morgan Kaufman Publishers: San Francisco, CA, USA, 2003.
- [65] Folgar, F. and Tucker, C. L. "Orientation Behavior of Fibers in Concentrated Suspensions." "Journal of Reinforced Plastics and Composites," 1984, vol. 3, no. 2, pp. 98–119.
- [66] Phelps, J. H. and Tucker, C. L. "An anisotropic rotary diffusion model for fiber orientation in short- and long-fiber thermoplastics." "Journal of Non-Newtonian Fluid Mechanics," 2009, pp. 165–176.
- [67] Tseng, H. C., Chang, R. Y., and Hsu, C. H. "Method and computer readable media for determining orientation of fibers in a fluid." EP2537661 A2, 2012, pp. 1-9.
- [68] Kunc, V.; Frame, B.; Nguyen, B. N.; Tucker, C. L.; Velez-Garcia, G. "Fiber length distribution

measurement for long glass and carbon fiber reinforced injection molded thermoplastics." SPE Automot. Compos. Div. - 7th Annu. Automot. Compos. Conf. Exhib. ACCE 2007 - Driv. Perform. Product., 2007, vol. 2, pp. 866–876.

# Appendix A

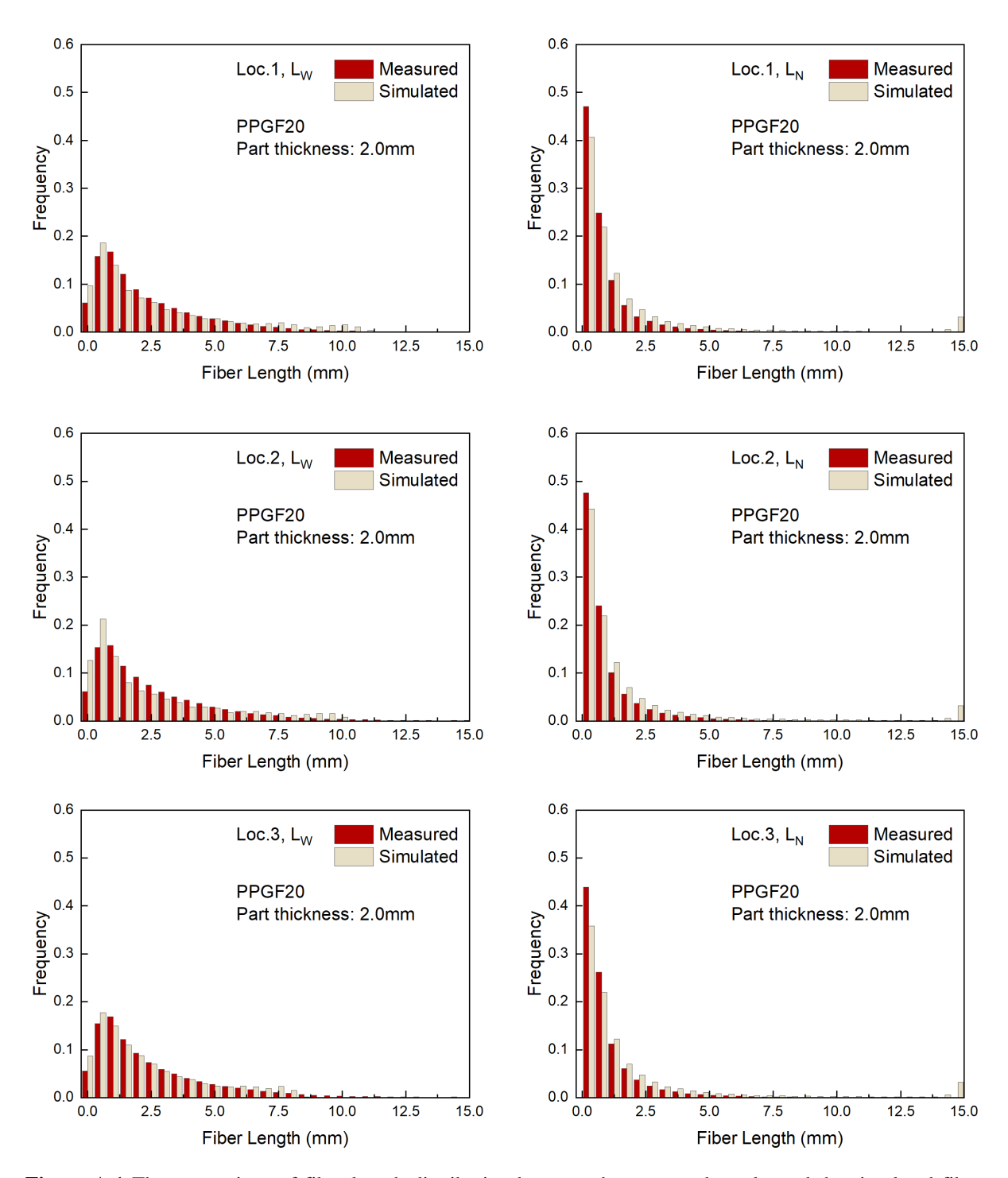


**Figure A.1** The comparison of fiber length distribution between the measured results and the simulated fiber length distribution at four locationsn for PPGF20, 2.0 mm-thick injection molded plaque.

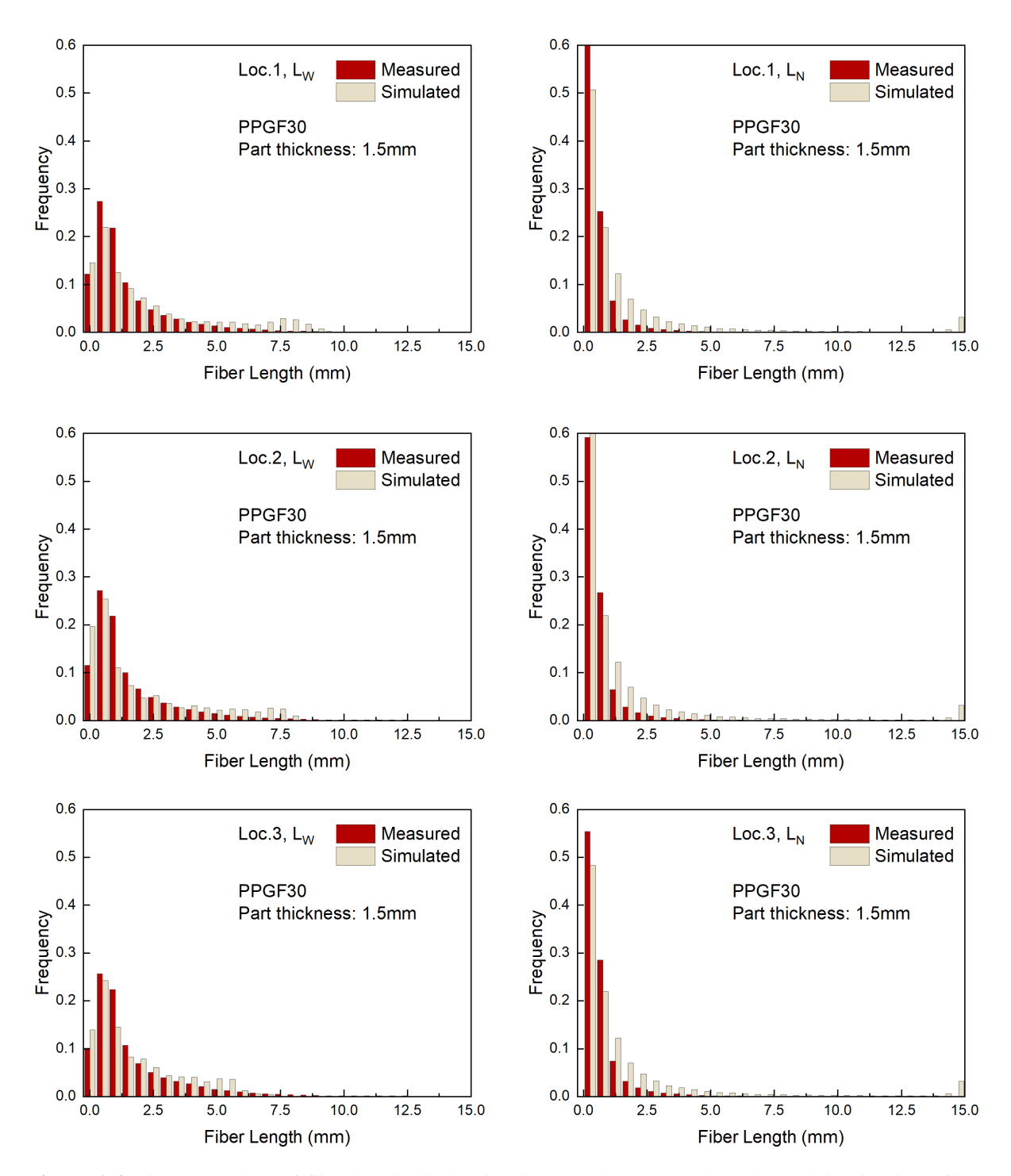


**Figure A.2** The comparison of fiber length distribution between the measured results and the simulated fiber length distribution at four locations for PPGF30, 1.5 mm-thick injection molded plaque.

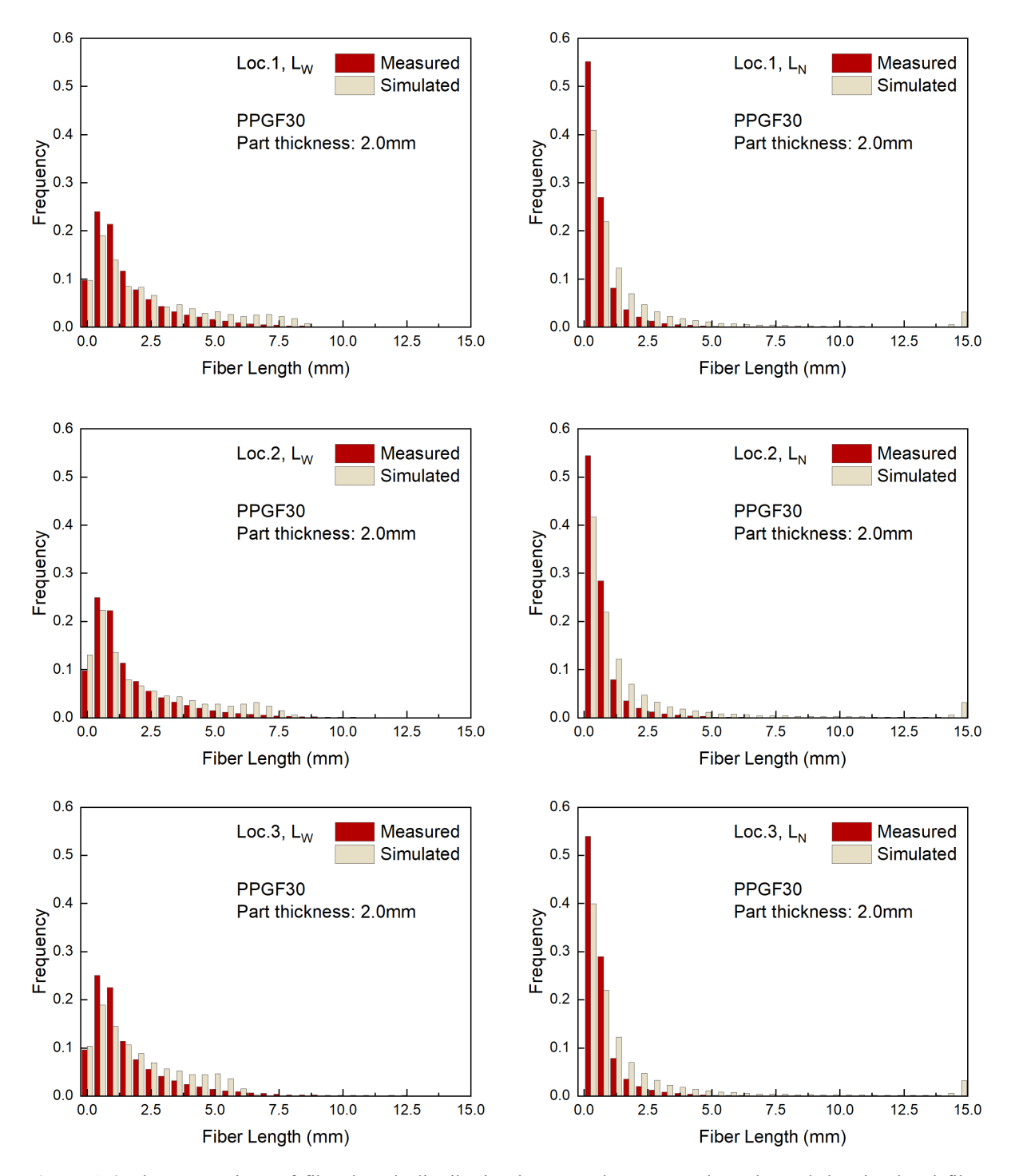


**Figure A.3** The comparison of fiber length distribution between the measured results and the simulated fiber length distribution at four locations for PPGF30, 2.0 mm-thick injection molded plaque.